

THE CENTRAL REGION OF ACTIVE GALACTIC NUCLEI

DISSERTATION

zur Erlangung des Grades

„Doktor der Naturwissenschaften“

an der Fakultät für Physik und Astronomie

der Ruhr-Universität Bochum

vorgelegt von

Michael Ramolla

Bochum 2012

Erster Gutachter: Prof. Dr. Rolf Chini,
Ruhr-Universität Bochum

Zweiter Gutachter: Prof. Dr. Wolfram Kollatschny,
Georg-August-Universität Göttingen

Disputation: 17. Dezember 2012

ABSTRACT

This thesis contains three interconnected parts, spanning an engineering project, a long term observational campaign and a novel analysis of archival data, all aimed at the research of the central region of active galactic nuclei (AGN):

1. The development and scientific verification of a telescope control system and data reduction pipeline for the optical 40 cm *VYSOS 16* telescope of the Universitätssternwarte Bochum in Chile. After an analysis of various mechanical errors, I develop a motion control system of the telescope axes, allowing for robotic observations of AGN.
2. New results on the size of the broad line region (BLR) of four AGN. The observations with the robotic telescopes *VYSOS 6*, *BEST II* and *VYSOS 16* demonstrate that photometric reverberation mapping is an efficient tool to substantially tighten the $R_{\text{BLR}} \propto L_{\text{AGN}}^\alpha$ relationship with $\alpha \approx 0.5$. It opens the door to measure BLR sizes R_{BLR} and the host-subtracted luminosity L_{AGN} for large samples of AGN, without the need of costly spectroscopy in all nights where the respective lightcurve is taken.
3. A new criterion to efficiently find water megamasers at 22 GHz. By comparing Mid-IR observations with X-ray fluxes, both drawn from international data archives, I can show that X-ray absorbed sources are more likely to be seen edge-on and thus are more likely to present maser emission towards the observer.

By expanding our knowledge about the properties and systematics of the central region, these results contribute to the prospect of using AGN for distance measurements of cosmological significance. Maser offer a direct geometric distance in type 2 AGN, while the $R_{\text{BLR}} \propto L_{\text{AGN}}^\alpha$ relationship may be applicable to type 1 AGN. *VYSOS16* has now become a key telescope to perform large AGN monitoring campaigns.

CONTENTS

| | | |
|-------|---|----|
| 1 | INTRODUCTION | 1 |
| 1.1 | Seyfert Galaxies | 1 |
| 1.2 | The Model of Active Galactic Nuclei | 2 |
| 1.2.1 | Spectral Energy Distribution | 2 |
| 1.2.2 | Line Emission and Absorption | 3 |
| 1.3 | Developing a Telescope Control System | 3 |
| 1.4 | Reverberation Mapping | 3 |
| 1.5 | Water Megamaser | 5 |
| 2 | VYSOS16 TELESCOPE CONTROL | 7 |
| 2.1 | Periodic error correction | 9 |
| 2.2 | Pointing Model | 11 |
| 2.3 | Dithering | 14 |
| 2.4 | Observations | 15 |
| 2.5 | Reduction Pipeline | 16 |
| 2.6 | Science verification | 17 |
| 3 | PHOTOMETRIC REVERBERATION MAPPING | 19 |
| 3.1 | Photometric Observations | 19 |
| 3.1.1 | VYSOS6 | 21 |
| 3.1.2 | VYSOS16 | 21 |
| 3.1.3 | BEST II | 21 |
| 3.2 | Photometry | 22 |
| 3.3 | Spectroscopic Observations | 22 |
| 3.3.1 | Robert Stobie Spectrograph at the South African Large Telescope | 23 |
| 3.3.2 | Calar Alto Faint Object Spectrograph | 23 |
| 3.4 | Spectra and Velocity Dispersions | 23 |
| 3.4.1 | PG0003 | 23 |
| 3.4.2 | Ark120 | 24 |
| 3.4.3 | 3C120 | 25 |
| 3.4.4 | ESO 374-G25 | 27 |
| 3.5 | Results and discussion | 31 |
| 3.5.1 | Lightcurves and BLR size | 31 |
| 3.5.2 | BH-Masses | 44 |
| 3.5.3 | Host-subtracted AGN luminosity | 45 |
| 3.5.4 | The BLR size – Luminosity relationship | 53 |
| 3.6 | Conclusion and Outlook | 55 |
| 4 | FINDING MEGAMASER CANDIDATES | 57 |
| 4.1 | Sample Selection and Data | 57 |
| 4.1.1 | The parent sample | 57 |
| 4.1.2 | Maser information | 58 |
| 4.1.3 | [OIV] line and $7\mu\text{m}$ continuum flux | 58 |
| 4.1.4 | X-rays and [OIII] flux | 59 |
| 4.1.5 | Additional maser sources | 59 |
| 4.2 | Results and discussion | 59 |
| 4.2.1 | Nuclear X-ray obscuration | 60 |

| | | |
|-------|---|----|
| 4.2.2 | Extended obscuration of the dust torus and NLR | 62 |
| 4.2.3 | Combined picture | 65 |
| 4.2.4 | Comparison of the three samples with other known masers | 66 |
| 4.2.5 | Maser and AGN luminosity | 67 |
| 4.3 | Conclusion | 69 |
| 5 | SUMMARY AND OUTLOOK | 71 |
| A | APPENDIX | 73 |
| A.1 | Hardware | 73 |
| A.2 | Software | 74 |
| A.3 | Vysos16 Script Commands | 74 |
| A.4 | Example of a complete observation plan | 76 |
| A.5 | Mathematical Methods | 77 |
| A.5.1 | The Discrete Cross Correlation Function | 77 |
| A.5.2 | The Flux Variation Gradient | 78 |
| A.6 | Tables | 79 |
| A.7 | Figures | 87 |
| | BIBLIOGRAPHY | 92 |

LIST OF FIGURES

| | | |
|-----------|--|----|
| Figure 1 | Basic model of the structure surrounding the nuclear region. | 1 |
| Figure 2 | VYSOS 16 taking flatfield images in Summer 2012. | 7 |
| Figure 3 | Intensity profiles of a point source | 8 |
| Figure 4 | Six different 1800 second long exposures with VYSOS 16. | 8 |
| Figure 5 | Periodically changing offsets of a stellar positions. | 10 |
| Figure 6 | Overview of a complete set of pointing observations. | 12 |
| Figure 7 | Accuracy of the pointing model. | 13 |
| Figure 8 | Offsets of the dither positions. | 14 |
| Figure 9 | Spatial coverage of the sub-pixel shifts. | 15 |
| Figure 10 | Comparison between POSS1 and VYSOS 16 images. | 17 |
| Figure 11 | Preliminary lightcurves of RXJ1741.4+0348. | 18 |
| Figure 12 | Phase diagram of the O-star CPD-41°7742. | 18 |
| Figure 13 | Effective transmission of the VYSOS 6 filters. | 19 |
| Figure 14 | Effective transmission of the VYSOS 16 filters. | 19 |
| Figure 15 | Observed spectrum of PG0003+199. | 24 |
| Figure 16 | Observed spectrum of Ark 120. | 25 |
| Figure 17 | CAFOS spectrum of 3C120 obtained on Oct.27 2009. | 26 |
| Figure 18 | CAFOS spectrum of 3C120 zoomed in at H β . | 26 |
| Figure 19 | SALT spectra of ESO 374-G25. | 29 |
| Figure 20 | SALT spectrum of ESO 374-G25 from 4th April 2012. | 30 |
| Figure 21 | Schematic view of an inclined BLR disk. | 31 |
| Figure 22 | <i>B</i> band and H α light curves of PG0003+199. | 32 |
| Figure 23 | Cross correlation of the <i>B</i> and H α light curves of PG0003+199. | 33 |
| Figure 24 | Result of the FR/RSS error analysis of the light curves of PG0003+199. | 33 |
| Figure 25 | Light curves of Ark120 between October 2009 and March 2010. | 34 |
| Figure 26 | Flux-flux diagram of Ark120 for the [O III] and <i>V</i> band filter. | 35 |
| Figure 27 | Cross correlations of Ark 120 light curves. | 36 |
| Figure 28 | FR/RSS cross correlation results of Ark 120. | 36 |
| Figure 29 | Artificial <i>B</i> and NB light curves of Ark120. | 37 |
| Figure 30 | Cross correlation of the complemented <i>B</i> and NB light curves. | 37 |
| Figure 31 | Observed light curves for 3C120. | 38 |
| Figure 32 | Flux-flux diagram of 3C120. | 39 |
| Figure 33 | Results of the cross correlations of the lightcurves of 3C120. | 39 |
| Figure 34 | Dependence of the lag from the bin size | 40 |
| Figure 35 | Results of the FR/RSS cross correlation for 3C120. | 40 |
| Figure 36 | Relative photometric lightcurves of ESO 374-G25. | 42 |
| Figure 37 | Discrete cross correlation of ESO 374-G25. | 43 |
| Figure 38 | Histogram result of the FR/RSS error analysis of ESO 374-G25. | 43 |
| Figure 39 | <i>B</i> versus <i>V</i> fluxes of PG0003+199, measured in a 7''.8 aperture. | 47 |
| Figure 40 | <i>B</i> versus <i>V</i> fluxes of Ark120, measured in a 7''.5 aperture. | 49 |
| Figure 41 | <i>B</i> versus <i>V</i> band FVG diagram of 3C120. | 50 |
| Figure 42 | <i>B</i> versus <i>V</i> flux variations of ESO 374-G25. | 53 |
| Figure 43 | $R_{BLR} - L$ relationship diagram. | 54 |
| Figure 44 | Observed 2-10 keV X-ray versus [O IV] line luminosity. | 61 |

| | | |
|-----------|--|----|
| Figure 45 | Histogram of the $L_X / L_{[\text{OIV}]}$ ratio. | 61 |
| Figure 46 | Observed X-ray versus [OIV] line flux. | 62 |
| Figure 47 | [OIV] flux histogram of Sy2 masers for absorbed sources. | 63 |
| Figure 48 | Histogram of the $7\ \mu\text{m}$ continuum to [OIV] line ratio. | 64 |
| Figure 49 | Distribution of [OIII] versus [OIV] luminosity. | 64 |
| Figure 50 | Histogram of the [OIII] to [OIV] ratio. | 65 |
| Figure 51 | Observed 2-10 keV X-rays plotted against [OIV] luminosity. | 67 |
| Figure 52 | Maser H ₂ O versus [OIV] luminosity. | 68 |
| Figure 53 | Flowchart: Software interactions. | 87 |
| Figure 54 | Format of the data-packets of the NI card. | 87 |
| Figure 55 | Workflow of the observations script. | 88 |
| Figure 56 | Diagnostic plot of a successfully applied observation plan. | 89 |
| Figure 57 | Flowchart: Pipeline workflow. | 90 |
| Figure 58 | Distortion parameters of <i>VYSOS 16</i> . | 91 |

LIST OF TABLES

| | | |
|---------|---|----|
| Table 1 | Characteristics of our photometric RM campaign. | 20 |
| Table 2 | Filters on the <i>VYSOS 6</i> and <i>VYSOS 16</i> telescopes. | 79 |
| Table 3 | Results of the DCF analysis of the obtained lightcurves. | 80 |
| Table 4 | Statistics of sample complement and matching. | 80 |
| Table 5 | The luminosity ratios for each subset of Seyfert galaxies. | 81 |
| Table 6 | Measured fluxes and literature values. | 82 |
| Table 6 | continued. | 83 |
| Table 6 | continued. | 84 |
| Table 6 | continued. | 85 |
| Table 6 | continued. | 86 |

ACRONYMS

| | |
|-------|---|
| AIRUB | Astronomisches Institut der Ruhr-Universität Bochum |
| ACS | Alma Common Software |
| BAT | Burst Alert Telescope |
| BEST | Berlin Extrasolar Search Telescope |
| BH | Black Hole |
| BLR | Broad line region |
| CAFOS | Calar Alto Faint Object Spectrograph |
| DCF | Discrete correlation function |
| DSS | Digitized Sky Survey |
| EUV | extreme ultra-violet |
| FVG | Flux variation gradient |
| IRS | Infrared-Spectrograph |
| ISO | Infrared Space Observatory |
| K-S | Kolmogorov-Smirnov |
| NLR | Narrow line region |
| QSO | Quasi-stellar object |
| RM | Reverberation mapping |
| RSS | Robert Stobie Spectrograph |
| SALT | Southern African Large Telescope |
| SB | Starburst |
| SED | Spectral energy distribution |
| Sy1 | Seyfert galaxy, type 1 to 1.5 |
| Sy2 | Seyfert galaxy, type 1.8 to 2 |
| USB | Universitätssternwarte der Ruhr-Universität Bochum |
| VPH | Volume Phase Holographic |
| VYSOS | Variable Young Stellar Object Survey |

INTRODUCTION

This Chapter will give the reader a short introduction into the field and the latest scientific progress. In this context, the backgrounds of the analysis in the Chapters 3 and 4 are explained. Throughout the whole thesis, distances from which we derived the luminosities are taken from the NED database. The cosmology is based on $H_0 = 73 \text{ km s}^{-1} \text{ Mpc}^{-1}$, $\Omega_\Lambda = 0.73$, and $\Omega_m = 0.27$.

1.1 SEYFERT GALAXIES

An active galactic nucleus (AGN) can be described as a compact region in a galactic center with a luminosity comparable or even superior to its entire host galaxy. It can also feature very broad emission lines ($> 1000 \text{ km/s}$), power-law-continua, variability on many timescales (hint for compactness) and strong radio-emission (not explainable by thermal radiation models).

From Carl Seyferts first investigations in 1943 until today, substantial progress in the understanding of the different components of these objects has been made. Today, the generally accepted picture¹ (Fig. 1) of AGN now contains a supermassive black hole (BH), an accretion disk, a jet of relativistic particles with its large-scale effects, an X-ray source that is close to the central engine, a torus-shaped configuration of dust that constrains the nuclear emission, and clouds of gas that form two popular regions: Close to the nucleus, are the fast-moving broad line regions (BLR) with high densities, while the narrow line regions (NLR) are more distant. The lower densities and low velocities in the NLR allow the clouds to emit sharp forbidden lines.

Nevertheless, there remain a lot of unsolved and disputed questions when one tries to conflate all these aspects into a single unified model, as for instance the matter fueling process or the relation between the AGN and its galactic environment, e.g. absorption effects observable in the mid-infrared (MIR) continuum.

¹ Described in detail in (Alloin and Johnson, 2006).

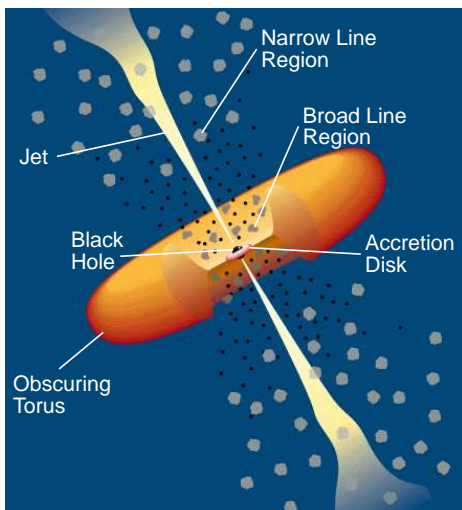


Figure 1: Basic model of the structure surrounding the nuclear region, as sketched by Urry and Padovani (1995). If the center is looked at through the torus, then the BLR clouds are hidden, resulting in a type 2-like appearance of the source. Seeing through the jet, we will consider the source being a Blazar. Otherwise it will appear as a type 1 AGN.

1.2 THE MODEL OF ACTIVE GALACTIC NUCLEI

The first concepts of AGN unification were introduced by Antonucci (1983) and Antonucci and Miller (1984, 1985), using spectropolarimetric observations of NGC1068 and NGC4151. By investigating polarized light, perpendicular to the radio emission axis, Antonucci found very broad and highly polarized components of the Balmer lines (up to ~ 7500 km/s in Antonucci and Miller 1985). Therefore he draws the fundamental conclusion that both Seyfert galaxy types are intrinsically identical and the observations are orientation dependent, by introducing an absorbing thick disk, in which the nuclear engine is embedded. The current model, mentioned afore, is still based on this concept.

This chapter will introduce basic concepts of the physical AGN structure. As the numerous observed objects are expected to present a widespread set of different intrinsic properties, further details will be explained in the discussion of the results respectively.

1.2.1 Spectral Energy Distribution

In contrast to normal or starburst galaxies, AGN generate an extraordinarily hard radiation field in their nuclear region. This radiation is mostly emitted by an accretion disk structure, similar as described above. It produces an excess in the extreme UV light, called blue bump, corresponding to the inner hot edge of the disk. But as a lot of the emitted energy is measured in the hard X-ray bands, the aforementioned maximum temperature at the disk's inner edges of $T_{\max} = 10^5$ K would not be sufficient. This leads to the conclusion that the X-ray flux emerges from a different hot medium. Since short-time variations of the high energy continuum appear, it can be assumed that this hot region rests also close to the BH. There are several effects that help to explain this observation. For example, diluted coronal gas accompanying the cool disk structure could generate very high temperatures in the range of 10^8 K. Depending on the Compton-depth it is furthermore possible to elevate softer X-ray photons to higher energies by scattering.

However, real accretion-disks are far more complicated and contain more unknown phenomena. For example, the effects of magnetic fields in the inner region, probably driving winds, is not clear yet.

The AGN signature in the MIR is mostly generated by reprocessed photons from the hot inner region of the surrounding structure. Assuming a torus of molecular dust (~ 1 pc), as proposed by the Unified Model by Antonucci and Miller (1984); Keel (1983), Pier and Krolik (1992) calculate an emission bump between ~ 2 and $15 \mu\text{m}$. This feature is not seen in regular starburst (SB) dominated galaxies, and due to the weak absorption in this wavelength regime the continuum could be used to find AGN. Hence, one may apply a selection based on the flux ratio between the continua at $25\mu\text{m}$ and $60\mu\text{m}$ (IRAS F25 μm /F60 μm), as performed by de Grijp et al. (1992).

1.2.2 Line Emission and Absorption

Broad Line Regions

For the presumably unabsorbed Sy_1 AGN spectra, kinematically broadened Balmer lines appear with velocity dispersions > 1000 km/s. These velocities require the emission regions to be close to the center of mass, regarding Keplerian movement. But due to this close distance, a free plasma would be pushed outwards as the radiation pressure fully impacts on each ion. Therefore, the emission regions are considered (i.e. in Alloin and Johnson 2006) to be embedded in high-density ($\sim 10^{10}$ cm $^{-3}$) clouds, presenting column-densities of $\sim 10^{23}$ cm $^{-2}$ with global covering factors of order 0.1, so that gravity dominates in them. The confinement of such clouds is not well understood, however, magnetic confinement may play a key role in this. The high density allows only the cloud's surface to be highly ionized. Furthermore, metastable states are de-excited most probably by collisions and the strongest predicted emission line becomes, among others, $Ly\alpha$ (Alloin and Johnson 2006).

Narrow Line Regions

In a far more extended volume around the nucleus (several kpc for luminous AGN) slower structures (several 100 kms $^{-1}$) of ionized gas are, due to their presumably lower densities, able to produce strong forbidden emission lines. This optically thin gas is also ionized by the powerful extreme ultra-violet (EUV) and X-ray photons from the central region. For particular elements one finds significant populations of particles with high ionization numbers (e.g. [OIV] with an excitation potential (ep) of 54.93 eV and [Ne V], ep: 97.12 eV).

The forbidden emission lines, investigated in this thesis, are emitted by low density high temperature ionized gas. In this plasma, collisional transitions are negligible for most of the involved elements except hydrogen and helium; Netzer (1990).

1.3 DEVELOPING A TELESCOPE CONTROL SYSTEM

Until March 2012 the Universitätssternwarte der Ruhr-Universität Bochum (USB) was performing the NB photometric RM only with the *VYSOS 6* telescope. Because of the huge demand for observing time on this instrument, it was highly desirable to have another automatic telescope with better light-collecting power for our faint AGN.

In principle, this instrument, *VYSOS 16* with a 40 cm diameter main mirror, was constructed already in Summer 2008. However, due to the bad condition of the main mirror and the control software, *VYSOS 16* couldn't be used for meaningful observations of variable objects. In Chapter 2, the solutions to these problems and their progress is documented. Finally, we are now able to perform autonomous robotic observations of faint AGN. The first results are presented in Chapters 2 and 3.

1.4 REVERBERATION MAPPING

Reverberation Mapping (Blandford and McKee 1982) has revolutionized our understanding of AGN during the past decades. Generally, spectroscopic monitoring is used to measure the delay τ of the broad emission line's reaction to nuclear blue continuum

variations. Using the light travel time allows to calculate the distance of these regions as $R_{\text{BLR}} = \tau \cdot c$.

The spectroscopy provides us also with a velocity dispersion σ_v of the emitting gas. Adopting Keplerian motion, one may estimate the enclosed mass, dominated by the supermassive black hole (Peterson et al. 2004 and references therein).

From theoretical considerations (Netzer 1990), the relationship $R_{\text{BLR}} \propto L_{\text{AGN}}^\alpha$, between BLR size and nuclear luminosity should have $\alpha = 0.5$. This has been investigated intensively (Bentz et al. 2006, 2009a; Kaspi et al. 2000, 2005; Koratkar and Gaskell 1991), with the latest result being $0.519^{+0.063}_{-0.066}$. Our goal is to further tighten this exponent, using a new photometric monitoring method, not requiring expensive spectroscopy on large aperture telescopes.

Because reverberation spectra usually require observations with at least a 2 m-class telescope, we present a first test of successful reverberation mapping using a 15 cm refractor (*VYSOS 6*) combined with a 40 cm mirror (*VYSOS 16*). We use a combination of *B*, *V* and a set of narrow band filters ([O III], [S II], 670 nm and 680 nm; details in Sect. 3.1). The broad filters are used to measure the triggering continuum variation, while the narrow filters are covering the H β or H α line response. Our sources have been selected dependent on their redshift in the way that one of their broad Balmer lines falls at least partially onto one of our narrow band filters.

To explore the capability and achievable accuracy of photometric reverberation mapping, we selected several local AGNs, the relatively clear-cut case PG0003+199 (Mrk 335) at redshift $z = 0.0258$ and the more challenging cases Ark 120 at $z = 0.0327$, and 3C120 at $z = 0.0330$ and the faint ESO 374-G25 at $z = 0.0237$. Spectroscopic reverberation results are available for the first three sources in Peterson et al. (1998a, 2004), Bentz et al. (2009b) and Grier et al. (2012a).

Our photometric investigation is accompanied by spectroscopic support observations. A first set of single epoch spectra was taken with the 2.2 m Calar Alto Faint Object Spectrograph (CAFOS). For ESO 374-G25 we collaborated in a study by Wolfram Kollatschny and Matthias Zetzl, Georg-August-Universität Göttingen, who took 10 spectra with the large 9.2 m South Africa Large Telescope (SALT), using the Robert Stobie Spectrograph (RSS).

To obtain the lag times, we apply a Discrete Correlation Function (DCF, Edelson and Krolik 1988) analysis to the lightcurves of the continuum, measured with the Johnson *B* band, and the broad Balmer line of interest, measured with a narrow band (NB) filter. The details of this principle are noted in Sect. A.5.1.

Our task will be to separate the pure AGN luminosity in our filters from the constant background of the host galaxy. Commonly, this is performed by applying complex galaxy model subtractions to high resolution images (e.g. HST images, see Bentz et al. (2009a)). As this is not possible with our equipment, we chose an alternative, the Flux Variation Gradient (FVG) method (Choloniewski 1981; Winkler et al. 1992), explained in detail in Sect. A.5.2.

Parts of the results that we present in Sect. 3.1 have already been published. The analysis of PG0003+199 and Ark120 is performed in Haas, Chini, Ramolla, Pozo Nuñez, Westhues, Watermann, Hoffmeister, and Murphy (2011). 3C120 has been studied in Pozo Nuñez, Ramolla, Westhues, Bruckmann, Haas, Chini, Steenbrugge, and Murphy (2012).

1.5 WATER MEGAMASER

While RM is an adequate tool for type 1 AGN, it can not be applied to type 2 AGN as their continuum and BLR emission is obscured by the dust torus that is seen edge-on. It is now straightforward to divert to frequencies that are able to penetrate this dust. Water megamaser emission, tracing the accretion disk, provides us with a solution here.

H₂O megamaser galaxies represent an extreme subclass of active galactic nuclei (AGN) with strong water maser emission at 22 GHz (reviews by Lo 2005 and Henkel et al. 2005). In those cases where the emission arises from a molecular disk and can be resolved spatially using very long baseline interferometry, the central BH mass, and the distance to the galaxy can be determined (e.g. for NGC 4258, Greenhill et al. 1993, Herrnstein et al. 1999). Thus, finding megamasers (*henceforth simply called masers*) and understanding their properties is of great interest.

Owing to theoretical considerations, a large line-of-sight column density of velocity coherent gas favors the detection of a maser. High velocity coherence of the maser emitting gas is required, because energy and momentum conservation imply that the induced photon has the same frequency and direction as the stimulating photon (e.g. Elitzur 2002). While the emission of an individual maser spot is directional (i.e. beamed), a collection of these spots statistically may be expected to radiate in all directions, but this has not yet been confirmed. The originally discovered water maser emission from AGN comes from (presumably edge-on) disks, and the resolved emission in most sources traces accretion disks and, in a few cases, star formation masers. However, two sources, Circinus and NGC3079 exhibit additional off-disk jet masers that seem to trace outflows. These outflow masers are potentially torus clouds, ejected perpendicular to the disk plane (Nenkova et al. 2008).

In the AGN unified model, an optically thick obscuring dust torus is envisioned to encircle the accretion disk and type-1 AGN are seen pole-on while type-2 AGN are seen edge-on (Antonucci 1993). Masers are almost exclusively found in AGN of Seyfert-2 or LINER type, consistent with the picture that masers are preferentially beamed in the plane of the torus (Braatz et al. 1997, 2004, Henkel et al. 2005). But not all type-2 AGN are masers.

The 22 GHz radio-frequency maser emission itself is believed to be largely unaffected by absorption; but high X-ray, optical, or mid-infrared obscuration may indicate that there is a high likelihood that the masing disk is seen edge-on, hence favoring a maser detection.

Type-2 AGN that host masers show a prevalence (> 80%) of high X-ray obscuring columns ($N_{\text{H}} > 10^{23}\text{cm}^{-2}$) and about half are Compton thick ($N_{\text{H}} > 10^{24}\text{cm}^{-2}$) (Braatz et al. 1997, Zhang et al. 2006, Greenhill et al. 2008). However, as pointed out by Zhang et al. (2006), among type-2 AGN the average X-ray derived column densities of masers and non-masers² are indistinguishable. One explanation of this unexpected result could be that X-ray scattering in clumpy media dilutes the true line-of-sight column density, and thus prevents us from deriving unbiased orientation information. Therefore, it is vital to include information from other frequencies than X-rays to reveal the potential influence of nuclear obscuration on the maser detection and non-detection, respectively.

² We denote as non-masers those AGN that have been observed at 22 GHz, but for which no megamaser was detected.

Zhang et al. (2010) analyzed the $K\alpha$ iron-line equivalent width $EW(K\alpha)$, following the strategy of Bassani et al. (1999), and compared it with two optical thickness parameters, the infrared 6-400 μm luminosity L_{IR} derived from IRAS 12-100 μm photometry and the [O III] 5007 \AA emission-line luminosity $L_{[\text{O III}]}$. Both parameters were adopted as isotropic tracers of the intrinsic AGN strength. While the $EW(K\alpha)$ distributions of 19 masers and 34 non-masers cover the same broad range (100 - 3000 eV), the median $EW(K\alpha)$ of masers is about a factor of four higher than that of the non-masers, indicating that the X-ray continuum of masers is absorbed stronger than that of non-masers.

However, it remains a matter of debate whether L_{IR} and $L_{[\text{O III}]}$ are indeed isotropic tracers of the intrinsic AGN luminosity. While [O III] has often been used as an isotropic AGN tracer (Alonso-Herrero et al. 1997; Bassani et al. 1999; Heckman et al. 2005; Lamastra et al. 2009; Mulchaey et al. 1994; Panessa et al. 2006), the discovery of polarized [O III] emission in some type-2 AGN (di Serego Alighieri et al. 1997) implies that a substantial fraction of the [O III] emission might be shielded by the torus. Further studies, using MIR emission lines such as [O IV] or [Ne V] as orientation independent tracers of the AGN power, provide evidence in terms of the [O III]/[O IV] ratio, that [O III] suffers orientation-dependent extinction, up to a factor of ten in individual cases (Haas et al. 2005, Meléndez et al. 2008a, Baum et al. 2010).

This is qualitatively consistent with results obtained using the (extinction-corrected) 2-10 keV X-ray luminosity L_X as an intrinsic measure of AGN power; Netzer et al. (2006) find that $L_{[\text{O III}]} / L_X$ of type-2 AGN is, on average, about a factor of two lower than that of type-1 AGN. Even in the face-on Sy1 case, the back-sided cone of the NLR lies – at least partly – behind an absorbing layer (e.g. the dust torus). Therefore, it is highly questionable how far [O III] can serve as an isotropic AGN tracer. The extinction correction via Balmer decrement ($H_\alpha / H_\beta = 3$) remains highly uncertain, since it is dependent on the geometry of the emitting and obscuring regions.

Hes et al. (1996) and Baker (1997) caution against the use of [O III] as a measure of the intrinsic NLR emission and suggest using [O II] 3727 instead. Observations of radio-loud AGN, where the orientation can be inferred from radio morphology, show that [O II] is largely orientation independent (Baker 1997; Hes et al. 1996). On the other hand, because of its low ionization potential, [O II] may also be dominated by star formation in the host (e.g. Ho 2005). Then, the decline in $L_{[\text{O II}]} / L_X$ with increasing L_X , also found by Netzer et al. (2006), could be naturally explained by a decline in host / AGN with increasing AGN L_X .

Likewise the mid-infrared ($\lambda < 40\mu\text{m}$) part of L_{IR} is orientation dependent (e.g. Fig. 16 in Buchanan et al. 2006), while the far-infrared ($\lambda > 40\mu\text{m}$) emission of Seyfert galaxies and low-luminosity quasars is dominated by star-forming contributions rather than the AGN itself (e.g. Maiolino and Rieke 1995, Schweitzer et al. 2006). Thus, a careful re-investigation using more suitable isotropic AGN tracers would be desirable.

In this thesis, I investigate the nuclear obscuration by reviewing the ratio of the almost unobscured [O IV]_{25.89 μm} to the potentially obscured hard X-rays in a well determined sample of 163 sources total, containing masers and non-masers. This will reveal if highly X-Ray obscured sources have a higher probability for a maser detection. This study has already been published in Ramolla, Haas, Bennert, and Chini (2011).

VYSOS₁₆ TELESCOPE CONTROL

In Summer 2008, the 40 cm reflector telescope *VYSOS 16* was installed at the Universitätssternwarte der Ruhr-Universität Bochum in order to monitor AGN and young stellar objects. Figure 2 shows a photograph of *VYSOS 16*. Unfortunately, the imaging quality was too poor to perform reliable photometry, especially for faint objects or crowded fields. This is illustrated by Fig. 3, left. In this image, the old PSF from the year 2008 shows a highly complex shape with inner and outer elliptical elements. Further focusing may flip the inner structure outwards and the former outer ellipse becomes the more focused center in turn. This optical defect is now well controlled since we replaced the main mirror with one provided by Bo Reipurth, IfA Hawaii. The replacement was taken from the northern twin *VYSOS 16-north*, the axes of which were broken during an earthquake.

The current optical system delivers a very circular and narrow PSF with about $3''/2$ FWHM. There is a minuscule amount of ellipticity, but as can be seen in Fig. 3, right, this can be well controlled with empirical PSF models. This particular shape of the PSF is a result of the image not being perfectly focused. The major axis is oriented diagonal towards the upper right corner. By traversing the point of perfect focus – defocusing into the other direction – the major axis will be flipped by 90° . This is typically caused by astigmatism, which may be a result of a tilted or imprecisely produced optical element (one of the three mirrors, or the coma corrector lens). By varying the different align- and adjustments of the optical elements, this error could not be compensated for. Apparently, this is another quality problem in the optical elements, but now only playing a minor role.

Even worse than the original optical defects, the tracking and pointing model of the system raised serious constraints for the observation of targets in the center of the CCD frame and especially for faint targets requiring long exposure times. This is shown by the examples in Fig. 4, where we show 6 image sections of 1800 second long



Figure 2: *VYSOS 16* taking flatfield images in Summer 2012.



Figure 3: The intensity profiles of a point source as seen by the *VYSOS 16* CCD, using the old optics (left) and the new system (right). Each pixel has a size of $0''.79 \times 0''.79$. Both exposures are 5 second short and practically free of tracking errors. The color gradient scaling is linear from the count maximum down to the maximum value of the background noise as lower limit. The shape of the star in 2008 has an ellipsoidal strong center and a distorted ellipsoidal outer ring structure. In 2012, using a new main mirror, we were able to produce almost circular PSF.

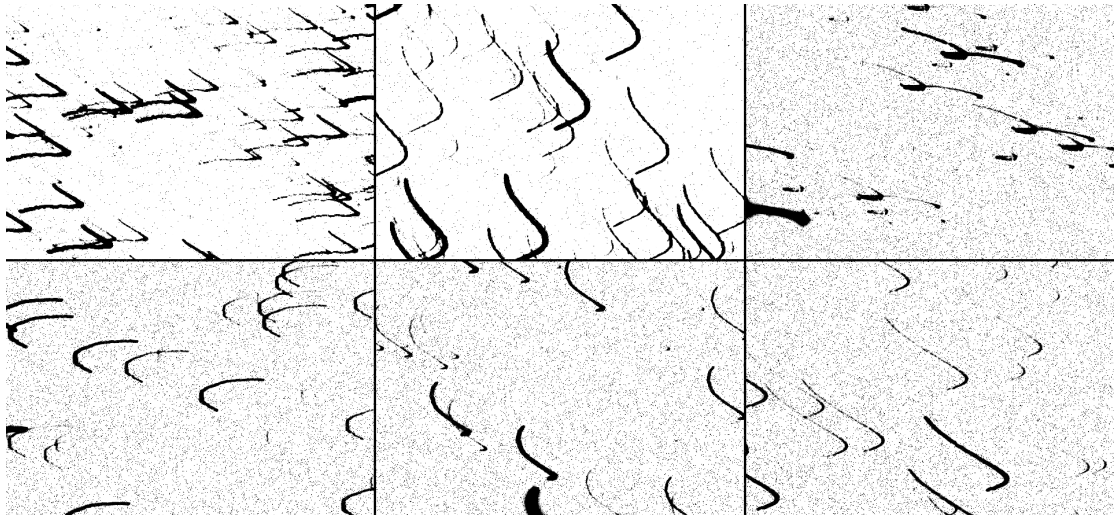


Figure 4: Six different 1800 second long exposures with *VYSOS 16* taken in 2012. They have been made with the newly configured optics but the old tracking system. Stars are traveling on trails that consist of circular and transversal motions across the image frame. Each having a size in the order of arcminutes.

exposures taken at different combinations of declination and hour angle respectively. The motions the stars follow can be generalized by a periodic component along both axes, resulting in a circular or ellipsoidal trail and an almost linear component (linear over the timescale observed here). The latter is caused by an erroneous pointing model, that does not compensate correctly for the positioning errors of the mount. Principal causes for these errors are the angular misalignment of the right ascension (α) axis relative to the earth rotation axis and the bending of mechanical elements of the mount (e.g. fork and tube), which will affect the orientation of the optics. The newly implemented model will be addressed in detail later in Sect. 2.2. The periodic error however could be caused by different reasons. For example one could expect the friction contact pinion of the positional encoders on the α axis to have a non-circular shape, causing periodic errors solely along the α axis. This is apparently not the major problem for our case, because as seen later in Sect. 2.1, Fig. 5, the movement is also along the declination (δ) axis with about the same offsets. This leads us to conclude that this effect must be caused by a problem in the bearing of the axis instead. In Sect. 2.1, we present the solution to resolve this issue by recording a model of this offsets in advance and applying this to the tracking loop of the telescope software.

In the following Chapter, I will briefly explain the improvements by the new telescope control software. The concept of the hard- and software design is presented in Sections A.1 and A.2 in the Appendix. Full details are documented in the *VYSOS 16* user handbook (Ramolla 2011).

An automatic script routine has been developed. It is capable to handle a given list of targets to be observed together with their calibration images, always considering environmental conditions of the observatory. Additionally, I have developed an automatic reduction pipeline for this data which will be explained below.

2.1 PERIODIC ERROR CORRECTION

In Figure 4, we have presented the problem that stars could not be tracked over long timescales and the long exposure images were delivering irregular startrails. There is a slowly, on timescales of several hours almost linearly drifting component, which is caused by the pointing model error. This is addressed later in Sect. 2.2. The other component, a periodic error on timescales of about 30 minutes, is already causing elongated stellar shapes on exposures of 30 seconds, but can be eliminated using the method presented in this Section.

The correction will be performed software-side. For this, we trace the positions of a star while tracking it over the complete visible time on the sky (for ~ 7 hours). Therefore we select a source close to 0° declination, because the offsets in the α direction are maximized there. Observations are starting as the object is 35° elevated in the east. The star is approximately centered in the CCD detector and every 10 seconds we take a new image, calculate the star's PSF and record the shift in α and δ of the center relative to the very first position. The results of this analysis are shown in Figure 5. Here we plotted the shifts of the star along the respective axis during tracking. The x -axis is the target hour angle (h) position on the sky. On the y -axis, the α and δ offsets of the target positions are drawn in arcseconds. A low frequency drift, stretching across the complete dataset, has been removed because it is just the residual error of the pointing model and not of interest here. The remaining periodic errors have a mostly well reproducible shape, except for some isolated bumps (e.g. at $h \approx 19^\circ$ in

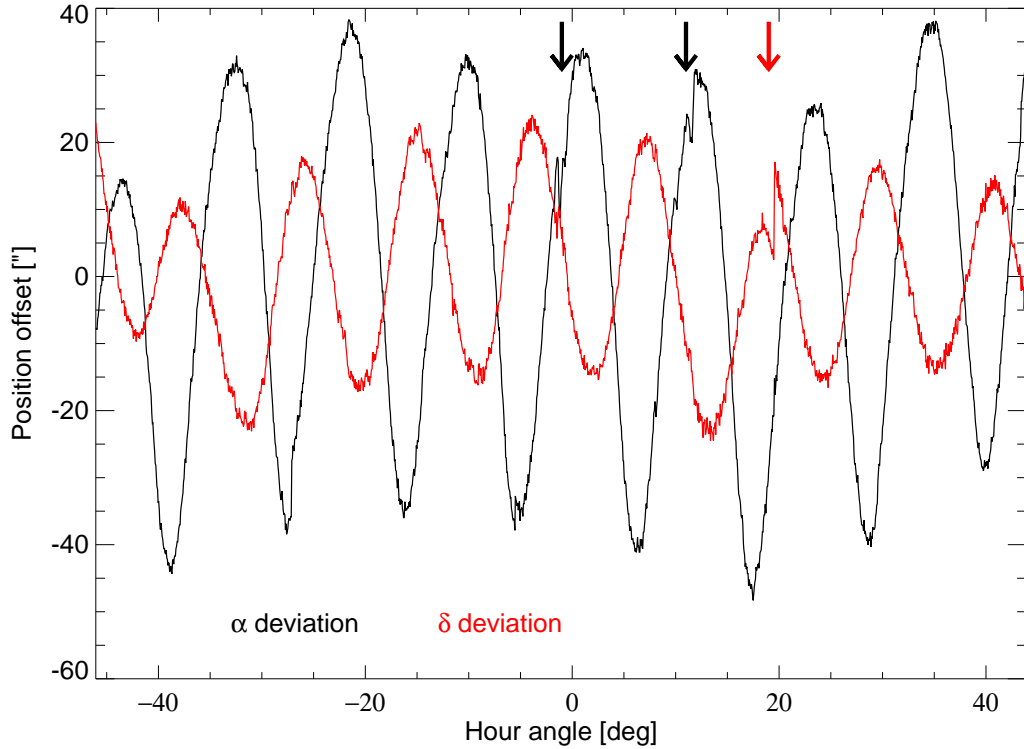


Figure 5: Periodically changing offsets of a stellar positions in α (black) and δ (red), while tracking a field during its period of visibility at $\delta \approx 0^\circ$. The low frequency deviation of the pointing model has been subtracted, hence the curves are not starting in the origin of the ordinates anymore. For illustration purposes this is irrelevant. The amplitude of $40''$ in the world coordinate system corresponds to 50 pixels on the detector. There are very fast changes in the positions of both axes, which are marked by arrows colored with respect to the axis in which they occur.

Fig. 5, marked by the red arrow). The appearance of these features is not predictable and they can happen on both axes independently. If an image is taken during such an event, bright stars are seen to be moving almost instantly very fast about several arcseconds, swinging into some final position. This must be caused by either mechanical instabilities or sand-grains in the bearing of the axes and it is too fast to be corrected for. The only solution is to discard and repeat images that suffer such a rare event. From the recorded offsets in Fig. 5 we obtained a model by removing the fast varying bumps and smoothing the curve with a 15 datapoints wide boxcar. The resulting smooth map of offsets is then directly supplied to the telescope server software.

Using these maps, generated tracking positions will now be corrected in-place for these offsets. If a precise pointing model is derived, based on these corrections, the tracking of *VYSOS 16* can stay within only one arcsecond over a period of 10 minutes.

2.2 POINTING MODEL

The pointing model equation for an equatorial mount is described in equations 1 and 2. IH and ID are the encoder index offsets. NP accounts for the misalignment between of δ and hour angle h . CH is the term for the misalignment between of the polar axis and declination axis (collimation error in east-west direction). ME is the coefficient for vertical misalignment of the polar axis. MA represents the azimuthal misalignment of the polar axis. TF represents the tube flexure and FO the fork flexure. A_1 and A_2 are additional terms, chosen to leverage slowly varying errors across the sky, however their physical origin is not clear and their impact on the pointing is only minor compared to the other coefficients.

$$\begin{aligned} \Delta h = & \text{IH} + \text{NP} \cdot \tan(\delta) + \text{ME} \cdot \sin(h) \tan(\delta) + \text{CH} \cdot \sec(\delta) \\ & - \text{MA} \cdot \cos(h) \tan(\delta) + \text{TF} \cdot \cos(\phi) \sin(h) \sec(\delta) \\ & + A_1 \cdot \sin(h) \cos(\delta) \end{aligned} \quad (1)$$

$$\begin{aligned} \Delta \delta = & \text{ID} + \text{ME} \cdot \cos(h) + \text{MA} \cdot \sin(h) \\ & + \text{TF} \cdot (\cos(\phi) \cos(h) \sin(\delta) - \sin(\phi) \cos(\delta)) \\ & + \text{FO} \cdot \cos(h) + A_2 \cdot \tan(\delta) \end{aligned} \quad (2)$$

Until a reliable pointing model had been computed, a very basic model of 2 star pointing was used by the mount. This model just interpolates linearly the coordinates between the two reference star positions. To compute the topocentric equatorial coordinates from the J2000 ones, the astronomy routines of the xephem¹ software package are used.

Measurements of pointing positions can either be taken within an approximately equidistant grid, or through pure random positions. The latter routine is currently implemented in the observation control software and can be called inside the observation scripts.

If a set of pointing observations is taken, the astrometry of these images is matched to the UCAC-3 catalog². This will result in offsets of α and δ to which we fit the above mentioned model. If only a single pointing observation is requested by the observer, the telescope will move to a field of high elevation and the obtained offsets to the catalog are directly applied to the pointing model offsets ID and IH in the current pointing model.

Figure 6 shows the targeted horizontal coordinates with calculated offsets and the pointing model correction for 97 points in an equally spaced grid with $\sim 10^\circ$ node distance. Note that the currently used model consists of a fit to 400 randomly chosen coordinates. However, this figure was selected as it demonstrates the nature of the offsets more clearly. Figure 7 shows the remaining residuals, when subtracting the model from the offsets. One can immediately see the drawbacks of selecting an ordered grid as base for the model fit, because systematic drifts are visible, which propagate with increasing number of the images taken. This particular dataset was taken in 2011 and the mechanics of the friction wheels of the axes were contaminated with small dust grains. These grains are able to let the positioning slip away from

¹ <http://www.clearskyinstitute.com/xephem/>

² http://ad.usno.navy.mil/ucac/readme_u3.html

time to time. The additional offsets, introduced by the slipping were simply adding up with the image numbers and as the order of the images was going in serpentine from north to south, the model will erroneously consider these systematics too, causing the patterns seen in Fig. 7. Instead, a random position selection will distribute these errors across the whole sky. Additionally, cleaning the axis mechanics in 2012 reduced the axis slipping to immeasurable small scales.

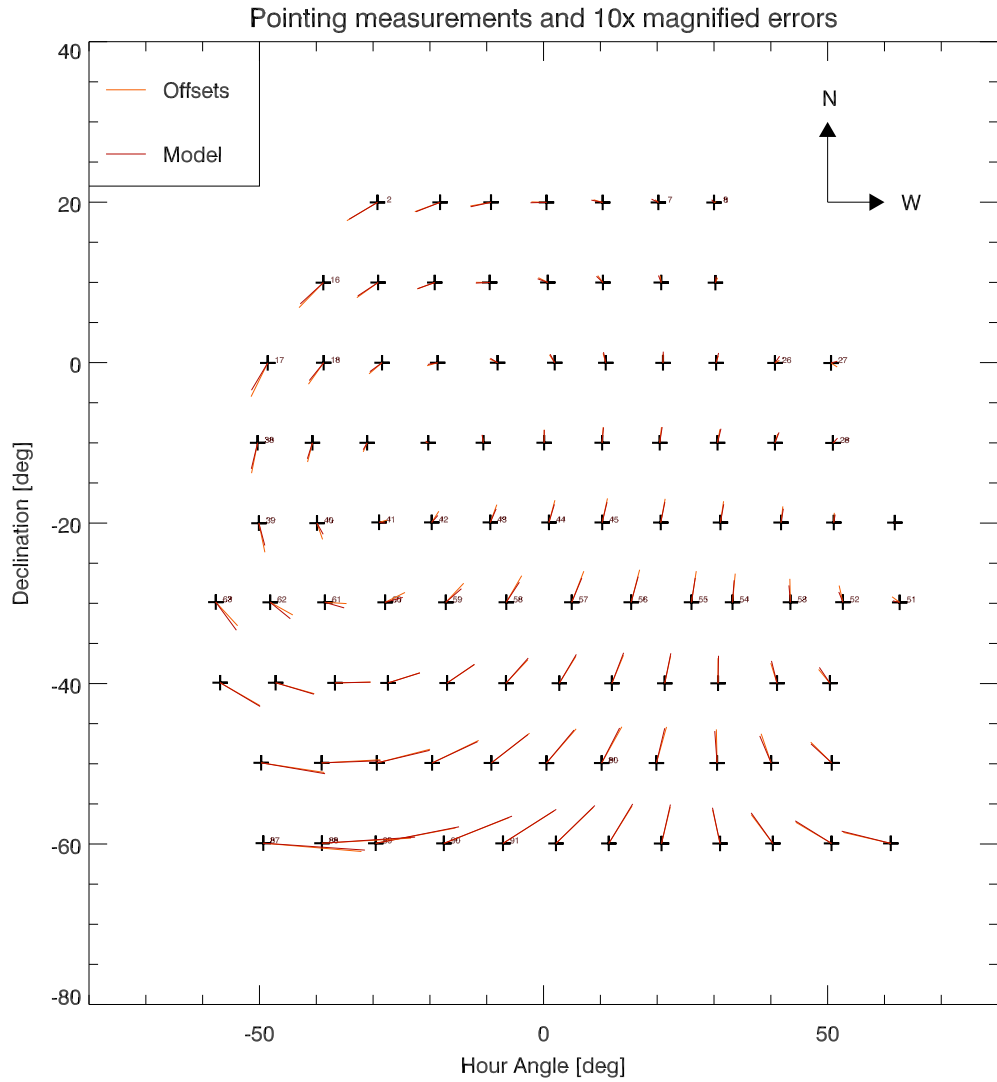


Figure 6: Overview of a complete set of pointing observations. Orange vectors are measured offsets from the reference coordinates (crosses) and red vectors are the corrections of the pointing model to it. These are ten times enlarged in this depiction. The observations were distributed over two nights, covering the sky with a serpentine slope each night. The gaps are caused by problematic images, where no reliable astrometric solution could be computed. Due to the strong axis slipping effects, some lines have systematically larger errors than others, visible by the numbering that is performed analogous to Fig. 7.

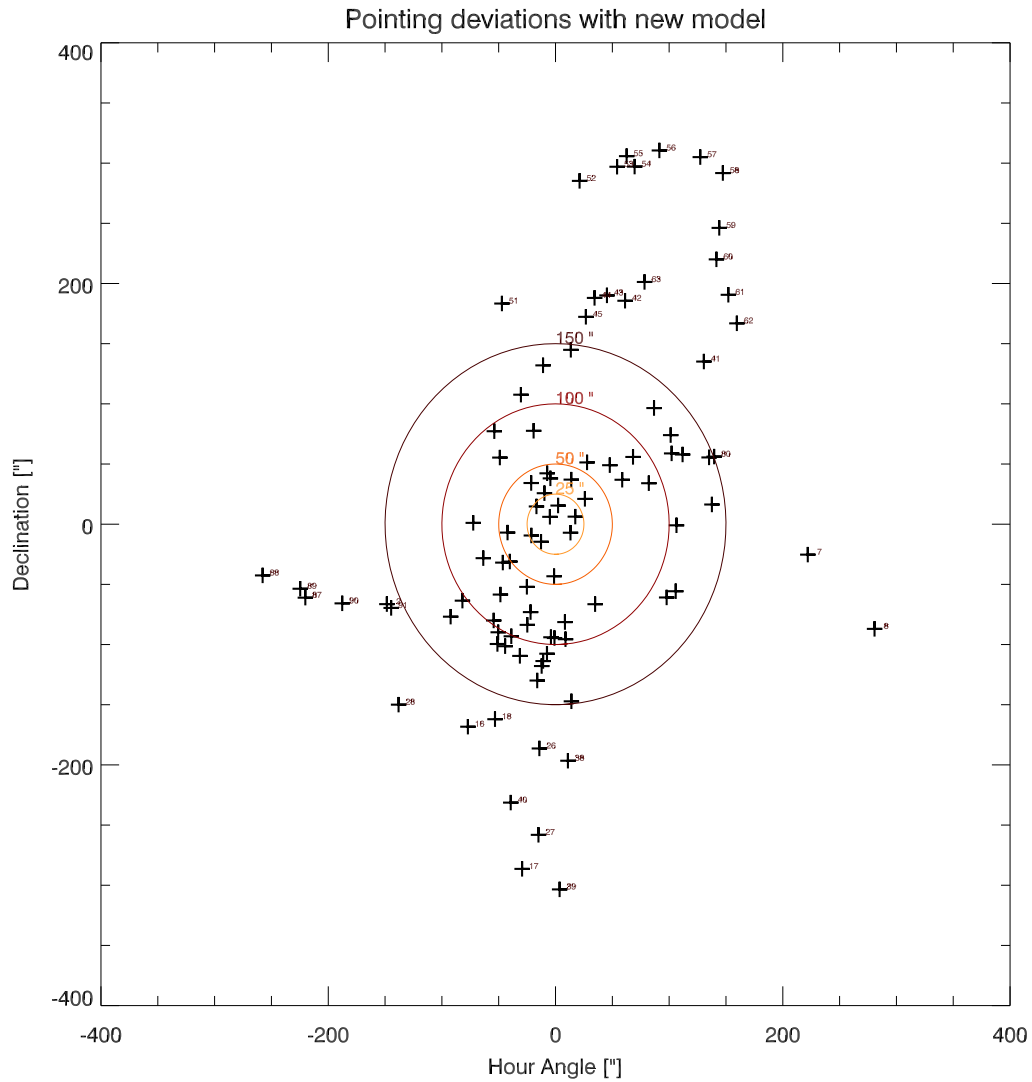


Figure 7: Accuracy of the pointing model: The residuals between model and astrometric offset of the images. Points are numbered corresponding to the logfile image numbers if they lie outside the 150 arcseconds boundary. The errors in this figure are far larger than the common periodic errors in α and δ of ~ 30 arcseconds. Large systematic offsets accumulate over time, while changing the mounts orientation. Obviously, the affected axis gears are slipping and losing counts. Thus, the pointing model will be shifted. It is also not clear how far backlash plays a role at re-positioning the axes.

2.3 DITHERING

The flatfield- and dark corrected image may contain cosmic rays, hot pixels, flatfield-errors and damaged columns or rows. These problems have to be accounted for before a reliable photometry is possible. Dithering around the selected target position poses a useful solution to this.

VYSOS 16 has a fixed dithering algorithm implemented in its software. The purpose is to maximize resolution enhancement potential in oversampling and to reliably eliminate detector errors and cosmic ray hits. The dithering will be executed along a predefined 9 point square pattern (see Fig. 8). Each point has a distance of 26.88 pixels to its next neighbors. This size is chosen to work around small scale detector errors and cosmic ray events, but also to avoid introducing large image loss at the borders or mixing different stray-light gradients in the field of view. The pattern is explicitly not aligned parallel with the axes of the CCD. This is to avoid problematic columns or rows in the image that would otherwise be stacking. The optimal angle of the rotation has been found to be $\approx 18.42^\circ$, which causes the projection of the pattern along the α or δ axis to have equidistant sampling with ≈ 8.5 pixel distance, thus ruling out all column and row errors being smaller than this. The pixel distance is also chosen in the

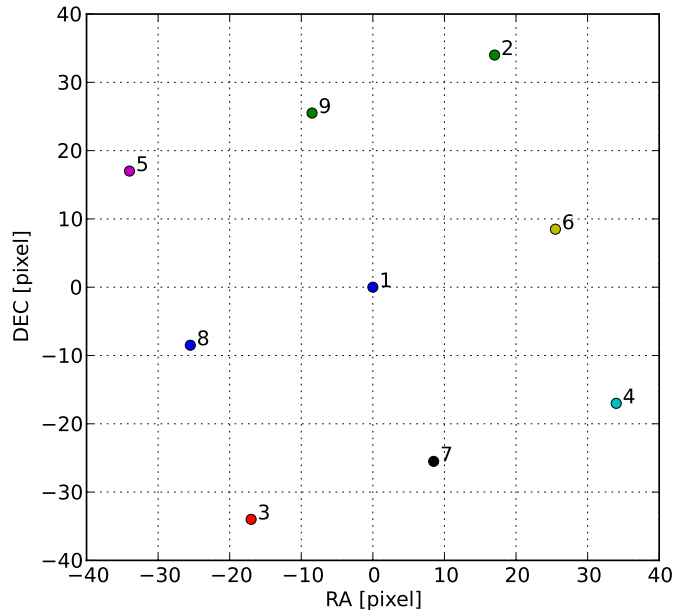


Figure 8: The offsets of the dither positions in the CCD detector coordinates (aligned to α and δ). The sequence is chosen to provide evenly distributed spatial coverage for lower numbers of total frames, like 3 or 5.

way that all collected images are taken with relative shifts of about $1/2$ pixel in α and δ direction, to improve the resolution in the re-sampling process, because later in the reduction pipeline, the different images of an observation block will be astrometrically matched to a reference grid. Hence, the dithering shifts will be removed completely before the images are stacked on a common grid. Figure 9 illustrates the pixel overlay on such a frame, free of the dithering shifts. The shifts have been optimized to provide

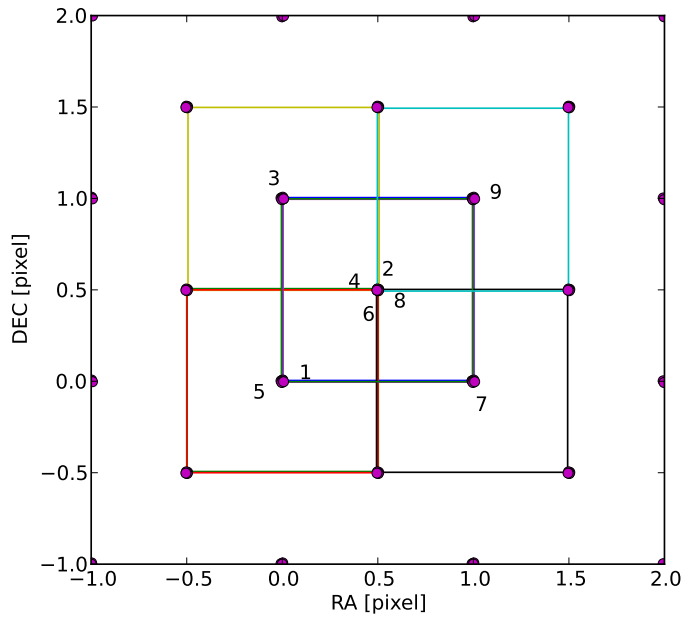


Figure 9: Spatial coverage of the sub-pixel shifts in the 26.88 pixel pattern in a common grid. The shifts have been truncated about the full-pixel shifts, so that only the relative sub-pixel shifts remain. In this manner, we have collapsed a 9 frame dither set. For every frame, we took a central pixel, touching the origin of ordinates and plotted its shape in a particular color. The magenta dots mark the centers of pixels. The coverage now is always in multiples of $1/2$ of the original pixel size.

half pixel offsets. Due to the astrometric matching of at least hundreds of sources in each image frame it is possible to exactly reconstruct the sub-pixel shifts.

The target grid for the re-sampling should have a higher resolution than the source images. In the case of half pixel shifts in the dithering, the resolution is doubled. The true resolving power of the images will be highly dependent on environmental observing parameters, like seeing or a good tracking during the exposure. The resolution gain will be the higher, the more the PSF on the source frames is under-sampled.

2.4 OBSERVATIONS

Observations of *VYSOS 16* are currently performed with predefined scripts that consist of a simple sequence of commands. A detailed list of usable script commands can be found in Sect. A.3, together with a small observation plan example in Sect. A.4, both in the Appendix.

The telescope control software is designed in the manner to detect critical situations and act accordingly. In the Appendix, Fig. 55, we present a flowchart describing the internal processes of the routine in detail.

Before moving to a source, environmental status is checked (currently controlled manually by the observer). If the weather conditions are poor, the observations will be halted and the telescope will move into the parking position and seal the optics. If conditions are good again, observations will continue, adapting for the time passed while waiting for good conditions. Checking the elevation of the target may have

the result that the target source will be below the lower limit for observations of 40° (before or after an potential exposure). If the source is below the limit, but it is about to rise, the script will wait for acceptable elevation. If the observation of this particular source is not possible anymore, it is skipped and the next task will be checked. Targets may also be skipped automatically, when the moon is too close (withing 10°), as this would allow too much stray light into the optical system, resulting in poor photometry.

This adaptive behavior is also utilized when taking sky flatfield images. At the beginning of dusk, the telescope will move 20° pointed away from zenith in the east (at dawn it is 20° in the west). After stabilizing the detector with several dummy readouts, the exposure time will be adapted so that the selected filter produces an image with a median of about 40 000 counts. If a good first exposure time is found, the control software assumes a known decrease profile of sky brightness to calculate the exposure time for the next frame, instead of further experimenting with different exposure times. As a result, there are almost no flatfield images that have to be discarded because of too low or too high counts and we are able to take at least 10 flatfields per night in each filter during dusk and dawn. At dawn, the routine naturally assumes an inverted profile for increasing brightness of the sky. The stability of the flatfield script allows to detect cloudy weather conditions, when the median counts are deviating too much from the known profiles.

We also designed a routine that is able to predict the telescope's behavior, considering the observability of the sources on the sky and instrumental overheads (e.g. filter changes and focusing). This routine allows the observer then to optimize his observation plans, or to detect problems, such as critical proximity of the moon. Fig. 56, in the Appendix, depicts the simulated observation properties of a typical night.

2.5 REDUCTION PIPELINE

The data is automatically transferred to servers in Bochum each night. Then, an automatic pipeline will inventorize them and start the reduction process for the observations, as illustrated in Fig. 57, in the Appendix. First, calibration images will be gathered from before and after the observed night of interest. If no data is existing, the calibration images from the night before will be used instead. The raw science frames are bias (20 frames/night), dark (20 frames/night) and flatfield (10 frames/night/filter) corrected in a standard manner using IRAF scripts. Then, *SourceEXtractor*³ is used to extract a catalog of positions of sources, in order to match them with an UCAC-3 astrometry reference catalog⁴. This is performed using *Scamp*⁵, which also determines image projection and distortion parameters. If these cannot be determined satisfactory, median values are used instead. These median values have been determined from analyzing a set of astrometric results with high confidence. In Fig. 58, in the Appendix, we show the median results for the 670 nm filter for 10699 high quality field matchings of the pipeline.

Provided the image offsets and distortion correction, we can now apply *Swarp*⁶. Using this tool, the images are then re-sampled to a new grid with a pixel size of $0''.39 \times 0''.39$ that is perfectly aligned to the ordinates of the world coordinate system.

³ <http://www.astromatic.net/software/sextactor>

⁴ http://ad.usno.navy.mil/ucac/readme_u3.html

⁵ <http://www.astromatic.net/software/scamp>

⁶ <http://www.astromatic.net/software/swarp>

Using the IRAF task “imcombine”, the image-sets are then combined with min/max rejection, to eliminate dead pixels, or cosmic ray events. Compared to pure median combination, this average yields a better signal-to-noise ratio. In Fig. 10 we demonstrate the imaging quality that we can achieve now with *VYSOS 16* on ESO 374-G25. Its resolution is comparable to a Digitized Sky Survey (DSS) image of the Palomar Schmidt telescope with an 1.26 m effective aperture.

2.6 SCIENCE VERIFICATION

Currently, a dozen AGN and 42 variable young stars are being monitored using *VYSOS 16*. The first results of these projects are already very promising. For example, Fig. 11 shows lightcurves in broad and narrow bands of the faint Sy1 galaxy RXJ1741.4+0348 (Ramolla et al. 2013, in preparation). The good quality of the curves allows us to see the time delay of the 670 nm NB (potentially dominated by the $H\alpha$) to the *B* band continuum variation by eye to be about 16 days (marked by the black arrows in Fig. 11).

Figure 12 shows another science verification result for the eclipsing binary star CPD-41°7742. The photometric data, kindly reduced by Angie Barr Dominguez, was obtained in about 2 months of observations in Summer 2012 and our result of 2.44 days agrees perfectly with the value determined by Sana et al. (2005). To conclude, the *VYSOS 16* telescope can now be used as a comfortable and reliable instrument for variability studies.

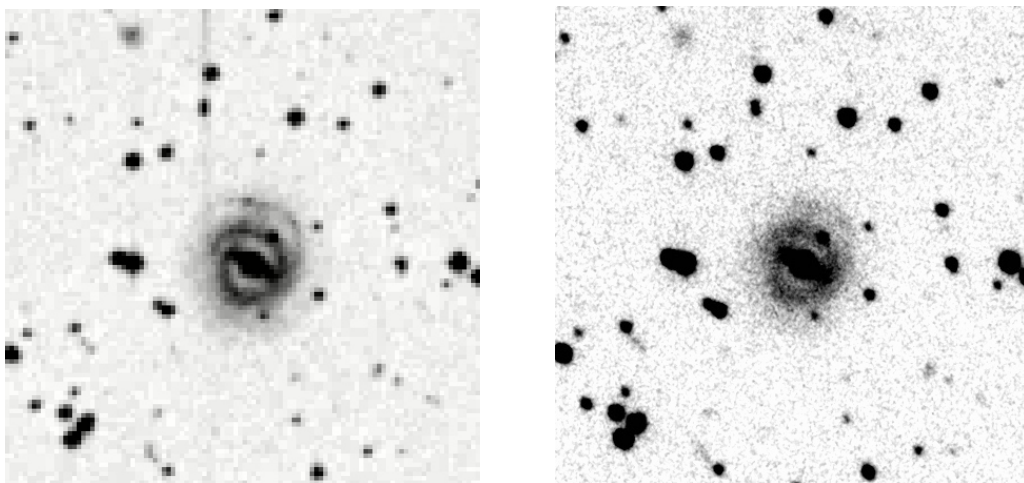


Figure 10: Comparison between V band images from the POSS1 survey (left) and *VYSOS 16* (right) for ESO 374-G25. Note that the effective aperture of the Palomar Schmidt telescope is 1.26 m, more than three times larger than *VYSOS 16*. Stellar profiles in the right-hand image have a lower effective resolution ($3''.2$ FWHM of point sources, compared to $2''.9$), but the PSF profiles have very pronounced smooth shapes due to the resampling of the images. The digitized POSS1 was obtained from the NED. Both images span $5' \times 5'$.

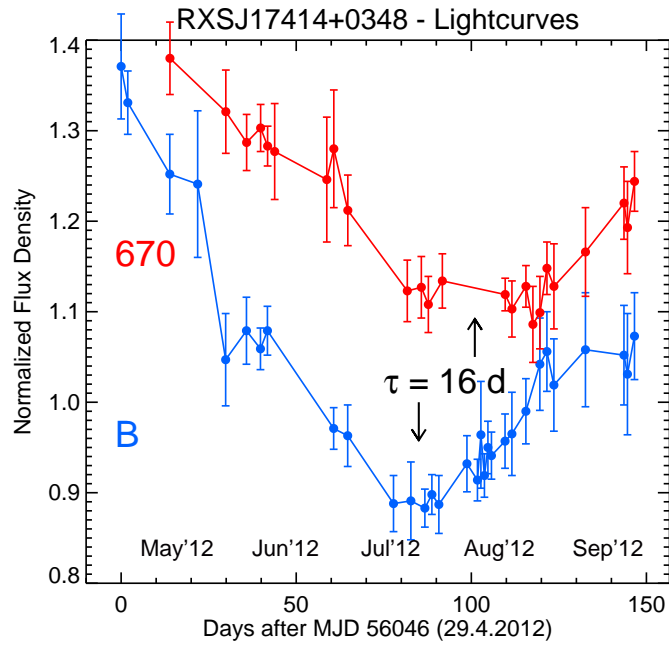


Figure 11: Preliminary lightcurves of RXJ1741.4+0348 in Johnson B band (blue) and 670nm NB (red). The last datapoint in this Figure is from September 23th 2012. All data has been taken with the *VYSOS 16* telescope alone. Fluxes are normalized to their average flux and the NB is shifted 0.4 units upwards.

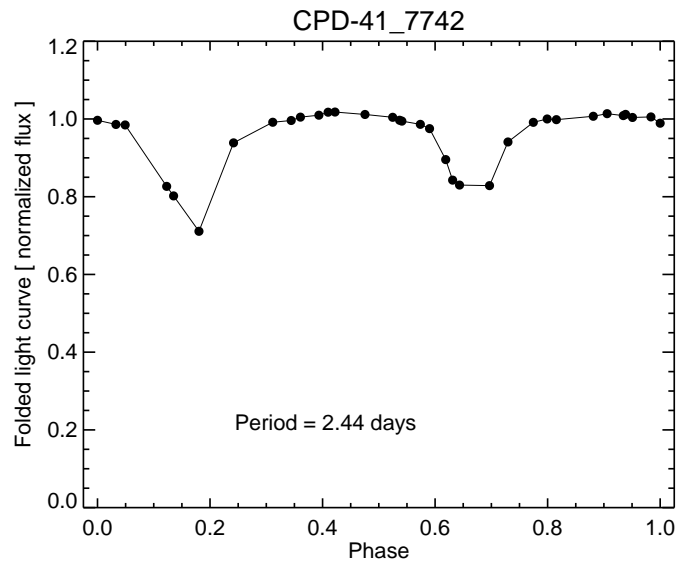


Figure 12: Phase diagram of the O-star CPD-41°7742. The phase used in this diagram is 2.44 days. The photometric errors are in the order of the symbol sizes.

PHOTOMETRIC REVERBERATION MAPPING

3.1 PHOTOMETRIC OBSERVATIONS

All photometric observations were performed with three robotic telescopes: The 15 cm *VYSOS 6*, the 40 cm *VYSOS 16* and the 25 cm *BEST II* telescopes on Cerro Armazones in Chile. The filter configuration of the telescopes is shown in Table 2, Appendix. Time frame, sampling rate and filter selection are given in Table 1, respectively for each object and epoch.

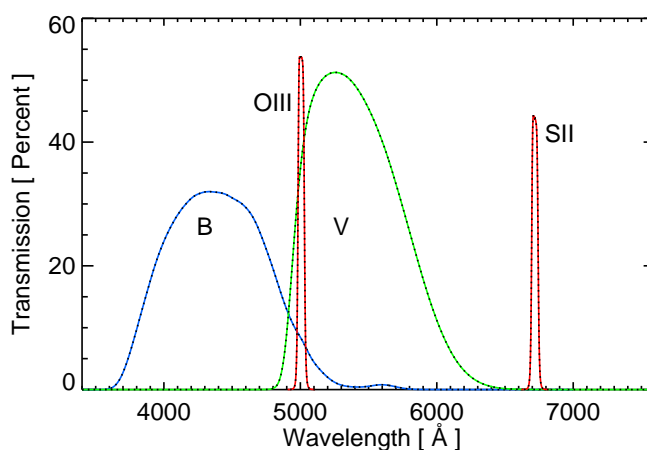


Figure 13: Effective transmission of the *VYSOS 6* filters convolved with the quantum efficiency of the ALTA U16M CCD camera.

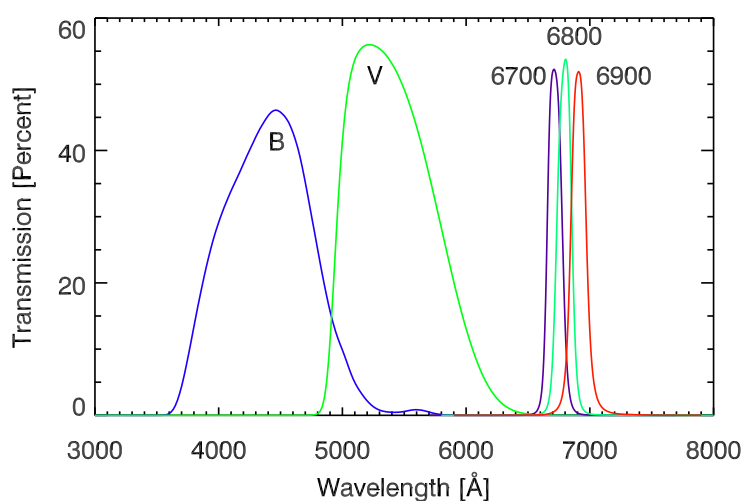


Figure 14: Effective transmission of the *VYSOS 16* filters convolved with the quantum efficiency of the Kodak 6303E.

Table 1: Characteristics and observational history of our photometric reverberation mapping campaign.

| Name | Observation epoch | | Filters ⁽¹⁾ | Median sampling (days) | $z^{(2)}$ | $D_L^{(2)}$ (Mpc) | $fB^{(3)}$ (mJy) | $fV^{(3)}$ | $A_B^{(4)}$ | $A_V^{(4)}$ (mag) |
|-------------|-------------------|---------|--|---------------------------|-----------|----------------------|---------------------|------------------|-------------|----------------------|
| | from | until | | | | | | | | |
| 3C120 | 10/2009 | 03/2010 | $B_j^{(b)}, V_j^{(b)}, [\text{OIII}]^{(b)}$ | 2 | 0.0330 | 145 | 7.02 ± 0.35 | 9.26 ± 0.41 | 1.283 | 0.986 |
| Ark120 | 10/2009 | 03/2010 | $B_j^{(b)}, V_j^{(b)}, [\text{OIII}]^{(b)}$ | 2 | 0.0327 | 138 | 15.09 ± 0.73 | 18.18 ± 0.57 | 0.554 | 0.426 |
| ESO 374-G25 | 04/2011 | 07/2011 | $B_j^{(b)}, r_s^{(b)}, [\text{SII}]^{(b)}$ | 3 | 0.0237 | 103 | 1.00 ± 0.08 | – | 0.446 | 0.343 |
| ESO 374-G25 | 03/2012 | 04/2012 | $B_j^{(a,b,c)}, V_j^{(a,c)}, [\text{SII}]^{(b)}, 670 \text{ nm}^{(c)}$ | 1 | " | " | 1.06 ± 0.04 | 2.11 ± 0.03 | " | " |
| PG0003+199 | 08/2009 | 12/2009 | $B_j^{(b)}, V_j^{(b)}, [\text{SII}]^{(b)}$ | 2 | 0.0258 | 103 | 6.24 ± 0.31 | 7.95 ± 0.31 | 0.153 | 0.118 |

1: Filters as listed in Table 2. Used with these telescope associations:

a) *BEST II*

b) *VYSOS 6*

c) *VYSOS 16*

2: Values from NED database.

3: Extinction corrected fluxes.

4: Extinction coefficients by Schlegel et al. (1998).

3.1.1 VYSOS6

VYSOS 6 features two identical 15 cm refractors on a German equatorial mount. Each tube has a filterwheel with 7 slots and one 4098×4098 pixel CCD camera¹. For VYSOS 6, the field of view is a $2^\circ 42' \times 2^\circ 42'$ square, with a pixelsize of $2''.37 \times 2''.37$. The association of the filters to the two refractors is given in Table 2 (Appendix). Additionally, the convolution of our applied filters with the quantum efficiency of the CCD is depicted in Fig. 13.

3C120 was observed between October 2009 and March 2010 with a median sampling of two days in the B and V bands and the [O III] $\lambda(5007 \pm 30)$ Å narrow band. For Ark120 and PG0003+199, we obtained light curves with a median sampling of two days in the B band (Johnson, 4330 ± 500 Å), the redshifted $H\alpha$ (NB 6721 ± 30 Å at $z = 0.0258$) and $H\beta$ lines (NB 5007 ± 30 Å at $z = 0.0327$) between August 2009 and March 2012. For Ark120 we also obtained a light curve in the V band (Johnson, 5500 ± 500 Å). In addition, we observed PG0003+199 in both B and V on July 25, 2010 and June 26, 2011. Figure 13 shows the effective transmission of the filters used here. To perform absolute photometric calibration, each night we observed standard stars in the fields SA092, SA095, SA111 from Landolt (2009).

ESO 374-G25 was observed during 2 epochs in 2011 (April until June) and 2012 (February until April) with VYSOS 6 in B_J , r_S and the [S II] narrow band filter with a median sampling of 3 and 1 days.

3.1.2 VYSOS 16

VYSOS 16 is a 40 cm Coudé reflector telescope, mounted on an equatorial mount. It has a 5 slot filterwheel installed inside a 3072×2048 pixel CCD camera². Further specifications of VYSOS 16 are detailed in Chapter A.1. The association of the filters is found in Table 2 (Appendix). Additionally, the convolution of our applied filters with the quantum efficiency of the CCD is depicted in Fig. 14.

The telescope was used to observe ESO 374-G25 in 2012 between the 2nd April until 20th May. At the end of May, the object was too late to be observed for a longer period, hence the total lightcurve is rather short. The observations were performed using Johnson B , V and the 670 nm narrow band. Unfortunately, due to difficult weather conditions and hardware problems with the mounting of the Telescope³, we could not obtain a good time resolution first. Although the sampling in the observation plans was chosen to be one day, the actually observed sampling has gaps of several days up to two weeks. The planning schedule allowed to use both Johnson B and V and 670 nm. In all filters, we also observed the standard star field SA111 from Landolt (2009).

3.1.3 BEST II

BEST II features a Newton reflector telescope with 25 cm diameter mirror on a German equatorial mount. Images are acquired by a CCD⁴ with 4096×4096 pixel, that has a

¹ Apogee Alta U16M

² Kodak 6303-E

³ Caused by a loose plastic distance holder influencing the gearing of the δ axis.

⁴ FLI ProLine 16801

pixel scale of $1''.5 \times 1''.5$, resulting in a field of view of $1^\circ 42' \times 1^\circ 42'$. The association of the filters is found in Table 2 (Appendix).

During the second observation epoch of ESO 374-G25 (in 2012), supplemental observations have been conducted with the BEST II telescope in B and V band because VYSOS 16 was not available before April 2012, and the usage of the V band filter was not possible at VYSOS 6 due to the tight scheduling on this instrument. This was intended primarily to provide a photometric lightcurve in the same epoch, when the spectra by Wolfram Kollatschny and Matthias Zetzl were taken at SALT.

Having B and V band photometry with the same instrument was necessary for the later FVG analysis (Sect. 3.5.3). The narrow dataset of VYSOS 16 alone did not allow a reliable fit of the AGN color gradient.

3.2 PHOTOMETRY

All data were reduced in a standard manner, using IRAF and custom written tools. Because the flux calibration using the standard star fields introduces additional errors into the light curves, we created relative light curves (in normalized flux units) using 10–30 non-variable stars located on the same images within $30'$ around the AGN and with a similar brightness to the AGN. For analyzing time lags we used the mean and standard deviation of these relative light curves. For the photometric analysis (to obtain the AGN luminosities), we kept the shape of the mean light curves fixed and cross-calibrated them by a least-squares fit to the photometry derived from the standard star fields.

Photometry is obtained using apertures of $7''.8$ for PG0003+199 and $7''.5$ for all other objects. For the absolute photometry, the errors for individual measurements are determined from the above-mentioned standard deviation of the relative lightcurve and the cross calibration with photometric reference stars from Landolt (2009). For this, the atmospheric (For the nearby site Paranal by Patat et al. 2011) and galactic foreground extinction (Schlegel et al. 1998). Afterwards, the fluxes are converted to mJy, with results listed as f_B and f_V in Table 1.

For VYSOS 16 we have used the same aperture of $7''.5$ in our analysis. This aperture has been set in order to allow a photometry that is more sensitive to the nuclear flux than the surrounding host. Expanding the aperture to a size that also covers the complete host will introduce too much detector noise for our faint sources and the calibration stars.

Selecting a small aperture, however, can be problematic if the image was observed under poor conditions (e.g. strong wind), so that the PSF is elongated. This will drive nuclear flux out of the aperture, while the spatially broad distributed host flux stays more or less constant. If images with these defects are detected, they will be rejected for the FVG analysis to avoid this systematic error.

3.3 SPECTROSCOPIC OBSERVATIONS

Here we briefly describe the spectrographs that have been used to observe the four AGN presented in this thesis in addition to our photometric campaign.

3.3.1 Robert Stobie Spectrograph at the South African Large Telescope

In a joint project with Wolfram Kollatschny and Matthias Zetzl, Georg-August- Universität Göttingen, a dedicated list of AGN will be monitored photometrically from the USB in Chile and spectroscopically from SALT. One of these objects is ESO 374-G25- During our VYSOS 16 monitoring ten optical spectra have been taken between 15th of February and 17th of April 2012. Standard reduction procedures were performed by Matthias Zetzl. The RSS features optical and IR spectroscopy using a Volume Phase Holographic (VPH) grating. In the optical it covers approximately a wavelength range of 3200 Å to 9000 Å, having a resolution between 500 and 10 000. The slit dimensions were $2'' \times 8'$ rotated to the parallactic angle of the object.

3.3.2 Calar Alto Faint Object Spectrograph

CAFOS is situated at the 2.2 m telescope in the German-Spanish Astronomical Center on the mountain Calar Alto in Spain. It was used with the B400 grism, giving a wide wavelength coverage from about 3600 Å to 8500 Å with an dispersion of 10 Å per pixel on the used SITe1d CCD. In October 2009, of 3C120, Ark120, PG003+199 and a standard star, a single contemporaneous spectrum was obtained, respectively with a slit width of $1''.54$. I reduced the spectra using standard IRAF routines.

3.4 SPECTRA AND VELOCITY DISPERSIONS

In this Section we present the analysis of the spectroscopic data that have been obtained in the epochs of our photometric campaigns for each object respectively.

3.4.1 PG0003

Figure 15 shows the spectrum of PG0003+199. The contribution of higher order Balmer lines (and that of the host galaxy) to the B band is negligible, thus the B band is dominated by the AGN continuum. From the $H\alpha$ profile in this spectrum, we can calculate line dispersion using equations 3 and correct these for the resolution of the spectrograph ($\sigma_{\text{Observed}}^2 = \sigma_{\text{Line}}^2 + \sigma_{\text{Instrument}}^2$). To obtain the velocity dispersion, we use the equation for relativistic Doppler shift (4).

$$\sigma_{\lambda}^2 = \frac{\int (\lambda - \lambda_0)^2 P(\lambda) d\lambda}{\int P(\lambda) d\lambda}, \quad \lambda_0 = \frac{\int \lambda P(\lambda) d\lambda}{\int P(\lambda) d\lambda} \quad (3)$$

$$\frac{\lambda_0 + \sigma_{\lambda}}{\lambda_0} = \sqrt{\frac{c + \sigma_v}{c - \sigma_v}} \quad (=) \quad \sigma_v = c \frac{\left(\frac{\lambda_0 + \sigma_{\lambda}}{\lambda_0}\right)^2 - 1}{\left(\frac{\lambda_0 + \sigma_{\lambda}}{\lambda_0}\right)^2 + 1} \quad (4)$$

When taking the spectral resolution into account, the observed $H\alpha$ line dispersion $\sigma = 1300$ km/s reduces to an intrinsic value $\sigma = 870$ km/s. The narrow band filter effectively covers the line between velocities -2800 km/s and $+1800$ km/s, so that at least 95% of the line flux is contained in the pass band, as we determined after line profile deconvolution.

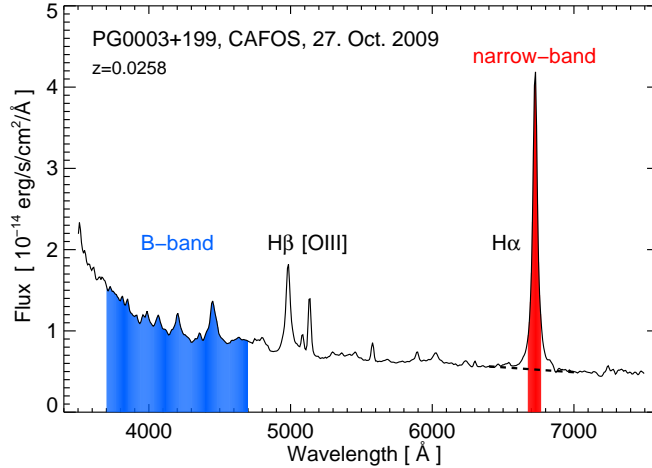


Figure 15: Observed spectrum of PG0003+199. The B band (blue shaded) traces essentially the AGN continuum, while the narrow band (red shaded) is dominated by the $H\alpha$ line. The blue and red shaded areas are a schematic illustration, and quantitative calculations were made using the transmission curves shown in Figure 13.

PG0003+199 is essentially a point-like, low-luminosity quasar (Narrow Line Seyfert-1) without a bright extended host. The $H\alpha$ line is strong and well covered by the narrow band filter. This makes PG0003+199 a clear-cut test case.

The contribution of both the $[NII]$ 6583 Å and narrow-line $H\alpha$ flux is predicted to be less than 40% of the $[OIII]$ 5007 Å emission (Bennert et al. 2006), hence negligible ($< 10\%$). The continuum underneath the emission line is small, contributing to only 15% of the total flux in the band pass, therefore the narrow band light curves will be dominated by the $H\alpha$ echo of the BLR gas clouds. Comparison with simulated line profiles of echo models (Welsh and Horne 1991 Horne et al. 2004) ascertains that the 5% line flux outside the band pass only has a marginal effect ($< 2\%$) on the BLR size determination: The narrow band echo may miss only a small fraction ($< 20\%$) of the innermost part of the BLR, namely the part that exhibits the fastest line-of-sight velocity, while the innermost gas clouds moving closer along the sky plane exhibit a modest line-of-sight velocity and are therefore contained in the narrow band.

3.4.2 *Ark120*

Ark120 lies at redshift $z = 0.0327$ so that the $H\beta$ line falls into the $NB5007 \pm 30$ Å filter. Compared to the case of PG0003+199, the observations of *Ark120* are more challenging: First, compared to $H\alpha$, the $H\beta$ line is fainter contributing only to $\sim 50\%$ of the flux in the NB band pass (Fig. 16). To measure the continuum variations underneath the $H\beta$ line, light curves using neighboring off-line intermediate bands would be ideal, but such bands were not available. While the V band covers $H\beta$ and the Fe complex, it is dominated to $83\% \pm 3\%$ by the AGN and host continuum (calculated using the transmission curve of filter and CCD shown in Fig. 13), so we used the V band, in addition to B band and $NB5007$ Å. The second challenge is that (after accounting for the spectral resolution) the $H\beta$ line is broader than the narrow band pass, so that the broadest line wings, carrying about 10 – 15% of the line flux, escape detection in the NB. Despite these handicaps, the results are promising.

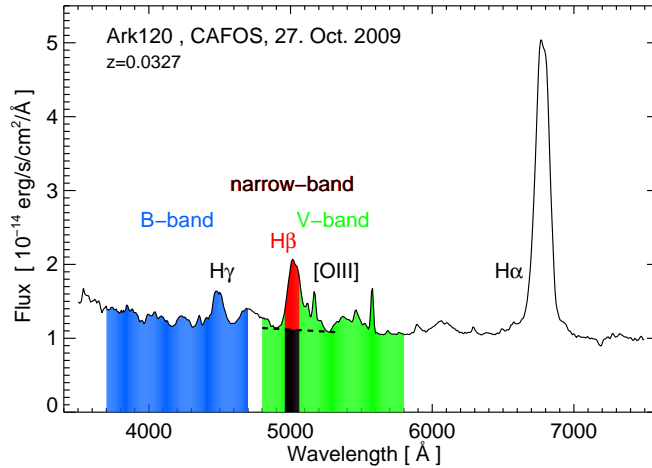


Figure 16: Observed spectrum of Ark 120. The B band (blue shaded) traces the AGN (and host) continuum and a small ($< 5\%$) contribution by $H\gamma$. The V band (green shaded) traces the continuum and a small ($< 15\%$) contribution by $H\beta$. The narrow band traces the continuum (black shaded) and $H\beta$ (red shaded), each component contributing to about 50% to the band pass. The red wing of $H\beta$ extending beyond $[O III]$ is neither seen in $H\alpha$ nor in $H\gamma$ and could be due to Fe lines (Korista 1992). For the effective transmission curves of B and V see Figure 13.

Already in the 1970s and 1980s, numerous studies revealed that the $H\beta$ line profile of Ark120 is strongly variable and exhibits two peaks in the rms spectra and a prominent red wing, which is present neither in $H\alpha$ nor in $H\gamma$ (Fig. 16). As discussed by Doroshenko et al. (1999), the BLR of Ark120 may show accretion inflows in addition to the virialized motion, and therefore any black hole mass estimates should be considered with some reservation.

3.4.3 $3C120$

$3C120$ lies at redshift $z = 0.0331$, so that the $H\beta$ line also falls into the $[O III] \lambda(5007 \pm 30)\text{\AA}$ filter, as Figure 17 shows. The $[O III]$ filter covers the line between velocities -3800 km/s and $+2200\text{ km/s}$. About 95% of the line flux is contained in the $[O III]$ filter through line profile deconvolution.

The spectral plot shows that about 50% of the continuum and 50% of $H\beta$ emission line is contributing into the narrow band filter.

The narrow emission lines $[O III] 4959, 5007\text{\AA}$ were modeled by single Gaussian profile and afterward subtracted from the single epoch spectra (Denney et al. 2009). We also considered the theoretical intensity ratio for this doublet of 2.98, determined by Storey and Zeippen (2000) and consistent with observational measurements, which exhibit a negligible intensity variation (Dimitrijević et al. 2007). A more sensitive case occurs removing the narrow component of the $H\beta$ profile. This can only be performed under the assumption of standard emission-lines ratios, which allow to model this contribution (Denney et al. 2009). We follow the same procedure as in Denney et al. (2009). The $[O III] 5007\text{\AA}$ line profile was used to create the model of the narrow emission, taking into account that the narrow component consists of about 10% of the $[O III] 5007\text{\AA}$ narrow line flux (Woo et al. 2007). This model was then subtracted from the $H\beta$ line.

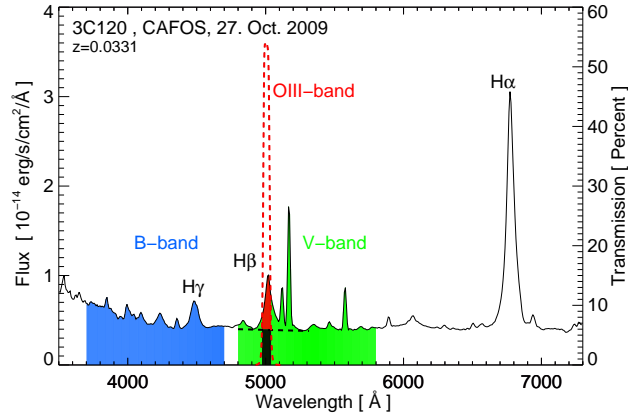


Figure 17: CAFOS spectrum of 3C120 obtained on Oct.27 2009. The effective filter transmissions are indicated; the transmission for the NB filter has been convoluted with the quantum efficiency of the ALTA U16 CCD camera. As an schematic illustration we show the AGN continuum (*B* band) and the narrow band ([O III] band) dominated about 50% for the H β emission line (red shaded) and 50% for the continuum (*V* band, black shaded).

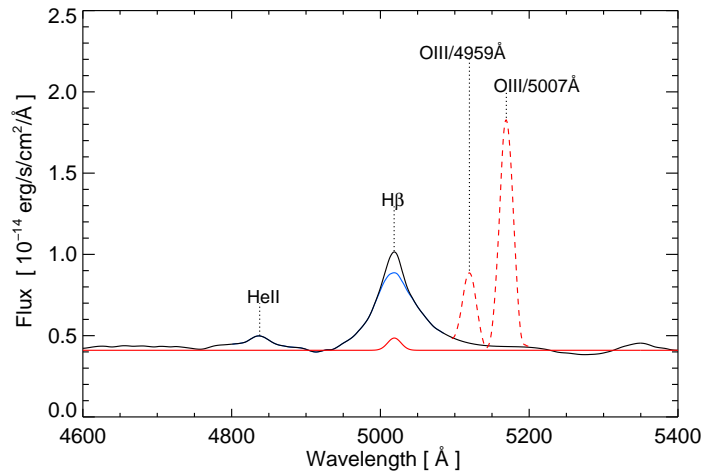


Figure 18: CAFOS spectrum of 3C120 zoomed in on the region around the broad H β emission line. The solid black curve represents the spectrum after subtracting the narrow [O III] 4959, 5007 Å emission lines (red dashed lines). The dashed red line (at the bottom of the H β profile) shows the narrow H β model, for 10% intensity of the [O III] 5007 Å line. The solid blue line represents the spectrum after subtracting the narrow H β models. Note that the broad faint He II 4686 Å emission line can be clearly seen, but its possible contribution to the H β profile is negligible.

Figure 18 shows the original $H\beta$ 4861 Å profile together with the narrow emission lines subtracted.

Once the narrow lines were removed, the $H\beta$ profile was isolated by the subtraction of a linear continuum fit, obtained through interpolation between two continuum segments on either end of the line, taking into account the possibility of local continuum contamination by FeII contribution and the red wing of the He II 4686 Å emission line (which may be blended with the blue wing of $H\beta$). This process was performed on the original (without subtraction of narrow lines) and corrected spectrum (narrow lines subtracted), in order to compare both results⁵. The velocity dispersion after removal of narrow lines is $\sigma_{\text{line}} = 1264$ km/s, consistent with $\sigma_{\text{line}} = 1166$ km/s obtained by Peterson et al. (2004). From a more recent spectroscopic reverberation campaign, Grier et al. (2012a) determined $\sigma_{\text{line}}(\text{mean}) = (1687 \pm 4)$ km/s and $\sigma_{\text{line}}(\text{rms}) = (1514 \pm 65)$ km/s. We should note that the narrow $H\beta$ component, in the mean spectra obtained by Grier et al. (2012a) (their Fig. 1), is clearly contributing to the $H\beta$ profile, which suggests that an underestimation of our subtraction would turn our velocity dispersion underestimated too, considering the possible systematic effects detected from single epoch spectra (Denney et al. 2009). On the other hand, our time lag is about 40% smaller than the result derived by Peterson et al. (2004). Hence, according to photo-ionization physics, the $H\beta$ region is closer to the ionizing source and in consequence higher velocities of the gas clouds are expected.

3.4.4 ESO 374-G25

ESO 374-G25 is a key target in the joint photometric/spectroscopic RM project. The spectra allow us to determine the kinematics of the $H\alpha$ line for our second photometric observation run in 2012.

Figure 19 shows the quick-look spectra of ESO 374-G25, taken with the RSS at the SALT. They have been reduced and intercalibrated by Matthias Zetzl. The relative intercalibration has been performed by assuming constant shape and flux of the 5007 Å [O III] line. Hence, the spectra are shifted in wavelength and scaled in flux. The dispersion axis spreads across an array of 3 CCDs. One border lies at ~ 5300 Å and the other one at ~ 6400 Å.

The upper Figure depicts an approach to estimate the host color. From the two-dimensional spectral image, two different apertures were used for extraction. ESO 374-G25 has a well resolved host (see Fig. 10). The smaller aperture of $\sim 7''.1$ is chosen to cover the nuclear region as completely as possible while minimizing the host contribution. The larger aperture of $\sim 30''.7$ was intended to catch more of the host flux around the nuclear region.

The green difference spectrum (large minus small aperture, multiplied by 3) indicates that the surrounding host galaxy is bluer than the nuclear region. As expected, the broad Balmer lines are much weaker. The remaining broad component presumably comes from the outer PSF wings of the nucleus stretching out to our outer aperture. The bluer colors in the outer regions can be interpreted as differences in the average stellar evolution in the regions we are looking upon. This means, the bulge-like center (although tightly overlaid with the blue but weak AGN) has an old and red stellar population, while the outer blue ring shows the young regions of starformation. In

⁵ If the narrow lines were not removed, the velocity dispersion would be too high ($\sigma_{\text{line}} = 1405$ km/s).

the spheroidal galaxies analyzed in Barway et al. (2005), these color properties of the galaxies were seen too.

With a redshift of $z = 0.0237$ (Theureau et al. 1998), the $H\alpha$ line falls mainly into our 670 nm and [S II] narrow band filters. The red wing is also visible in the 680 nm filter. In the lower Fig. 19, the contribution of $H\alpha$ to continuum in the [S II] NB filter is varying from $\sim 1/2$ down to $\sim 1/5$.

For ESO 374-G25 the $H\alpha$ line is broader than our available NB filters (see Fig. 20). While the 670 nm filter covers about 80% of the total $H\alpha$ line, the [S II] filter will collect only about 45% close to the line center. Hence, the faster (because of the lower distance to the nucleus on Keplerian orbits) variations of the $H\alpha$ line wings will be missed. To get a better estimate on the true line dispersion of $H\alpha$, the stationary narrow components (of the host environment) have been subtracted. This is depicted in Fig. 20, where the narrow $H\alpha$ 6548 Å and the narrow [N II] 6584 Å lines have been subtracted. This was performed in the following order:

1. Fit a Gaussian profile to the [N II] 6584 Å line with the boundary condition that the underlying slope of the broad line towards longer wavelengths has a constant gradient. Then subtract the Gaussian from the spectrum.
2. According to Storey and Zeppen (2000), we assume that the flux ratio between [N II] 6548 Å and 6584 Å is 1:3. Then we subtract a scaled Gaussian with same line width parameters, from the spectrum at 6548 Å.
3. Finally we perform another Gaussian profile fit at the position of $H\alpha$, again with the boundary condition that the underlying spectral slope has a minimized gradient. This profile is subtracted from the spectrum too.

In Figure 20, the resulting spectrum is plotted together with the subtracted peaks (dotted slope). Netzer (1990) suggests a flux ratio between [N II] and $H\alpha_{\text{narrow}}$ of about 1:1 (up to 1:3). In our fit, the narrow $H\alpha$ is only 70.25% apart from the 1:1 ratio. Hence, we may have overestimated [N II] and/or underestimated the narrow $H\alpha$. Fixing either problem however, would create a very unlikely narrow gap in the BLR profile, which is more speculative than the smoothness assumption in the profile fits above. From Fig. 20 the Fe II contribution could not be clearly determined, because a potential bump in the spectral slope is not seen here. By assuming a smooth BLR profile the potential contribution is negligible.

For comparison, we calculate the dispersion for the different NB filters used, i.e. [S II] of VYSOS 6 and 670 nm of VYSOS 16. In Fig. 20, we convolved the $H\alpha$ line profile (above the dashed continuum) with the used filter transmission normalized to its maximum transmission. While spectroscopic reverberation data enable one to use the velocity information from the rms spectra, i.e. from the variable portion of the emission lines, several attempts have been made to determine the mas of the central black hole using single epoch spectra (e.g. Vestergaard 2002, Woo et al. 2007, Denney et al. 2009). In this way the reported uncertainties of the velocity dispersion range between 15% and 25%, of which we will assume the latter. The total $H\alpha$ dispersion is then (2190 ± 550) km/s.

Figure 21 illustrates which regions in a Keplerian accretion disk are lost, when observing with the NB filter respectively. The Figure approximates our situation of 15 – 20% line flux loss. Here, we only lose the BLR clouds moving fast on the line-of-sight to the observer. The fast moving clouds that move perpendicular to the line-of-sight, will still be measured in the narrow filter. However, the average BLR distance measured must then be expected to be larger.

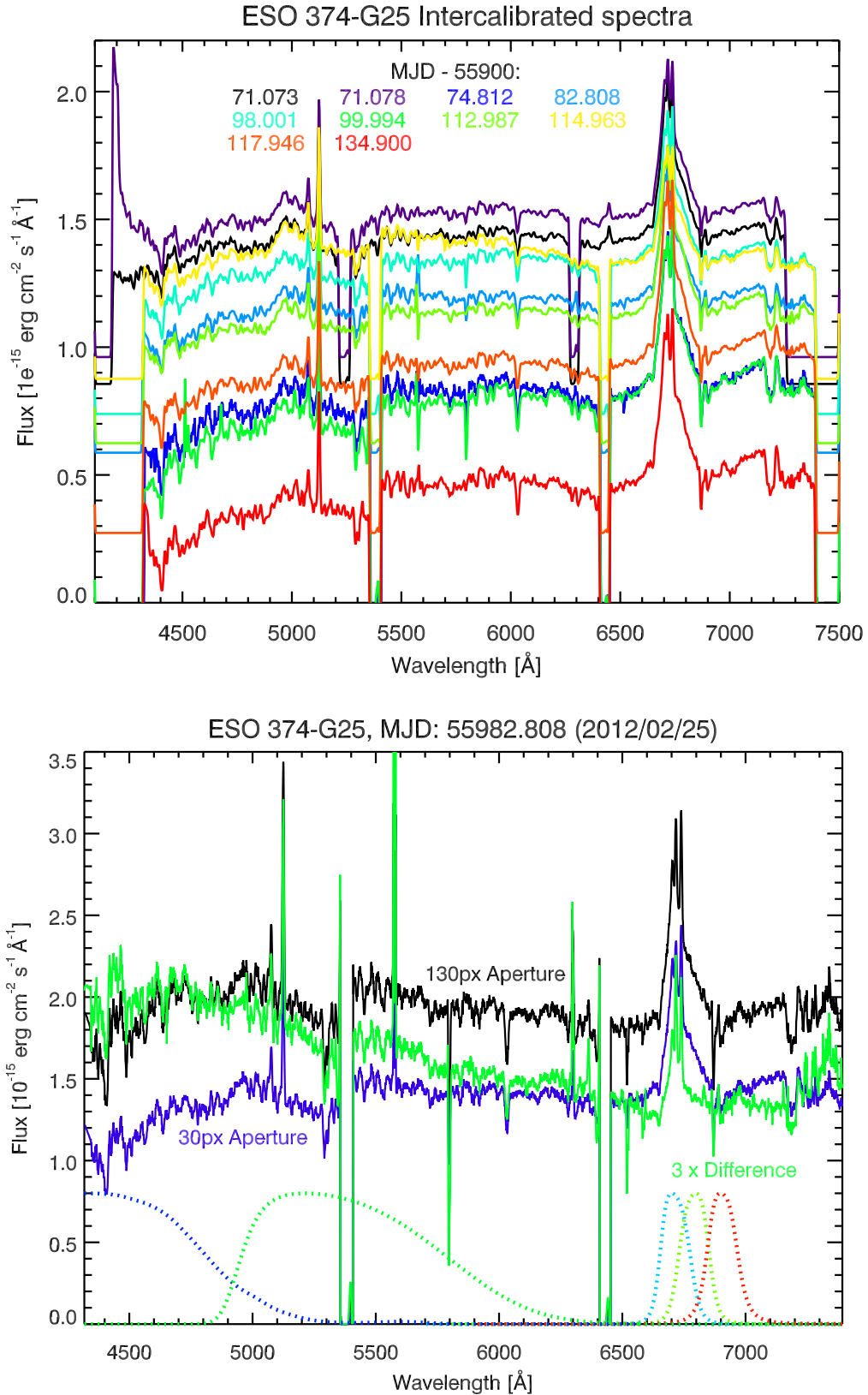


Figure 19: SALT spectra of ESO 374-G25. The upper plot shows our complete set of intercalibrated spectra. The plot below shows a difference spectrum between a $7''.1$ (30 pixel) wide aperture and $30''.7$ (130 pixel) wide aperture. As additional information, relative filter transmissions *VYSOS 16* are drawn at the lower border (left to right): B_J , V_J , 670, 680 and 690 nm. At about 5400 \AA and 6400 \AA , the CCDs have their borders.

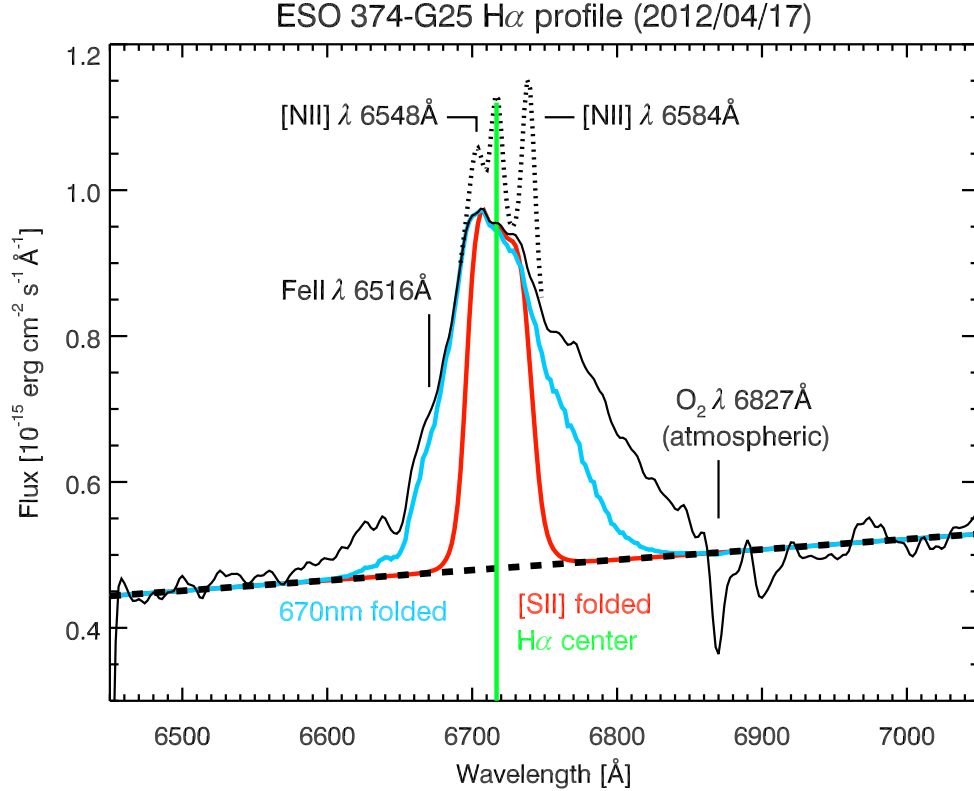


Figure 20: SALT spectrum of ESO 374-G25 from 4th April 2012, zoomed in to the region of the broad H α line (black line). Narrow components of H α and [N II] have already been subtracted, and are represented by the thin dotted line. The convolutions of the narrow band filters with the broad H α line profile are plotted as colored lines. For this, the line profile has been measured above the dashed continuum approximation and multiplied with the relative transmission of the filter and quantum efficiency of the CCD. The 670 nm filter (cyan) covers about 80% of the total line, while the [SII] filter (red) will collect only about 45%, and predominantly the slow moving components. At 6867 Å, there are atmospheric O₂ absorption features, that have been avoided in the continuum estimation. A very weak narrow component is visible at the redshifted position of H α . 25 Å to the right side of it, we find the narrow [N II] ($\lambda = 6584$ Å) line. Both are covered by our narrow filters, but they stay constant over time.

The details of these effects are being studied in the Diploma Thesis by Bruckmann (2012). The first results show that the bias of using a filter that is narrower than the target Balmer (H β in his case) line will not change the average lagtime significantly. This is numerically simulated for a 3C120-like object with the results:

1. A perfect symmetrical cut of the high-velocity line wings of 50% will only introduce a systematic error of $\sim 2\%$ to τ .
2. Moving the filter to the red flank, losing $1/3$ of the total flux at the blue side (asymmetric cut) will cause a systematic offset of $< 1\%$ only.

In our particular case, we are facing a combination of both effects. Even given the perspective of the model analysis above, we must consider that there may be a bias in

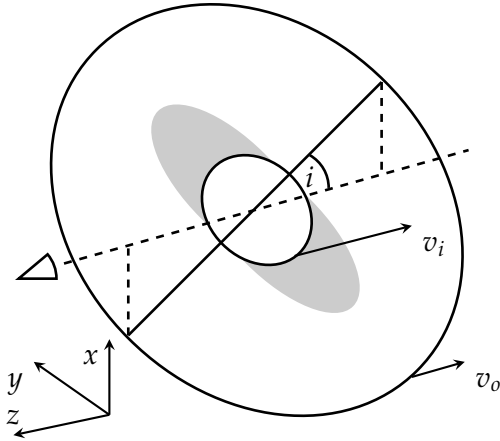


Figure 21: Schematic view by an observer of an about i inclined BLR disk with inner and outer radius (black ellipses). The use of a very narrow filter blends out the high velocity clouds (shaded region). Inclination is chosen high, radii and distance are not to scale. v_i and v_o represent the fast inner or slower outer velocity components.

our time lag estimates (see Sect. 3.5.1) towards larger values besides other sources of errors, like time-sampling and time-gaps that will have an impact on our results.

3.5 RESULTS AND DISCUSSION

In this Section we present our results of the different analysis steps, beginning with the time-lag estimation through DCF (Edelson and Krolik 1988) applied to the lightcurves. Then we combine this with single epoch spectroscopy to estimate black hole masses. Using the FVG method (Choloniewski 1981; Winkler 1997; Winkler et al. 1992), we separate nuclear from host flux in our apertures. Finally, we present new positions of our four observed AGN in the radius – luminosity diagram.

3.5.1 Lightcurves and BLR size

In this Subsection, we will present the different lightcurves and their DCF together with a statistical analysis to estimate reliable lagtime errors.

PG0003

Figure 22 depicts the light curves of PG0003+199. The AGN continuum as traced by the B band increases gradually from August 2009 to a peak around the end of September, followed by a steep trough by 20% at MJD ~ 55118 ($= 55045 + 73$). Also the $H\alpha$ light curve has a steep $\sim 10\%$ trough with a delay of about 20 days.

We used the discrete correlation function (DCF, Edelson and Krolik 1988) to cross correlate the $H\alpha$ and B band light curves. The cross correlation shows a major peak with a lag of 20.2 days as defined by the centroid τ_{cent} (Fig. 23). Two smaller correlation peaks around lag 50 days and 65 days are present, and are caused by the B band troughs at the beginning and middle of September 2009 (Fig. 22). We do not consider these two lags further here, because spectroscopic reverberation predicts a lag of less than 30 days (Peterson et al. 2004).

We estimate the error for the cross correlation time lag using the flux randomization / random subset selection method (FR/RSS, Peterson et al. 1998b, Peterson et al. 2004). From the observed light curves of $H\alpha$ and B band, a subset of 2000 randomly generated curves is created with each curve containing 63% of the original data. This

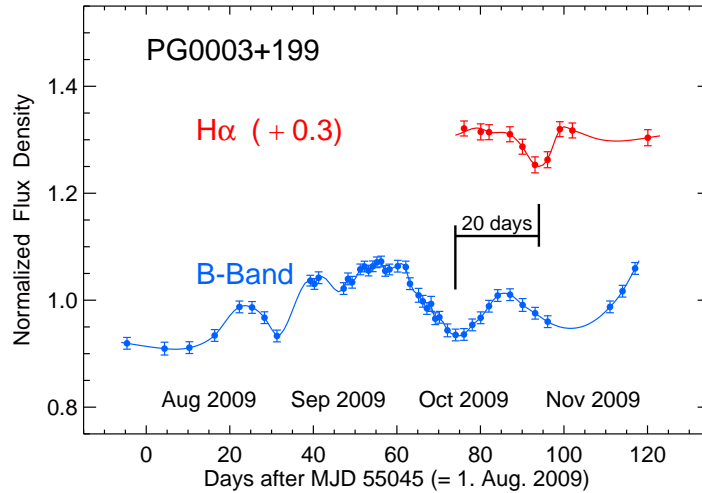


Figure 22: B band and $H\alpha$ light curves of PG0003+199. The $H\alpha$ observations were started in October 2009 after recognizing the pronounced B band variations.

is considering the Poisson probability, avoiding the selection of a particular point, reducing the size of the selected sample by a factor about $1/e$ (Peterson et al. 2004). For every datapoint the flux is then altered according to its normal distributed measurement error. For each of these 2000 sets of lightcurves we calculate the DCF and its centroid value τ_{cent} . Figure 24 shows the distribution of the 2000 τ_{cent} values, which yields the median lag τ_{cent} and the 68% confidence range. From this distribution we obtain a lag $\tau_{cent} = 20.5^{+2.0}_{-2.8}$ days. Thus, the mean of positive and negative uncertainty of τ_{cent} is about 12% ($2.4/20.5$).⁶ Correcting for the time dilation yields a rest frame lag of $\tau_{rest} = 20.0^{+2.0}_{-2.7}$ days.

We did not find any $H\alpha$ lags of PG0003+199 in the literature, but we can compare our result with that of the $H\beta$ line for which spectroscopic reverberation mapping found a rest-frame lag of 15.7 ± 3.7 days averaged over several epochs (Peterson et al. 2004, Bentz et al. 2009b) or the recent study by Grier et al. 2012b, with a lag of 13.9 ± 0.9 days. This $H\beta$ lag is $\sim 30\%$ smaller than our $H\alpha$ lag of 20.0 days. One possible explanation could be that the BLR size is smaller for higher excitation emission lines. Kaspi et al. (2000) found in the spectroscopic reverberation data of 17 PG quasars $R_{H\alpha} = s \cdot R_{H\beta}$ with a scaling factor $s = 1.19$, but a high uncertainty of ± 0.23 . On the other hand, Kollatschny (2003a) provides clear evidence for the BLR stratification of Mrk 110 ($s = 1.37$, his Table 1). Recently, the Lick AGN Monitoring Program of 11 low-luminosity AGN found $s = 1.54 \pm 0.4$ (Bentz et al. 2010). It could be that the BLR stratification and the scaling factor s depends on the luminosity. The luminosity of PG0003+199 is similar to that of Mrk 110. If the value $s = 1.37$ of Mrk 110 holds for PG0003+199, then the $H\beta$ lag of PG0003+199 translates to an $H\alpha$ lag of $13.9 \times 1.37 = 19.0$ days, hence agrees within 6% with the restframe $H\alpha$ lag of 20.0 days from our measurement. Kaspi et al. (2000) provides us also with an 5100 \AA flux of $(7.57 \pm 1.01) \text{ erg s}^{-1} \text{ cm}^{-2} \text{ \AA}^{-1}$ that corresponds to $(6.56 \pm 0.88) \text{ mJy}$, being in the range

⁶ The observed $H\alpha$ light curve has only 10 data points, 3 of which are in the trough. While a subset of exactly 63% data points would require to take 6.3 data points, we selected 7 random data points. This $\sim 10\%$ larger number of data points may bias the errors to somewhat lower values. On the other hand, we find the largest errors for those randomly selected subset light curves where all 3 data points in the trough are omitted. In this case the information about the existence of a trough is completely lost. To counterbalance this effect, we selected 7 instead of 6.3 data points.

between our measured fluxes, as listed in Table 1 in the Appendix. If one interpolates between our B and V fluxes, (assuming $F_\nu \propto \nu^\alpha$) their total flux is about 10% lower. This can be an explanation for a smaller BLR size one year after our campaign.

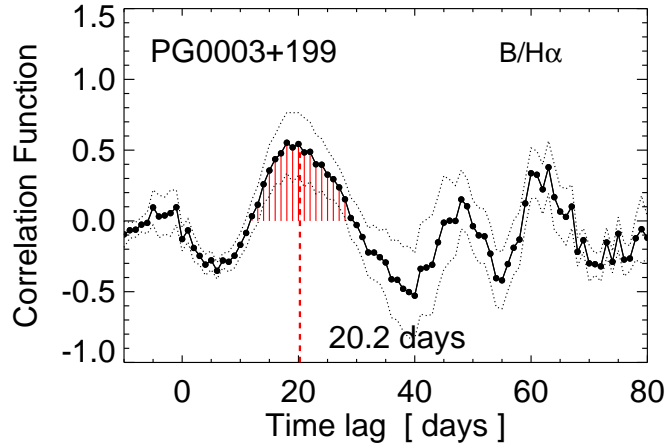


Figure 23: Cross correlation of the B and $H\alpha$ light curves of PG0003+199, taking all data points. The dotted lines indicate the error range ($\pm 1\sigma$) around the cross correlation. The red shaded area marks the range to calculate the centroid τ_{cent} of the major correlation feature, yielding a lag of 20.2 days (vertical dashed line).

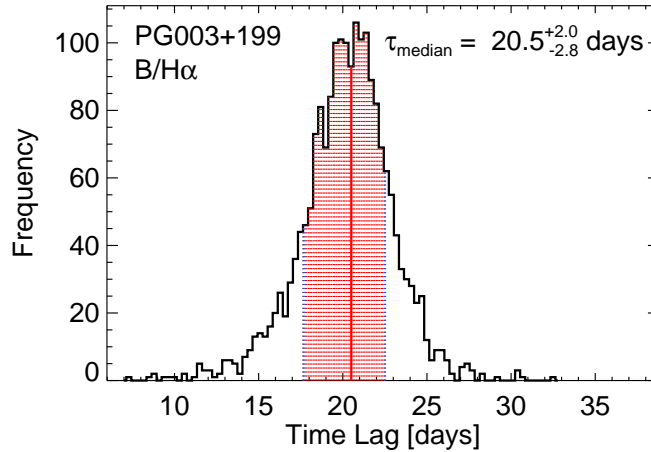


Figure 24: Result of the FR/RSS error analysis of the cross correlation of the B and $H\alpha$ light curves of PG0003+199. The histogram shows the distribution of τ_{cent} for 2000 flux randomized and randomly selected subset light curves. The median of this distribution is taken as the final value of the lag τ_{cent} . The red shaded area marks the 68% confidence range used to calculate the errors of τ_{cent} .

Ark120

Figure 25 depicts the light curves of Ark 120. The dense time sampling clearly outlines the variations. The B band steeply increases during ten days in November 2009 by about 17% with a sharp peak at the end of November 2009. From January to March

2010 it declines gradually by about 17%. In November the V and NB light curves are similar to that of the B band, but with smaller amplitude ($V \sim 10\%$, $NB \sim 7\%$). In contrast to the steep B band flux increase, the NB flux increase is stretched until January 2010 with an amplitude of 12 – 15% between the beginning of November and January. While the continuum brightening occurred in November, the line brightening, as far as we can see it, is delayed to January 2010, yielding the measured lag of $\tau_{cent} \sim 48\text{days}$.

The NB contains about 50% continuum and 50% $H\beta$, as can be already seen in the SE spectrum in Fig. 16. In support of this, the observed flux ratios between the V band and the [O III] band are shown in Fig. 26. Of course, the $H\beta$ reaction to a variation of the continuum is delayed (causing the scatter seen in the distribution), but the average fluxes (marked by the colored lines in Fig. 26) allow us to estimate the $H\beta$ fraction in the NB filter. The contribution of $H\beta$ in the broad V band is clearly $< 10\%$ (see Fig. 16), hence a subtraction of the V band flux from the [O III] NB flux will result in a slightly underestimated $H\beta$ residual flux, which is $\sim 55\%$ of the NB flux in this case. With regard to the scattering, the assumption of $\sim 50\%$ continuum can therefore be justified. The residual error will finally be eliminated in our following DCF analysis, where this assumption suppresses the autocorrelation component.

To remove the continuum, we computed a synthetic $H\beta$ light curve by subtracting a scaled V curve from the NB curve: $H\beta = NB - 0.5 V$ (V scaling factor = 0.5). Alternating the V scaling factors between 0.4 and 0.6 yields similar results. The synthetic $H\beta$ curve still has a remaining variability pattern in October and November, which we suggest arises from the relics of the continuum. However, the important result is that compared to November, the $\sim 10\%$ higher flux level in January becomes more

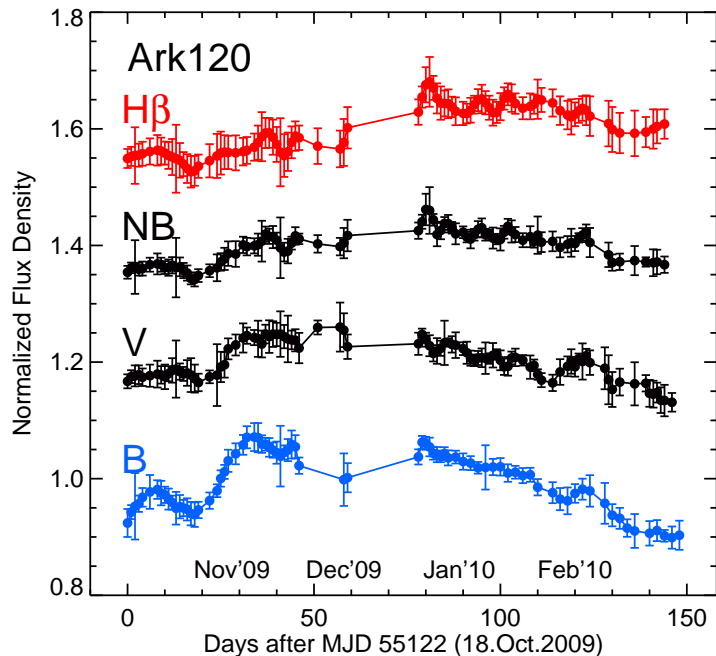


Figure 25: Light curves of Ark120 between October 2009 and March 2010. The B , V , and NB curves are as observed, the $H\beta$ curve is computed by subtracting a scaled V curve from the NB curve ($H\beta = NB - 0.5V$) and re-normalization (mean=1). For better visibility, the light curves are shifted against each other by +0.2. The 2009 December data are mostly lost by strong wind preventing us from opening the dome.

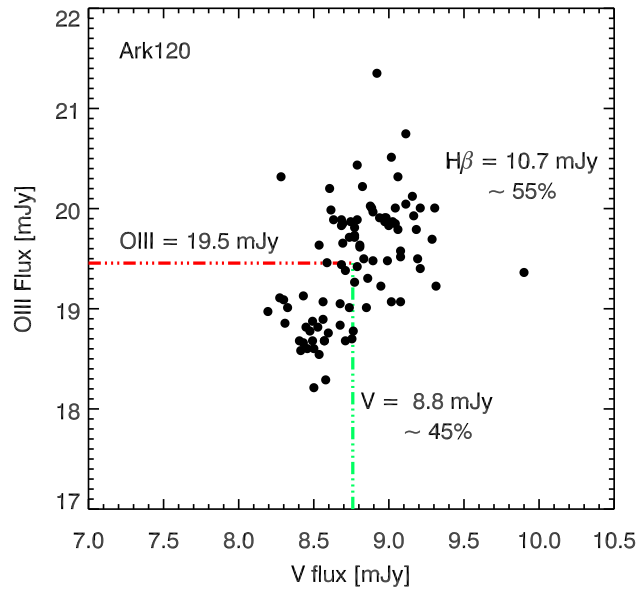


Figure 26: Flux-flux diagram of Ark120 for the [OIII] and V band filter. The red and green lines represent the average flux in the [OIII] and V band respectively. The data are as observed and not corrected for extinction. Fluxes (black dots) were measured using 7.5 aperture photometry.

pronounced. While the subtraction of a scaled V curve from the NB curve turns out to be a successful approach to recovering a pure $H\beta$ light curve, it may be more precise to take just another NB filter in direct neighborhood of the $H\beta$ line, placed on a line-free continuum area. Note that to achieve this, the VYSOS 16 has been equipped with a set of three neighboring NB filters.

Figure 27 shows the cross correlation results after applying the DCF to the entire light curves in a first step. The DCF of B and NB exhibits two distinct major peaks, one at a lag of 47.5 days and one at a lag of about zero days. Because the cross correlation of B and V yields a lag of $1.2^{+1.6}_{-2.6}$ days consistent with lag zero, we conclude that the lag zero peak in the DCF of B and NB comes from the continuum contribution contained in the NB. This contribution appears here in autocorrelation, while the lag of 47.5 days is due to the line echo. This is corroborated further by the DCF of the B and synthetic $H\beta$ curves, where the peak at lag 47.7 days dominates, while the continuum-caused contribution at lag zero is very reduced. This shows that the subtraction of a scaled V light curve from the narrow band light curve, in fact, largely removes the interfering continuum emission, allowing us to measure the lag of the emission line.

To determine the lag uncertainties, we applied the FR/RSS method, again creating 2000 randomly selected subset light curves, each containing 63% of the original data points, and randomly altering the flux value of each data point consistent with its (normal-distributed) measurement error. Then we cross-correlated the 2000 pairs of subset light curves and computed the centroid τ_{cent} . As shown in Fig. 28, the resulting median lag is $\tau_{cent} = 47.5^{+3.4}_{-3.0}$ days for the DCF of B and NB, and $\tau_{cent} = 48.0^{+3.0}_{-3.3}$ days for the DCF of B and synthetic $H\beta$. Briefly, the lag uncertainty is about 7%. Correcting 48.0 days for the time dilation factor (1.0327) we obtain a rest frame lag of $\tau_{rest} = (46.5 \pm 3.3)$ days, consistent with the lag found by spectroscopic monitoring ((47 ± 10) days

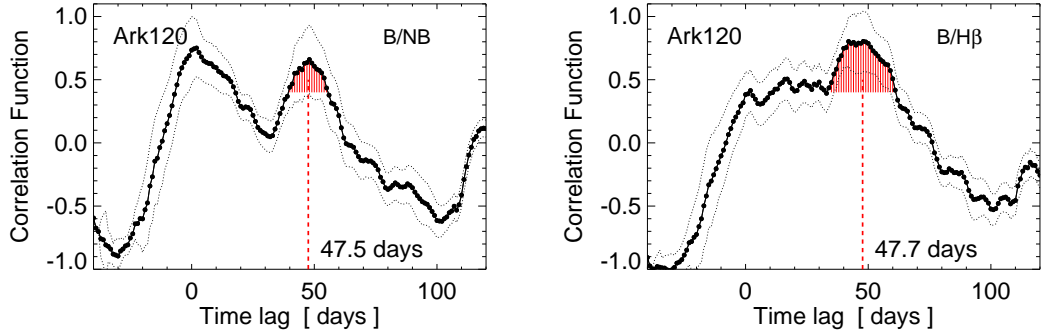


Figure 27: Cross correlations of Ark 120 light curves for B and NB , and for B and the synthetic $H\beta$ ($= NB - 0.5V$). The dotted lines indicate the error range ($\pm 1\sigma$) around the cross correlation. The red shaded area marks the range used to calculate the lag τ_{cent} (vertical dashed line).

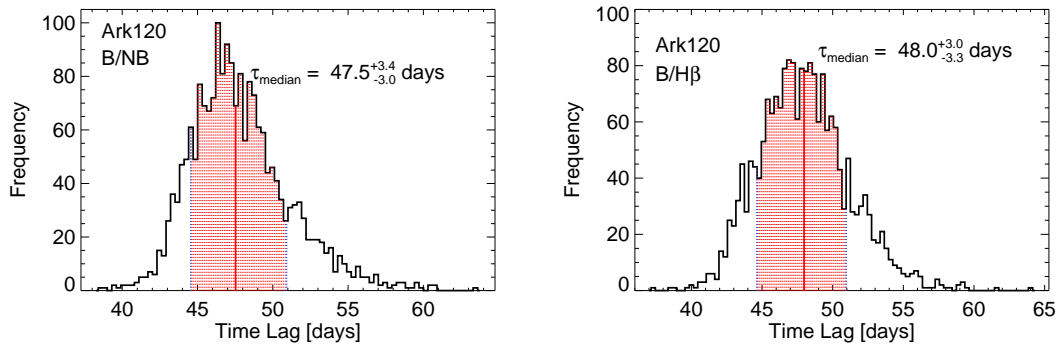


Figure 28: FR/RSS cross correlation results of Ark 120. Left: B and NB . Right: B and synthetic $H\beta$. Each histogram shows the distribution of τ_{cent} obtained by cross-correlating 2000 flux randomized and randomly selected subset light curves. The median of this distribution is taken as lag τ_{cent} . The red shaded area marks the 68% confidence range used to calculate the errors of τ_{cent} .

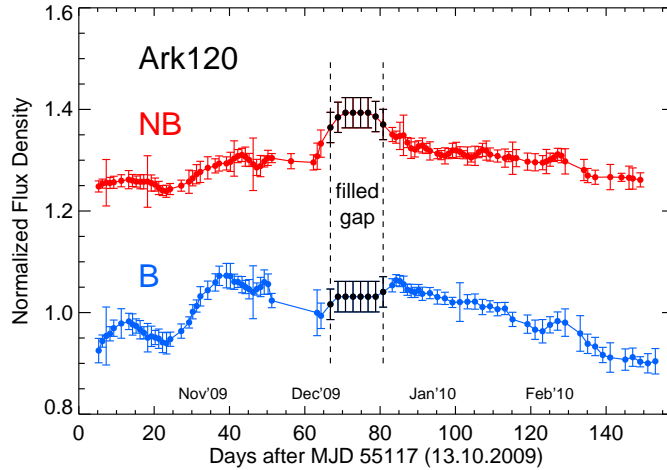


Figure 29: Artificial B and NB light curves of Ark120, with additional data points (black dots) filling the observational gap of 18 days end of December 2009. The data points are chosen so that they mimic a strong line echo during the gap.

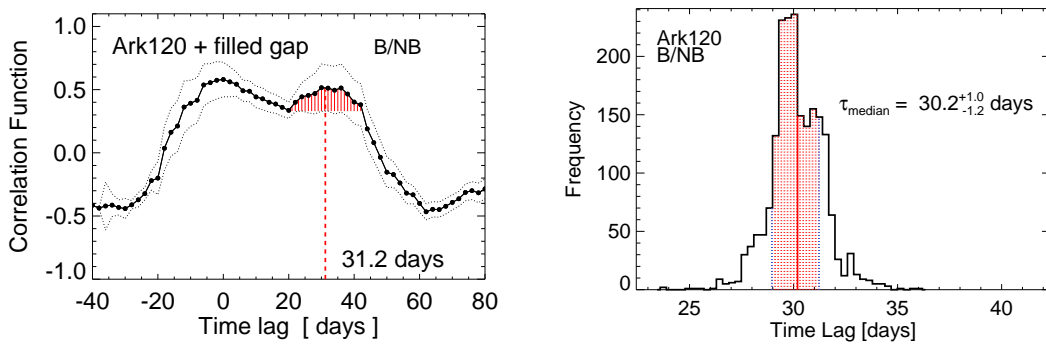


Figure 30: *Left*: Cross correlation of the complemented B and NB light curves of Ark 120 shown in Fig. 29. The dotted lines indicate the error range ($\pm 1\sigma$) around the cross correlation. *Right*: Distribution and 68% confidence range of τ_{cent} , obtained by FR/RSS analysis.

by Peterson et al. (1998a, 2004) and in the range of 34 – 54 days by Doroshenko et al. (1999)).

However, because of the observational gap at the end of December 2009, we do not know whether the line brightening already occurred at this time. To test the effect, if there were a strong line echo in December 2009, we took the B and NB light curves and filled the gap with the artificial bump in the NB light curve as shown in Fig. 29. The bump may be somewhat strong, but it was chosen to better illustrate the potential effects here. One can already see in the light curves that the lag between the B band increase in November and the NB increase in December is about 30 days. The cross correlation of these artificial light curves shows two major peaks, one from the autocorrelated continuum at lag zero and one from the line at lag 31 days (Fig. 30). The FR/RSS analysis yields $\tau_{cent} = 30.2^{+1.0}_{-1.2}$ days. The difference between this lag and $\tau_{cent} = 48$ days derived from the original light curves is 18 days which is just about the size of the gap. From this example we conclude that, if there is a large observational

gap, one should take a potential systematic error of τ_{cent} into account, which is about the size of the gap. In this example the light curve is short in the sense that it covers only one pronounced continuum event and one subsequent line echo. Therefore the missing information during the gap cannot be filled. But in long-lasting light curves that cover several variability events one may expect that the actual gaps are smaller on average. These considerations about systematic errors hold for both photometric and spectroscopic reverberation data. Therefore, they do not question the successful applicability of photometric reverberation mapping.

3C120

The light curves of 3C120 are shown in Figure 31. The B band shows a gradual increase from the beginning of October to the beginning of December by 30%. Afterwards, the flux undergoes an abrupt drop by about 20% until mid-December 2009. Between the end of January and early February, the variability is more regular and the flux increases again to reach a third maximum at the end of February 2010. In contrast to the steep B band flux increase, the NB flux increase is stretched until December 2009 to its first maximum. The sharp decrease in flux in the B band, after the second peak in late December 2009, is reflected in the NB in early January 2010. Thus, as a first approximation, the time delay is 20 – 30 days. The spectrum, shown in Fig. 17 allows us to estimate the $H\beta$ fraction to the [O III] NB filter to be $\sim 50\%$. Additionally, by plotting the V band flux versus [O III] NB flux in Fig. 32, we estimate this ratio. Subtracting the V band from the NB yields an average $H\beta$ fraction of 44%. Considering

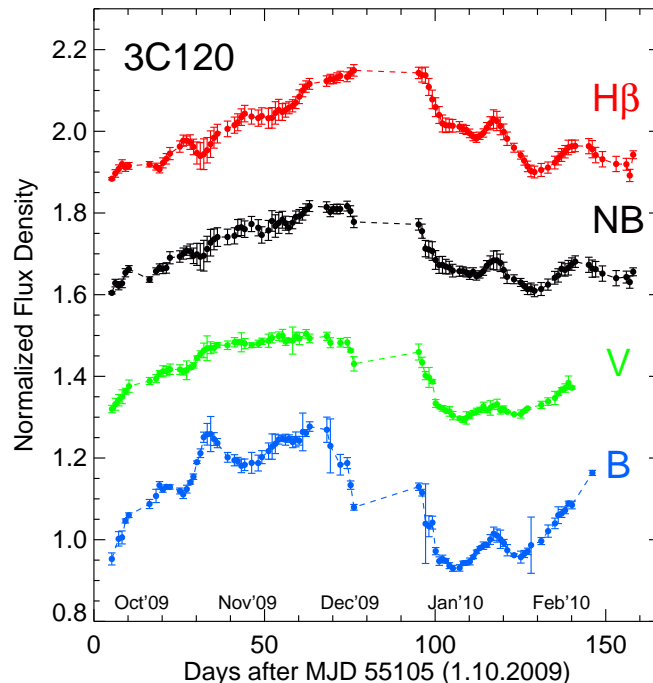


Figure 31: Observed light curves of 3C120 between Oct. 2009 and March 2010. The $H\beta$ light curve is computed by subtracting a scaled V curve from the NB curve and re-normalized to mean = 1. The light curves were shifted by multiples of 0.2 for clarity. The data gap between the end of December 2009 and the beginning of January 2010 is mostly due to strong wind preventing observations.

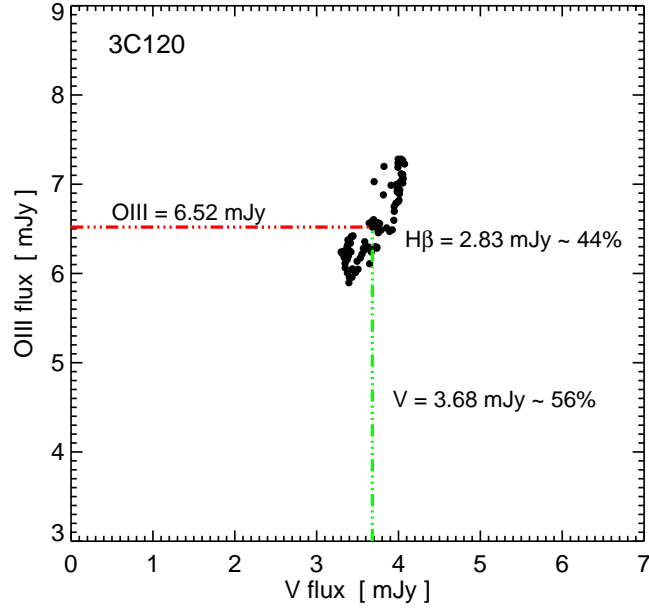


Figure 32: Flux-flux diagram of 3C120 for the [O III] and V band filter. The red and green lines represent the average flux in the [O III] and V band respectively. The data are as observed and not corrected for extinction. Fluxes (black dots) were measured using $7''.5$ aperture photometry.

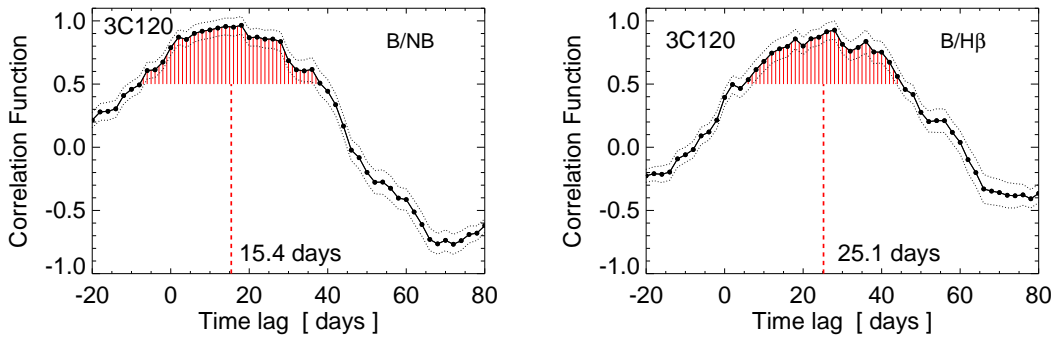


Figure 33: Results of the cross correlations of the lightcurves of 3C120. Left: B and [O III] NB. Right: B and synthetic $H\beta$ light curves. The dotted lines indicate the error range ($\pm 1\sigma$) around the cross correlation. The red area marks the range used to calculate the centroid of the lag, which is represented by the vertical red dashed line.

that the V band contains the $H\beta$ flux too ($< 10\%$), this ratio is slightly underestimated. Hence, the assumption of $\sim 50\%$ continuum is justified.

The cross correlation shows a major peak for a time delay of 25.1 days, which is defined by the centroid τ_{cent} in Figure 33. As usual we adopted the median sampling value (2 days) for the bin size in the DCF. In addition we have made the computations for different values of the bin size, in order to detect possible significant variations in the time delay (Rodríguez-Pascual et al. 1989). Some of this variations can be introduced due to scatter of the points in the DCF (bin size smaller than the median sampling) or due significant structures caused by the noise (bin size greater than the

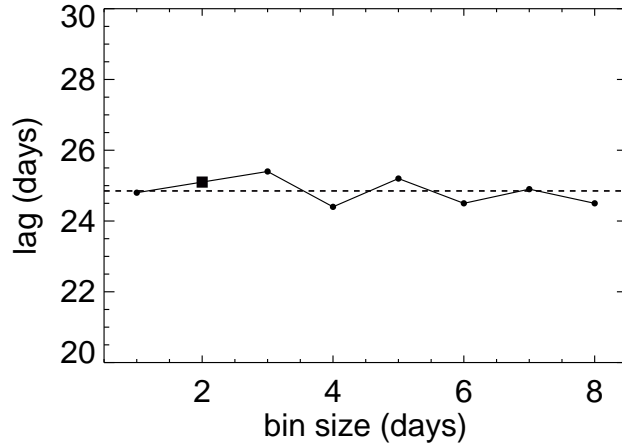


Figure 34: Dependence of the lag (determined by the DCF) from the bin size. The square symbol indicates the value used in this work (bin size of 2 days) and the dashed line represents the average value of 24.85. The data points are here connected by a line only to guide the eye.

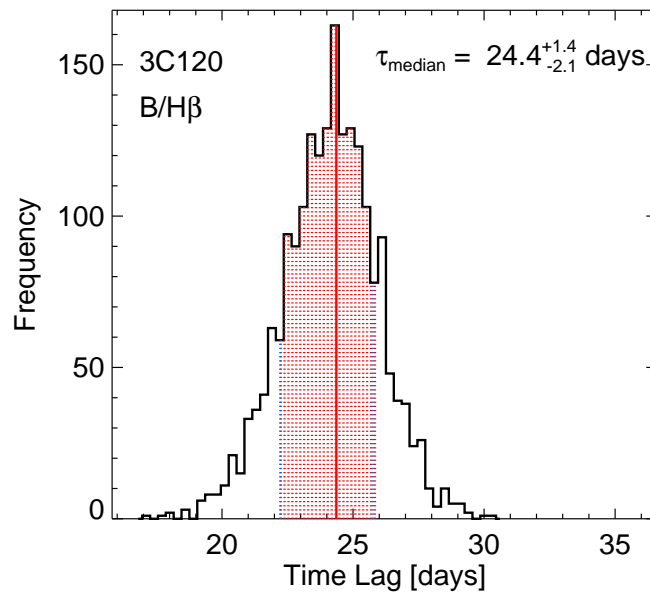


Figure 35: Results of the FR/RSS cross correlation for 3C120 for B and synthetic $H\beta$. The histogram shows the distribution of the centroid lag obtained by cross correlating 2000 flux randomized and randomly selected subset light curves. The red area marks the 68% confidence range used to calculate the errors of the centroid.

median sampling) (see Rodriguez-Pascual et al. 1989, for details). Figure 34 shows the dependence of time delay on different bin size values (1-8 days). The difference is less than 2% in comparison with our adopted value and which is an expected response for high quality sampling.

Because of the broad distribution of the lag, the DCF centroid was adopted to be measured above the correlation level at $r \geq 0.5 \times r_{max}$. We also used the correlation level at $r \geq 0.8 \times r_{max}$, which is the most adopted value in recent spectroscopic reverberation measurements. To determine the uncertainty in the time delay we apply again the FR/RSS method (Peterson et al. 1998b, Peterson et al. 2004)). Figure 35 shows a histogram with the distribution of the 2000 τ_{cent} values which yields a median lag $\tau_{cent} = 24.4_{-2.1}^{+1.4}$ days. Correcting the mean lag time for the time dilation factor we obtain a rest frame lag $\tau_{rest} = (23.6 \pm 1.7)$ days, hence the lag uncertainty less than 10%. This lag is smaller than the $\tau_{rest} = (27 \pm 1)$ days obtained by Grier et al. (2012a), from their spectroscopic reverberation campaign that was one year after ours. Considering the luminosity change during this time, in Sect. 3.5.4 we will see that our results fit nicely to the $R_{BLR} - L_{AGN}$ relationship.

The rest frame lag derived here is in good agreement with the results obtained by Grier et al. (2012a), who determined a rest frame lag $\tau_{rest} = 27 \pm 1$ days from a recent spectroscopic reverberation mapping campaign.

ESO 374-G25

The VYSOS 16 observations were first performed on April 2nd 2012, overlapping with those of VYSOS 6, having the same intended sampling rate of one day, including now also V band observations and switching from the NB [S II] filter of VYSOS 6 to the 670 nm filter of VYSOS 16. To combine both datasets, we normalized the relative VYSOS 16 fluxes to those final datapoints of VYSOS 6, from 2nd until 7th of April (overlapping period).

In the epoch of 2011 (Fig. 36, top left), we see a steep B band rise in April, followed by a decline until May. Afterwards, there is a slow rise towards the end of the epoch. The maximum amplitude of the variation is about 20%. The NB follows the B band qualitatively, but in the minima of the curves in May, we can already see a shift of about 10 days. From the spectra (see 3.4.4), we can assume $\sim 50\%$ contribution of the continuum to the NB fluxes. With this assumption, we can construct a synthetic $H\alpha$ lightcurve by subtracting half of the B band flux (Fig.36, top right). As a result, the minimum in the $H\alpha$ curve is more pronounced.

For the epoch of 2012, we follow an identical analysis. In March, there is a significant valley in the B band (about 10%) of which we see an echo about 10 days later in the NB. Again, by subtracting 50% B band flux, our synthetic $H\alpha$ curve shows a more pronounced echo of this signal. At the begin of April, there is a second bump of about 10%, of which the echo is falling into place with another rise of the continuum in the mid of April, but due to the gap before and the end of the lightcurve afterwards, this is not as clear-cut as the first feature.

Figure 37 shows the results of the DCF analysis of the lightcurves from Fig. 36. The left-hand side represents the DCF between B band and the original NB flux for both epochs. We see autocorrelation peaks at zero days, as expected due to the continuum contribution in the NB filter. However, there are already convincing correlation peaks at $\tau = 11.1$ days (2011) and $\tau = 10.7$ days (2012), by measuring the first moment of the correlations in this peak above a threshold of 0.8 (2011) and 0.3 (2012), as marked

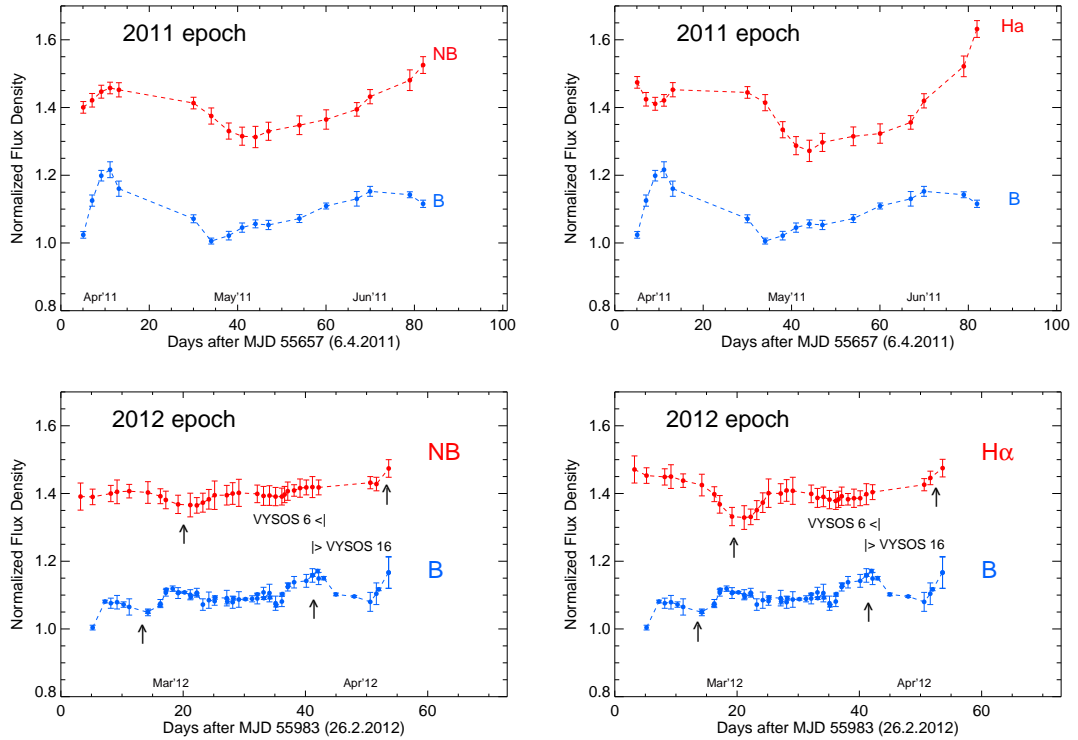


Figure 36: Relative photometric lightcurves of ESO 374-G25. Top left is the original narrow band flux together with the B band taken in 2011. Top right is the B band and the synthetic $H\alpha$ curve, obtained by subtracting a scaled B band curve from the narrow [S II] band for 2011. Below the same figures for the year 2012. All relative fluxes are scaled relative to the first point, chosen to be 1. The NB and $H\alpha$ flux is then shifted 0.4 unit upwards. The ending of the VYSOS 6 observations and the beginning of the VYSOS 16 observations is marked, together with significant features of the lightcurves.

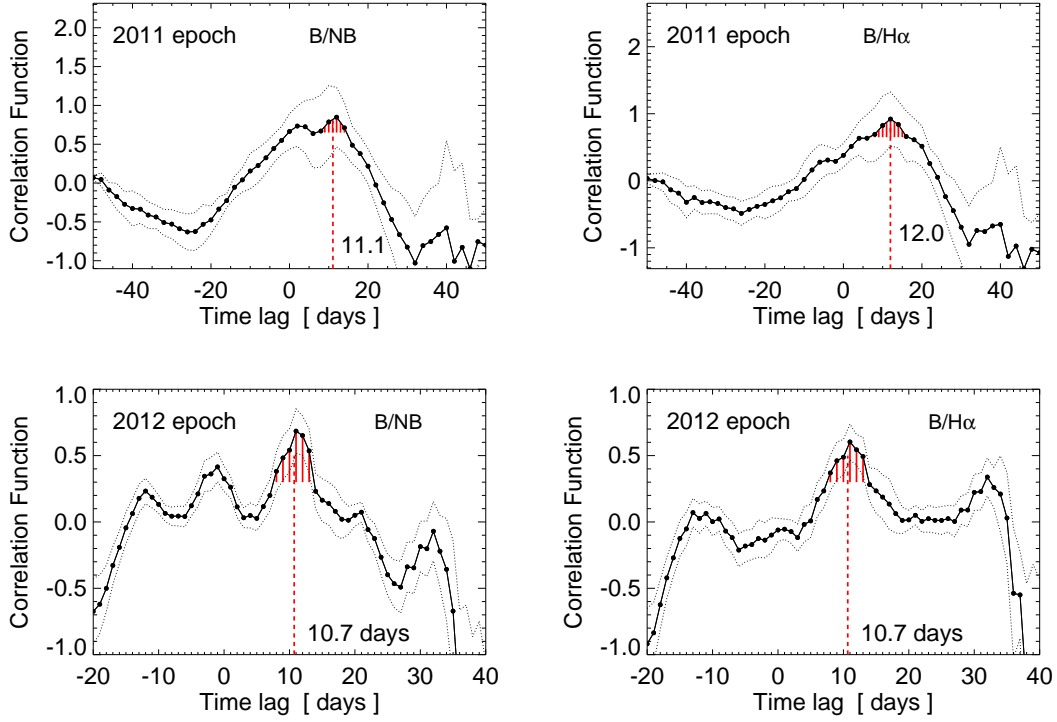


Figure 37: Discrete cross correlation of both observation epochs of ESO 374-G25 applied to the lightcurves in Fig. 36. Left are the DCFs between the observed NB and B band lightcurves, right the DCF between the synthetic $H\beta$ and B band lightcurves. Our assumption for the continuum fraction in the total NB flux appears effective in leveling the autocorrelation peak at zero days.

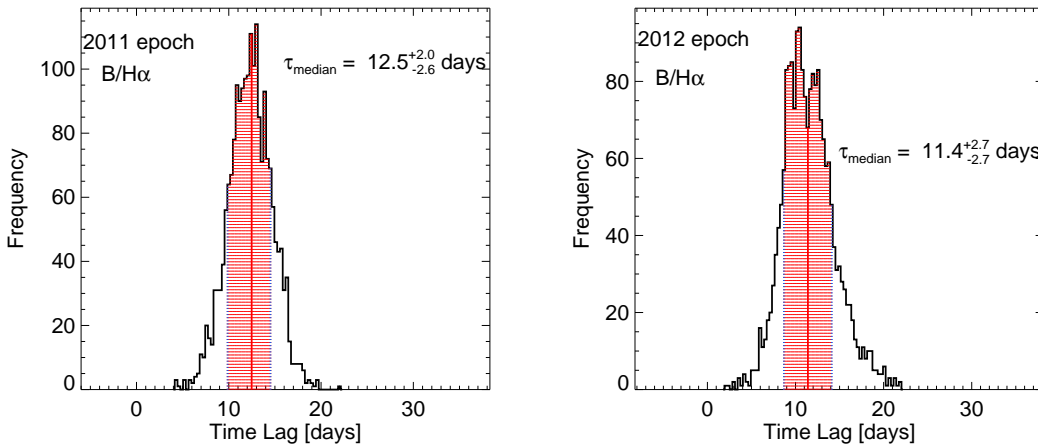


Figure 38: Histogram result of the FR/RSS error analysis of our B and synthetic $H\alpha$ lightcurves for ESO 374-G25. The histogram shows the distribution of τ_{cent} for 2000 flux randomized and randomly selected subset light curves. The median of this distribution is taken as the final value of the lag τ_{cent} . The red shaded area marks the 68% confidence range used to calculate the errors of τ_{cent} .

by the red dashed area in the plots. Note that the correlation coefficient of the DCF is not normalized, so we select the thresholds relative to the peak of the most plausible correlation. The choice of a lower time-bin size does not change the results if a well-sampled data is used according to Peterson et al. (2004). Due to the sparser sampling in 2011, the correlation peaks are broader and the flanks of zero and 11.1 days obviously overlap, biasing the peak of our H α echo towards lower lagtimes. Indeed, this can be verified if we look at the correlation of B band and H α (NB minus 50% of the B band flux). This is shown the right-hand side, where we can clearly see that the autocorrelation peak is well removed in both epochs, 2011 (top right) and 2012 (bottom right). Removing the autocorrelation bias in 2011 pushes the mean lagtime to $\tau = 12.0$ days. In 2012, there is no effect on the result. This is because of the better time sampling of the lightcurve, causing independent sharp correlation peaks in the DCF plot.

To determine the lag uncertainty again, we applied the FR/RSS method. For each of the 2000 generated sets of lightcurves we calculate the DCF and its centroid (like in Fig. 37). Then, in Fig. 38, we show a histogram of the distribution of all the τ_{cent} results. Correcting for time dilation, for the epoch in 2011, we calculate $\tau = 12.2^{+2.0}_{-2.5}$ days by deviating from the median value τ_{median} to each side of the distribution until 68% of the counts are reached, to take this ranges as upper and lower error. Analogously, the result for 2012 is $\tau = 11.1 \pm 2.6$ days.

3.5.2 BH-Masses

Next we try to determine the mass enclosed by the BLR. This mass is dominated by the central black hole, enabling us to determine good estimates with our reverberation mapping technique. The enclosed mass is obtained via the virial theorem:

$$M_{BH} = f \frac{c\tau\sigma_v^2}{G} \quad (5)$$

Where $c \cdot \tau$ is the average radius of the BLR clouds disk on an Keplerian orbit with the velocity σ_v , here the velocity dispersion of the BLR clouds. The factor f is a scaling factor, dependent on the geometry and kinematics in which the real BLR is different from our simplified model. The average value for this is still under debate. Onken et al. (2004) derived a first empirical average of this factor of $f = 5.5 \pm 1.8$. Although there exist more recent studies like Graham et al. (2011) that conclude a value of $2.8^{+0.7}_{-0.5}$, other RM projects as Bentz et al. (2006, 2007, 2009b); Denney et al. (2006, 2009); Grier et al. (2008); Metzroth et al. (2006); Peterson et al. (2004, 2005); Sergeev et al. (2007) have been adopting the value of $f = 5.5$. Hence, we will do the same for better comparability of our results with the literature.

The bottom line of our analysis is that these virial BH mass estimates have to be seen with some reservation because we only rely on single epoch spectra and the line profiles are not necessarily symmetric, as can be seen easily in the H α lines by Ark120 and ESO 374-G25, both of which show a prominent red wing.

PG0003

For PG0003+199 we obtained an intrinsic H α line dispersion from our single epoch spectrum of 870 km/s (with 25% uncertainty adopted). The DCF analysis of the lightcurve shows a rest frame time time delay of 20.0 ± 2.4 days. Then the virial black hole mass is $M_{virial} = (3.0 \pm 1.5) \times 10^6 M_{\odot}$. Adopting the scaling factor of $f = 5.5$ (Onken et al.

2004), this yields a central black hole mass of $M_{\text{BH}} = 16.3 \pm 8.3 \times 10^6 M_{\odot}$, in agreement with the value of $15.2^{+4.7}_{-4.2} \cdot 10^6 M_{\odot}$ derived via spectroscopic reverberation mapping by Peterson et al. (2004).

Ark120

From our single epoch spectrum we determined an intrinsic $H\beta$ line dispersion of $\sigma = 1950 \text{ km/s}$, in agreement with the value by Peterson et al. (2004). To get rid of the red wing of the $H\beta$ line, we mirrored the blue side of the $H\beta$ line profile to the red, and calculated the line dispersion of this synthetic profile. The shape and the dispersion of this profile are consistent with what we derived for $H\alpha$ ($\sigma \sim 1970 \text{ km/s}$) and $H\gamma$ ($\sigma \sim 1920 \text{ km/s}$). Combining line dispersion (with 25% uncertainty adopted) and the rest frame time delay ($46.5 \pm 3.25 \text{ days}$) yields a virial $M_{\text{virial}} = (35 \pm 17) \times 10^6 M_{\odot}$.

Again using the scaling factor $f = 5.5$, this corresponds to a central black hole mass of $M_{\text{BH}} = 190 \pm 96 \times 10^6 M_{\odot}$, consistent with the value of $195 \pm 44 \times 10^6 M_{\odot}$ derived via spectroscopic reverberation mapping by Peterson et al. (2004).

Already in the 1970s and 1980s, numerous studies revealed that the $H\beta$ line profile of Ark120 is strongly variable and exhibits two peaks in the rms spectra and a prominent red wing, which is present neither in $H\alpha$ nor in $H\gamma$ (Fig. 16). As discussed by Doroshenko et al. (1999), the BLR of Ark120 may show accretion inflows in addition to the virialized motion, and therefore any black hole mass estimates should be considered with some reservation.

3C120

Using the velocity dispersion (with 25% uncertainty adopted, i.e. $\sigma_{\text{line}} = (1264 \pm 316) \text{ km/s}$) and our rest frame time lag $\tau = 23.6 \text{ days}$, the virial black hole mass is $M_{\text{virial}} = (10.4 \pm 5.3) \times 10^6 M_{\odot}$. This is consistent with the result of $M_{\text{virial}} = (10 \pm 5) \times 10^6 M_{\odot}$, derived via spectroscopic reverberation mapping by Peterson et al. (2004) and the more recent value of $M_{\text{virial}} = (12 \pm 1) \times 10^6 M_{\odot}$, as derived by Grier et al. (2012a), also from a spectroscopic monitoring campaign. Our result for the central black hole mass is then $M_{\text{BH}} = (57 \pm 29) \times 10^6 M_{\odot}$.

ESO 374-G25

From the ESO 374-G25 lightcurve, we adopt $\tau = 11.1 \pm 2.6 \text{ days}$ of the epoch in 2012, corresponding to our spectroscopic follow-up observation with the SALT telescope (see section 3.5.1). From the spectra we obtained a $H\alpha$ velocity dispersion of $\sigma_v = (2190 \pm 550) \text{ km/s}$ (Section 3.4.4). This yields a virial black hole mass of $M_{\text{BH}} = (10.4 \pm 5.7) \times 10^6 M_{\odot}$. Assuming the scaling factor $f = 5.5$ the central black hole mass is $M_{\text{BH}} = (57 \pm 32) \times 10^6 M_{\odot}$.

3.5.3 *Host-subtracted AGN luminosity*

To determine the AGN luminosity free of host galaxy contributions, we applied the flux variation gradient (FVG) method proposed by Choloniewski (1981). In this method the B and V data points obtained in the same night through the same apertures are plotted in a B -flux versus V -flux diagram. Fluxes (e.g. in units of mJy) are plotted and not magnitudes. The important feature is that the flux variations follow a linear

relation with a slope Γ_{BV} given by the host-free AGN continuum (e.g. Choloniewski 1981, Winkler et al. 1992 and Winkler 1997).

In the flux-flux diagram the host galaxy – including the contribution of line emission from the NLR – lies on the AGN slope somewhere toward its fainter end. This has been demonstrated for a sample of 11 nearby AGN (containing 3C120 but not ESO 374-G25, PG0003+199 and Ark120) by Sakata et al. (2010), using monitoring data in combination with Hubble Space Telescope and multi band ground-based images from the MAGNUM telescope. For an $8''.3$ aperture, they derived host galaxy colors in the range $0.8 < B - V < 1.1$ (their Table 6), which agree with the typical colors of a bulge or an elliptical galaxy. This color range corresponds to a host slope in the range $0.4 < \Gamma_{BV}^{host} < 0.53$. The contribution of the NLR emission lines to the B and V bands is less than 10% of the host flux and has a similar color as the host galaxy (cf. Tables 6 and 8 of Sakata et al. (2010)). We note that dust enshrouded nuclear starbursts, which often accompany the AGN phenomenon, have red colors ($B - V \sim 1$). They would be unresolved on HST images and could explain the small deviations of the host position from the AGN slope found in three cases by Sakata et al. (2010). Therefore, by host we here denote the host galaxy including NLR AGN lines and starbursts.

The host slopes pass through the origin. Because the host slopes are flatter than typical AGN slopes ($\Gamma_{BV} \sim 1$), the intersection of the two slopes should occur in a well defined range. Winkler et al. (1992) showed for NGC 3783 that this intersection range allows one to determine the host flux contribution and to calculate a host-subtracted AGN luminosity at the time of the monitoring campaign – even without the need for high spatial resolution images. In the following Subsections, we will present our results of the FVG analysis, applied to our lightcurves.

PG0003

During our monitoring campaign of PG0003+199 in August through November 2009, we obtained only B fluxes, but we have three data points at hand for the B versus V flux-flux diagram as shown in Fig. 39. All data are corrected for galactic foreground extinction (Table 1). That PG0003+199 was much brighter in 1979 (McAlary et al. 1983) than in 2009-2011 allows us to achieve a linear least-squares fit to the data points with sufficient accuracy. The fit yields an AGN slope $\Gamma_{BV} = 1.20 \pm 0.04$. This slope is at the steep end, but within the range determined by Winkler et al. (1992) for other type-1 AGN.

To check the slope of PG0003+199 further, we searched in the NASA Extragalactic Database (NED) and found two more B and V data points taken with comparable apertures, one with $15''.7$ by McAlary et al. (1983) and one with $14''.0$ by Elvis et al. (1994). These (extinction corrected) data points are displaced to the right of the $7''.8$ slope in Fig. 39, because they contain additional host emission from the extended disk which is redder than the AGN emission. These two data points yield a slope of $\Gamma_{BV} = 1.25 \pm 0.04$. The consistency of Γ_{BV} derived from two independent data sets corroborates the steep AGN slope of PG0003+199.

The range of host slopes ($0.4 < \Gamma_{BV}^{host} < 0.53$) is taken from Sakata et al. (2010), corresponding to their colors $0.8 < B - V < 1.1$ in their Table 6. The intersection area of the AGN and host slopes defines the host flux. Averaging over the intersection area yields a mean host flux of (2.16 ± 0.29) mJy in B and (4.56 ± 0.30) mJy in V .

During our monitoring campaign, the total B fluxes lay in the range between 5.69 mJy and 6.78 mJy with a mean of (6.24 ± 0.31) mJy. To derive the contempora-

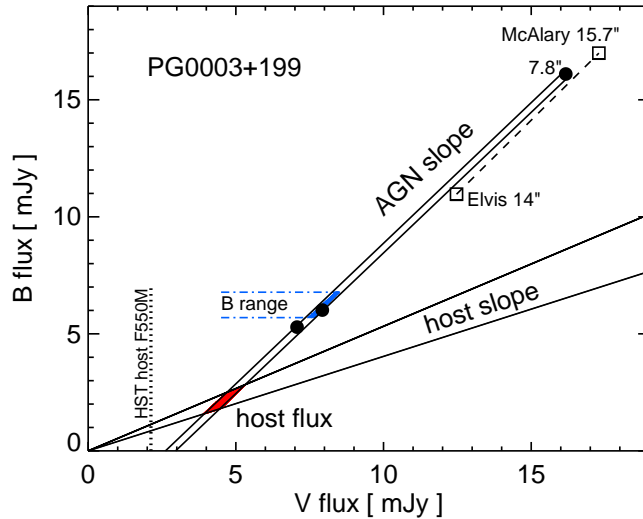


Figure 39: B versus V fluxes of PG0003+199, measured in a $7''.8$ aperture (black dots). Errors are within the size of the symbols. A linear least-squares fit to the three data points yields the range for the AGN slope plotted by the two steep lines. This slope is corroborated by the slope (dashed line) obtained with larger apertures $14''$ (Elvis et al. 1994) and $15''.7$ (McAlary et al. 1983). The range of host slopes plotted by the two shallow lines is taken from Sakata et al. (2010). The intersection area of the AGN and host slopes (red shaded) defines the host contribution. The blue shaded area marks the intersection of the AGN slope with the range of B fluxes during our Aug-Nov 2009 monitoring campaign. This area allows us to infer the range of V fluxes during the monitoring campaign. The vertical dotted line marks the host flux found in an aperture of $5'' \times 7''.6$ via modeling of HST F550M images by Bentz et al. (2009a). All data are corrected for galactic foreground extinction.

neous 5100\AA AGN luminosity, which is widely used in reverberation studies, we tried to extrapolate the host-subtracted B fluxes to restframe 5100\AA fluxes, using a power-law spectral shape ($F_\nu \propto \nu^\alpha$) with α constrained by Γ_{BV} . But this extrapolation results in large uncertainties, because α is sensitive to errors in Γ_{BV} . Therefore we applied the following procedure, inferring the V flux range in a first step.

During our monitoring campaign, the V fluxes should lie in the intersection area of the B flux range with the AGN slope (Fig. 39). That the data point from June 2011 lies in this area supports our suggestion. From this area we infer the V fluxes during the monitoring campaign, yielding a mean $f_V = (7.95 \pm 0.31)$ mJy.

Then, during our monitoring campaign the host-subtracted AGN fluxes are in the range (4.08 ± 0.43) mJy in B and (3.39 ± 0.40) mJy in V . From this range we interpolate the host-subtracted AGN flux of PG0003+199 at restframe 5100\AA $F_{5100} = (3.52 \pm 0.41)$ mJy, adopting for the interpolation that the AGN has a power-law spectral energy distribution ($F_\nu \propto \nu^\alpha$) analogous as above. To determine the errors on F_{5100} , we interpolated between the $1\text{-}\sigma$ borders of the flux values too. This means F_{5100} between $f_B + \sigma$ and $f_V + \sigma$ as well as between $f_B - \sigma$ and $f_V - \sigma$. At the distance of 112.6 Mpc this yields a host-subtracted AGN luminosity $L_{5100} = (3.13 \pm 0.36) \times 10^{43}$ erg s $^{-1}$. The 12% uncertainty includes the measurement errors, the uncertainty of the AGN and host slopes, and the AGN variations.

The AGN luminosity during our campaign derived with the FVG method is about a factor of two lower than the value $L_{5100} = (6.03 \pm 0.03) \times 10^{43} \text{ erg s}^{-1}$ derived with host galaxy modeling by Bentz et al. (2009a) for the data of the spectroscopic monitoring campaign (Peterson et al. 1998a). To understand this difference, we compared the numbers given in Bentz et al. (their Tables 7-9) with ours. Our aperture area (7".8 in diameter) is only 25% larger than that of Peterson's campaign (5" \times 7".6), and the additional flux from the outer region is negligible (Fig. 3 in Bentz et al. 2009a). The total observed (not extinction corrected) fluxes F_{5100} are similar at $7.83 \times 10^{-15} \text{ erg s}^{-1} \text{ cm}^{-2} \text{ \AA}^{-1}$ for our campaign and $7.68 - 8.81 \times 10^{-15} \text{ erg s}^{-1} \text{ cm}^{-2} \text{ \AA}^{-1}$ for Peterson's campaign. The main difference, however, lies in the estimate of the host contribution. Already in the early stage of the HST image decomposition with GALFIT, the Bentz et al. host flux ($f_{V,host} \sim F_{550M} = 1.88 \times 10^{-15} \text{ erg s}^{-1} \text{ cm}^{-2} \text{ \AA}^{-1}$) corresponds after extinction correction to 2.12 mJy, which is more than a factor two smaller than our $f_{V,host} = 4.56 \text{ mJy}$.

As illustrated in Fig. 39, it is hard to bring the small host flux from GALFIT modeling into agreement with the available FVG data. Firstly, we consider whether the discrepancy may be caused by failures in the FVG method. We find the following:

1. Altering the assumptions on the host slope does not bring the host contributions into agreement.
2. Although the AGN slope is determined by only a few data points, the wide flux range, which allows for a good slope determination, and the consistency between the AGN slope determined with apertures of 7".8 and $\sim 15''$ argues in favor of a steep AGN slope.
3. The correction for galactic foreground extinction may introduce errors in the AGN slope. However, the foreground extinction is relatively low (Table 1), and even without correcting for foreground extinction, the AGN slope remains steep ($\Gamma_{BV} = 1.16 \pm 0.05$), resulting in $f_{V,host} = (4.2 \pm 0.3) \text{ mJy}$, hence about twice the GALFIT host value.
4. If the host flux from GALFIT modeling were correct, then at low luminosity the AGN slope (of PG0003+199) would show a strong curvature towards redder colors, contradicting the results by Sakata et al. (2010) where the host galaxy lies on the linear extension of the AGN slope.

These four arguments lead us to conclude that the discrepancy between GALFIT and FVG host fluxes is not caused by errors in the FVG method alone. On the other hand, looking for potential error sources in the GALFIT method, it could be that a large fraction of the bulge and/or nuclear starbursts of PG0003+199 is unresolved on the HST images and therefore underestimated by the GALFIT modeling. Future data may clarify this issue.

Ark120

To separate AGN and host luminosity contributions, we applied the flux variation gradient method (Choloniewski 1981). Figure 40 shows the *B* versus *V* fluxes of Ark120, corrected for galactic foreground extinction (Schlegel et al. 1998). A linear least-squares fit to the flux variations yields $\Gamma_{BV} = 1.19 \pm 0.06$, consistent with the $\Gamma_{BV} = 1.20 \pm 0.10$ found by Winkler et al. (1992), using 20" aperture and adopting $E_{B-V} = 0.1$, and with the $\Gamma_{BV} = 1.22 \pm 0.02$ found by Doroshenko et al. (2008), af-

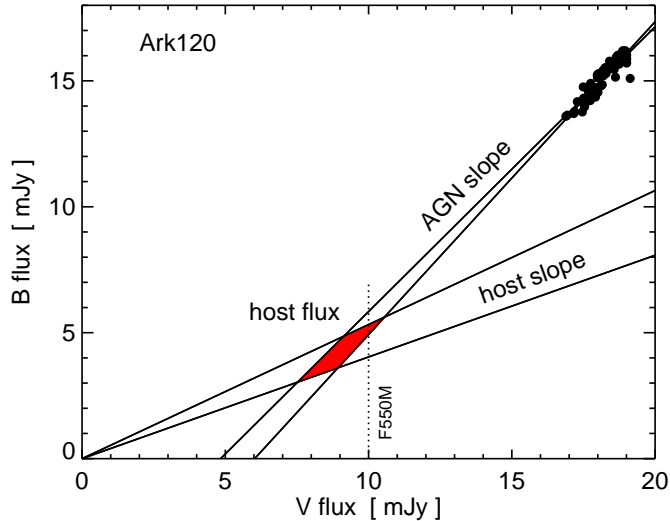


Figure 40: B versus V fluxes of Ark120, measured in a $7''.5$ aperture. The fluxes for each night (fat dots) follow a linear gradient yielding the range for the AGN slope. As host slope we adopted the range found by Sakata et al. (2010). The intersection of the two slopes (red shaded area) defines the host flux. The vertical dotted line marks the host flux found in an aperture of $5'' \times 7''.6$ via modeling of HST F550M images by Bentz et al. (2009a). All data are corrected for galactic foreground extinction.

ter correcting the values in their Table 3 for extinction⁷. The range of host slopes is taken from Sakata et al. (2010). The intersection area of the AGN and host slopes defines the host contribution. Averaging over the intersection area yields a mean host flux of $f_B = (4.26 \pm 0.59)$ mJy and $f_V = (9.02 \pm 0.62)$ mJy. Our host fluxes (in a $7''.5$ aperture) are consistent, albeit a bit high, when compared with the values $f_B \approx 4.5$ mJy and $f_V \approx 9$ mJy (in a $15''$ aperture) from a FVG analysis of $UBVRI$ data (Doroshenko et al. 2008). Subtracting our host fluxes from the total fluxes, we obtain the host-subtracted B and V fluxes and then by power-law interpolation the rest-frame AGN flux $f_{5100} = (9.41 \pm 0.86)$ mJy. At the distance of 141.8 Mpc, this yields a host-subtracted AGN luminosity $L_{5100} = (13.27 \pm 1.21) \times 10^{43}$ erg s⁻¹. The uncertainty of the AGN luminosity is less than 10%.

The AGN luminosity during our campaign as derived with the FVG method is about 50% higher than the mean value $L_{5100} = (8.47 \pm 0.81) \times 10^{43}$ erg s⁻¹ derived with host galaxy modeling by Bentz et al. (2009a) for the data of the spectroscopic monitoring campaign (Peterson et al. 1998a). A detailed comparison of the parameters yields an aperture area ($7''.5$ in diameter) that is only 16% larger than that of Peterson’s campaign ($5'' \times 7''.6$), and the V band host fluxes agree within the uncertainties as shown in Fig. 40 (extinction-corrected: $f_V \approx 9$ mJy from our data and $F_{550M} \approx 10$ mJy from the HST/spectroscopic data base). However, the total observed (not extinction corrected) fluxes F_{5100} differ significantly at 13.4×10^{-15} erg s⁻¹ cm⁻² Å⁻¹ for our campaign and lying in the range $7.82 - 10.37 \times 10^{-15}$ erg s⁻¹ cm⁻² Å⁻¹ during Peterson’s eight-year campaign, hence are 30% – 70% larger in our campaign. This leads us to conclude that the AGN luminosity is $\sim 50\%$ higher during our campaign.

⁷ Because of a typo the value $V = 14.27$ mag in this table should be $V = 14.72$ mag to be consistent with the plotted values in their Fig. 4.

3C120

The total flux (AGN+Host) contains a contribution from the emission lines originating in the narrow line region (NLR). However, this contribution is less than 10% of the host galaxy flux in the B and V band (Sakata et al. 2010). We here denote the host galaxy flux including the NLR lines. The AGN fluxes have been corrected for galactic foreground extinction according to Schlegel et al. (1998).

We have plotted B and V total fluxes obtained during the same nights and through the same aperture in a flux-flux diagram. Figure 41 represents such a diagram. Again, the host color range is taken from Sakata et al. (2010) and drawn from the origin of ordinates (dashed lines). For the varying AGN flux (black dots), we use the OLS bisector linear regression in order to determine a range of possible AGN colors (solid thin lines). This regression yields a linear gradient of $\Gamma_{BV} = 1.12 \pm 0.04$. The result is consistent, within the uncertainties, with $\Gamma_{BV} = 1.11 \pm 0.02$ determined by Sakata et al. (2010) and $\Gamma_{BV} = 1.02 \pm 0.07$ obtained by Winkler (1997).

The cross-section of the host and AGN slope allows us now to split the superposition of fluxes in both filters. Averaging over the intersection area between the AGN and the host galaxy slopes, we obtain a mean host galaxy flux of 2.17 ± 0.33 mJy in B and (4.58 ± 0.40) mJy in V . Our host galaxy flux derived with the FVG method is consistent with the values $f_B \approx 2.10$ mJy and $f_V \approx 4.73$ mJy obtained by Sakata et al. (2010), considering the flux contribution of the narrow lines ([O III] 4959, 5007 Å,

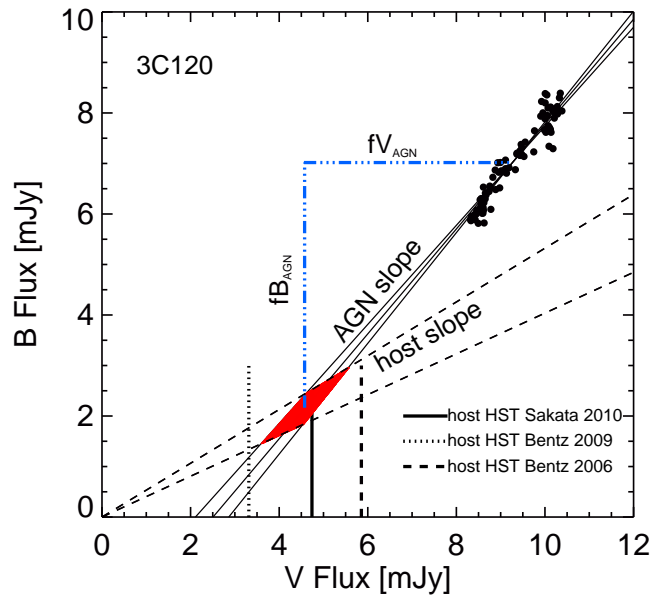


Figure 41: B versus V band FVG diagram of 3C120. The solid lines represent the bisector regression model and yields the range of the AGN slope. The dashed lines indicates the host galaxy flux contribution determined by Sakata et al. (2010). The intersection between the host galaxy and AGN slope (red area) gives the host galaxy flux in both bands. The vertical dotted lines show the host flux determined by Bentz et al. (2006) and Bentz et al. (2009a) respectively. While the solid line show the results obtained by Sakata et al. (2010). The dash-dotted blue lines represent the range of the AGN flux in both filters. Fluxes (black dots) were measured in a $7''.5$ aperture photometry and corrected for galactic foreground extinction.

H β , H γ) in each filter (his Table 8). We have also compared our results with those obtained by Bentz et al. (2006) and Bentz et al. (2009a) through modeling of the host galaxy profile (GALFIT, Peng et al. 2002) from the high-resolution HST images. On the nucleus-free image and through an aperture of $5'' \times 7''.6$, Bentz et al. (2006) determined a rest-frame 5100 Å host-flux $F_{5100} = 1.82 \times 10^{-15} \text{ erg s}^{-1} \text{ cm}^{-2} \text{ Å}^{-1}$. Using the color term factor from the HST-F550M filter to 5100 Å (their Table 3) we deduced the flux for the F550M filter to be $F_{F550M} = 1.74 \times 10^{-15} \text{ erg s}^{-1} \text{ cm}^{-2} \text{ Å}^{-1}$ and which corresponds after extinction correction to 4.62 mJy. Moreover, considering the contribution of the narrow lines in the V band (1.235 mJy), determined by Sakata et al. (2010), the previous value translates to 5.86 mJy.

In a subsequent investigation, Bentz et al. (2009a) determined a host galaxy flux of $0.78 \times 10^{-15} \text{ erg s}^{-1} \text{ cm}^{-2} \text{ Å}^{-1}$, which after extinction correction and adding the contribution of the narrow lines yield a value of 3.31 mJy.

The difference between the two results lies mainly in the type of model used for the decomposition of the galaxy, which was a first step considering general Sersic function for modeling bulges (Bentz et al. 2006) and in a second step performing the modeling with variations and improvements to the original profile (Bentz et al. 2009a). Our value ($f_{V,host} = 4.58 \text{ mJy}$) falls exactly in the middle of both values, suggesting that our determination is consistent, within the error margins, with those determined by Bentz et al. (2009b).

Also we should note that 3C120 together with another three objects (which showed larger residuals in the results obtained through the surface brightness fitting of the MAGNUM V band images (Figure 17, Sakata et al. 2010) in comparison to the results obtained for the HST images (Figure 14, Sakata et al. 2010 and Figure 3, Bentz et al. 2009a). This might suggest an possible overestimation in the value determined by Sakata et al. (2010). On the other hand, Bentz et al. (2009a) mentioned a possible underestimation for the final brightness of each host galaxy, which could be caused by the attribution of more flux to the sky background and PSF components in the model.

Taking account of our aperture area ($7''.5$ in diameter), which is only 16% larger than that of Peterson's campaign ($5'' \times 7''.6$) and considering that additional bandpass conversion factor between the HST-F550M filter and our Johnson V filter could increase the Bentz et al. (2009a) flux by about 10%, is highly plausible that the most contemporaneous value provided by Bentz et al. (2009a) could be underestimated. The results obtained by Bentz et al. (2009a) and Sakata et al. (2010) are plotted for comparison in Figure. 41.

The AGN fluxes at the time of our monitoring can be determined by subtracting the host galaxy fluxes from the total fluxes. During our monitoring campaign, the total B fluxes lay in the range between 5.81 and 8.39 mJy with a mean of $(7.02 \pm 0.11) \text{ mJy}$. The total V fluxes lay in the range between 8.17 and 10.38 mJy with a mean $(9.27 \pm 0.11) \text{ mJy}$.

Again we adopt an interpolation that the AGN has a power law SED ($F_\nu \propto \nu^\alpha$), between effective frequencies in the B and V bands respectively. The error was determined by a linear interpolation between the ranges of the AGN fluxes $\pm\sigma$ in both filters, as performed above.

To determine the luminosity, we used the distance of 145 Mpc (Bentz et al. 2009a). This yields $L_{AGN} = (6.94 \pm 0.71) \times 10^{43} \text{ erg s}^{-1}$. The AGN luminosity during our campaign is about half the mean value of $(12.40 \pm 2.6) \times 10^{43} \text{ erg s}^{-1}$ found by Bentz et al.

(2009a) and slightly lower than the value $(9 \pm 1) \times 10^{43} \text{erg s}^{-1}$ found by Grier et al. (2012a).

ESO 374-G25

First, in Figure 42 (left) we show the FVG diagram for different apertures that have been used to extract flux around the nucleus of ESO 374-G25 with correction for galactic foreground extinction (Schlegel et al. 1998). Using a very small aperture of $5''.0$, a big fraction of the total flux is lost. In this case nonetheless, we should expect a higher nuclear fraction in the remaining flux. As the AGN variation (Fig. 42, right) follows a clearly bluer slope than the host range by Sakata et al. (2010), we expect the datapoints to lie more clearly above the host range. The fact that this is not seen in our data (and the points even disperse down the lower limit of the host range using the $5''.0$ aperture in Fig. 42, left), allows us to conclude two potentially coexisting scenarios:

- The host galaxy, close to the nucleus, must be exceptionally red, while the AGN shows low flux variation relative to its average luminosity.
- The AGN could be intrinsically weak compared to its host, but showing an extreme relative variation.

In Barway et al. (2005), we can see examples of galaxies with similar properties and in every case, a ring structure turns out to be bluer than the bulge-like center of the galaxy. Considering this, the true host slope in our FVG diagram will not be linear as the dashed lines suggests. In fact, it will rise until our biggest aperture of $25''.0$ that is covering parts of the outer ring (reminding Fig. 10 above in Sect. 3.1). This potential offset towards bluer colors of the $25''.0$ fluxes can be seen in Fig. 42, left. Additionally, the bigger scatter here is a systematic effect, introduced by different atmospheric transmission, seeing and wind. These environmental conditions influence the low surface brightness (e.g. strong winds and seeing are driving flux of the nucleus out of the small aperture).

Selecting a $7''.5$ aperture around the nucleus delivers the lowest absolute scatter for the fluxes. Thus, we use this aperture to obtain an estimate for the AGN luminosity. The $7''.5$ aperture flux variation is shown in Fig. 42 (right).

Now we calculate the host flux contribution using the lower boundary of host-slopes from Sakata et al. (2010). During the monitoring campaign, the averages of the total fluxes have been $f_V = (2.11 \pm 0.03) \text{ mJy}$ and $f_B = (1.06 \pm 0.04) \text{ mJy}$. These fluxes are represented by the blue solid lines in Fig. 42, right.

According to Isobe et al. (1990), the preferred fitting algorithm is the ordinary least squares (OLS) bisector method. This is using the average angle between the $\text{OLS}(X|Y)$ (x -distance least square) $\text{OLS}(Y|X)$ (y -distance least square) and has proven itself to be the most reliable tracer of the underlying relation. The result is a slope of $\Gamma_{BV} = 1.33 \pm 0.22$. This is quite steep but not uncommon, when compared to the other type-1 AGN, as determined by Winkler et al. (1992).

The difficult task is now to determine the host contribution in the $7''.5$ aperture. As mentioned before, the flux variation, although being steep, is ranging (almost completely) inside the cone spanned by the host color slopes of Sakata et al. (2010) (dashed black lines in Fig. 42). The most reasonable assumption, in a physical sense, is that the host close to the nucleus is very red, otherwise the relative nuclear variations would be unrealistically big. Hence, we will assume the Sakata's lower red slope of $\Gamma_{BV}^{\text{host}} = 0.4$ for the host color and take the intersection with the AGN slope as host contribution.

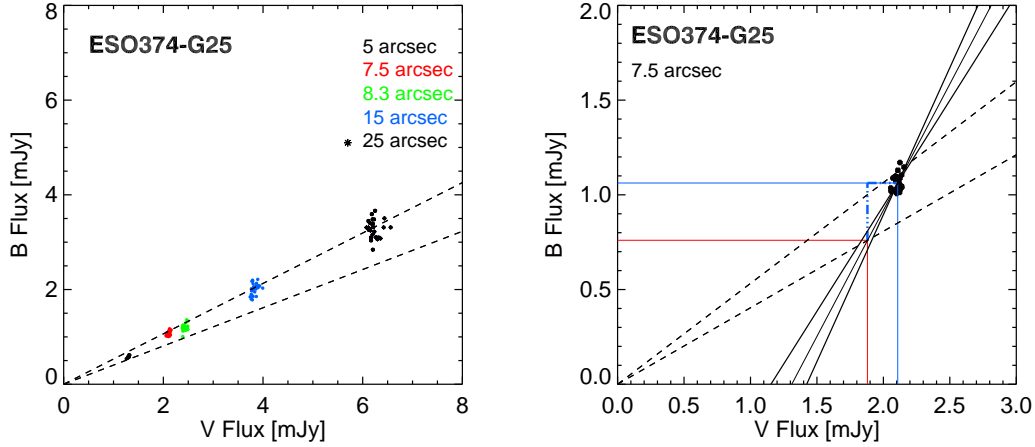


Figure 42: B versus V flux variations of ESO 374-G25, plotted together with the host slope estimates, adapted from Sakata et al. (2010). Left: Comparison of different apertures, used for the photometric extraction of the flux. Right: Flux variations measured in the 7.5 aperture. The black lines indicate the OLS bisector fit result of the datapoints. The blue lines mark the average fluxes measured, while the red lines designate the estimated host fluxes estimated from the lower boundary of Sakata’s host range. Flux errors are within the size of the symbols. All fluxes are corrected for galactic foreground extinction according to Schlegel et al. (1998).

The intersection is marked in Fig. 42 with red solid lines. This results in an estimate of the AGN flux of $f_{V,AGN} = 0.23$ mJy and $f_{B,AGN} = 0.31$ mJy with corresponding host fluxes of $f_{V,host} = 1.88$ mJy and $f_{B,host} = 0.75$ mJy. For the further analysis, we will assume 50% relative errors for these fluxes.

From this range we interpolate the host-subtracted monochromatic AGN flux F_{5100} , adopting for the interpolation that the AGN has a power-law spectral energy distribution ($F_\nu \propto \nu^\alpha$) between the determined B and V band fluxes.

At the distance of 103 Mpc this yields a host-subtracted AGN luminosity $L_{5100} = (1.85 \pm 0.93) \times 10^{42}$ erg s $^{-1}$. The large uncertainty includes the conservative 50% uncertainty of the AGN flux separation, the measurement errors and the standard deviation of the AGN flux variations.

3.5.4 The BLR size – Luminosity relationship

An important result from spectroscopic reverberation mapping is the relationship between the BLR size and the nuclear luminosity $R_{BLR} \propto L^\alpha$ with a predicted slope of $\alpha = 0.5$ (Netzer 1990; Netzer and Marziani 2010). This relationship allows one to derive the virial black hole mass for high-redshift AGN from single-epoch spectra by inferring R_{BLR} from L (e.g. Vestergaard 2002; Netzer 2003, McLure and Dunlop 2004). While early observations indicated $\alpha = 0.6 \pm 0.1$ (Kaspi et al. 2000, 2005), for $H\beta$ line and 5100 \AA luminosity a recent analysis including host galaxy subtraction yields $\alpha = 0.519 \pm 0.063$ (Bentz et al. 2009a). The true slope of the current $R_{BLR} - L$ relationship depends also on the adopted cosmology, because the more luminous sources are at higher redshift than the low-luminosity AGN. Here we adopt $H_0 = 73 \text{ kms}^{-1}\text{Mpc}^{-1}$, $\Omega_m = 0.27$ and $\Omega_\lambda = 0.73$.

The current $R_{\text{BLR}} - L$ relationship exhibits a large scatter about an order of magnitude in both R_{BLR} and L , and many objects have large error bars (see Fig. 43). The new photometric reverberation measurements shift the position of 3C120, PG0003+199 and Ark120 in this diagram outside the quoted error range of the previous positions. Since we measure all parameters in a different epoch than the literature values, this is not surprising, because the optimally-emitting BLR region is quick to adapt to changes of L (Baldwin et al. 1995). But notably, the shift seen in the Figure is generally higher in L than in R_{BLR} . The new positions of PG0003 and Ark120 are about 50% closer to the relationship fitted by Bentz et al. (2009a), while 3C120 moved almost parallel to its slope with respect to the newly measured values by Grier et al. (2012a), but also considering the result obtained in 2008 by Bentz et al. (2009a) (green box in Fig. 43). However, the older result has a noticeably bigger scatter in the time lag estimate. Nonetheless, this is demonstrating that the optimally-emitting BLR cloud's distance scales with the nuclear luminosity according to photoionization physics.

The new result for ESO 374-G25 lies left above the relationship. On the one hand, this may be caused by an incorrect estimation of the host to AGN flux contribution in

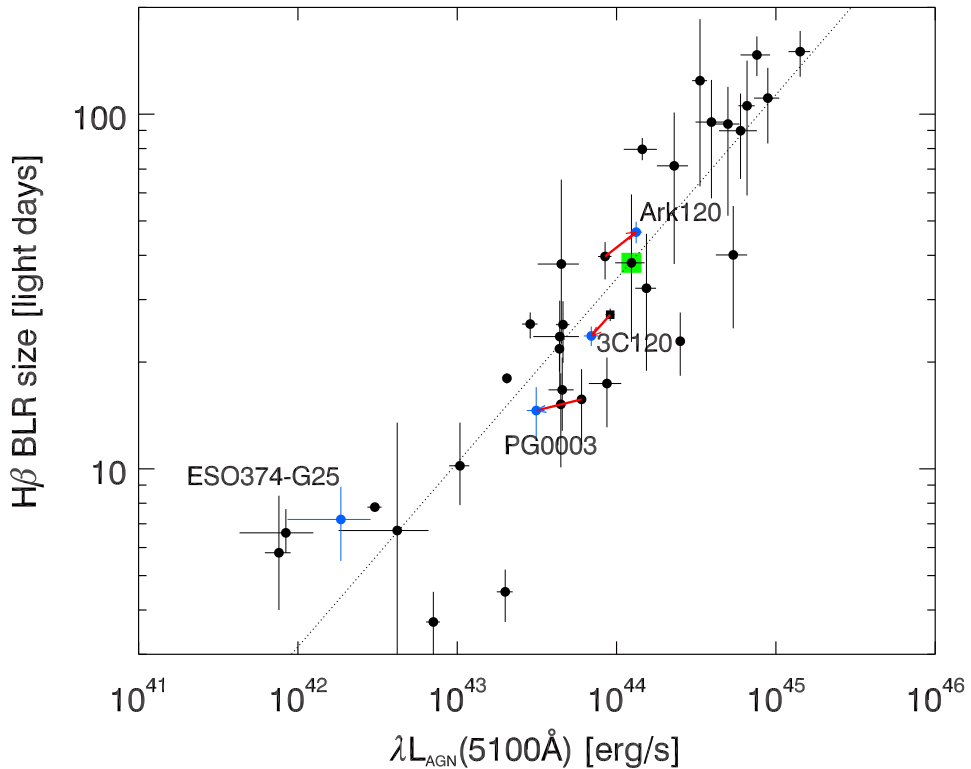


Figure 43: $R_{\text{BLR}} - L$ relationship from data of Bentz et al. (2009a) (black dots) and fit with a slope $\alpha = 0.519$ (dashed line). The diagram is zoomed to contain the objects presented in this work (blue dots). The red arrows show the shifts from the previous literature values to our newly determined ones. The red arrow of 3C120 is drawn from the value (black square) obtained by Grier et al. (2012a) and is parallel to the regression slope. There is another older result of 3C120 by Bentz et al. (2009a), highlighted with a green square.

our FVG diagram (Fig. 42 in Sect. 3.5.3). As argued before, it is possible that the host galaxy bulge in vicinity to the AGN is even redder than the lower slope $\Gamma_{BV} = 0.53$ of Sakata et al. (2010). On the other hand, our measured τ_{rest} may be too high. This can be explained by the fact that we were only equipped with filters that are narrower than the actual $H\alpha$ line, especially with the [SII] filter, we had to use most of the time (see the convolution of this filter with the line profile in Fig. 20).

Concluding, this suggests that well-sampled reverberation data and improved host-free AGN luminosities may reduce the scatter of the $R_{\text{BLR}} - L$ relationship. Certainly, a true scatter may remain, simply because AGN are complicated objects and the R_{BLR} determination depends on the continuum variability pattern and the geometry of the BLR that produces the line echo.

3.6 CONCLUSION AND OUTLOOK

While spectroscopic reverberation mapping is the only way to explore the details of the innermost AGN structure and kinematics of the BLR (e.g. Kollatschny 2003a,b; Kollatschny and Zetzl 2011), the advantage of photometric reverberation mapping with suitable filters is to efficiently measure BLR sizes and host-subtracted luminosities for large AGN and quasar samples – even with small telescopes. Photometric broad- and narrow band monitoring of a sample of 100 quasars ($V < 18 \text{ mag}$) can be performed with 1-m telescopes in an equivalent to three years observing time.

The data, as presented in this work is novel for all four objects; of course for ESO 374-G25, of which the BLR size has never been measured before. For the other three sources this statement can be justified, because our lightcurves were recorded in different epochs, where the AGN luminosities have apparently changed. Our results (overview in Table 3) can be summarized as follows.

- For ESO 374-G25, we could determine a rest-frame $H\alpha$ lag of $\tau_{\text{rest}} = 11.1 \pm 2.6$ days from a DCF analysis (Edelson and Krolik 1988) together with a nuclear luminosity of $L_{\text{AGN}} = (1.85 \pm 0.93) \times 10^{42} \text{ erg s}^{-1}$ obtained from the FVG analysis (Choloniewski 1981; Winkler et al. 1992). From spectroscopy we can determine a $H\alpha$ line dispersion of $\sigma = (2190 \pm 550) \text{ km/s}$ (Section 3.4.4). This allows us to calculate a virial black hole mass of $M_{\text{virial}} = (10.4 \pm 5.7) \times 10^6 M_{\odot}$.
- For PG0003+199 we could determine an average $H\alpha$ BLR lag of $\tau_{\text{rest}} = (20.0 \pm 2.4)$ days. With the line dispersion of $(870 \pm 220) \text{ km/s}$, we derive a virial black hole mass of $M_{\text{virial}} = (3.0 \pm 1.5) \times 10^6 M_{\odot}$. Compared to previous spectroscopic RM studies, the position in the $R_{\text{BLR}} - L$ diagram is now closer to the expected $a = 0.5$ than in Bentz et al. (2009a).
- Ark120 has an average $H\beta$ lag of $\tau_{\text{rest}} = (46.5 \pm 3.25)$ days. Combined with the line dispersion of $\sigma = (1950 \pm 490) \text{ km/s}$ $M_{\text{virial}} = (35 \pm 17) \times 10^6 M_{\odot}$. The position in the $R_{\text{BLR}} - L$ diagram is now also closer to the expected $a = 0.5$ with respect to the result of Bentz et al. (2009a).
- For 3C120, we could determine a $H\beta$ lag of $\tau_{\text{rest}} = (23.6 \pm 1.69)$ days and a nuclear luminosity of $L_{\text{AGN}} = (6.94 \pm 0.71) \times 10^{43} \text{ erg s}^{-1}$. As result with the highest precision (see Fig. 43), 3C120 was traveling to higher luminosities in Grier et al. (2012a) on a parallel path to the $\alpha = 0.519$ slope. Due to the quick adaption of the BLR emission distance to L , our measurements agree very well with Grier et al. (2012a). This demonstrates impressively that photometric RM, as

performed with a 15 cm refractor telescope is well competitive to spectroscopic RM performed on a 1.3 m mirror telescope (McGraw-Hill telescope on Kitt Peak, as used by Grier et al. 2012a). With a single epoch spectrum, for $H\beta$, we obtain $\sigma = (1264 \pm 316)$ km/s. The virial black hole mass is then $M_{\text{virial}} = (10.4 \pm 5.3) \times 10^6 M_{\odot}$.

In the cases of Ark120 (ESO 374-G25), the $H\beta$ ($H\alpha$) line contributes to only 50% of the flux in the narrow band pass we used. This suggests that photometric reverberation mapping of emission line lags works even for broader bands, as long as the line contributes at least 50% to the band pass. Also, it is worthwhile testing the method even for weaker emission lines contributing less than 50% to the band pass. The upcoming Large Synoptic Survey Telescope (LSST) is equipped with six broad band filters and will discover thousands of variable AGN. The $H\alpha$ line is shifted into the i' and z' bands at $z \approx 0.16$ and $z \approx 0.38$, respectively, and may be strong enough to contribute about 50% to these broad bands. While an approximate photometric redshift may be sufficient to determine the filter that contains the $H\alpha$ line, it is desirable to take a spectrum of the AGN, in order to measure an accurate redshift, also for luminosity determination, and the line dispersion for black hole mass estimates. To determine the $H\alpha$ line lag, the neighboring filters, which are largely free of line emission, may be used to interpolate and remove the continuum variations underneath the $H\alpha$ line, much like what we did for Ark120.

Recently, an interesting statistical alternative to our method has been proposed by Chelouche and Daniel (2012), which is specifically designed for large samples of AGN light curves expected to be obtained with the LSST. Consider AGN light curves in two band passes, curve X (tracing the continuum largely free of emission lines) and curve Y (tracing the emission line with underlying continuum): While our approach aimed to remove the continuum contribution from curve Y by subtracting a scaled X curve, Chelouche & Daniel propose to use the light curves X and Y unchanged, and to subtract the autocorrelation of X from the cross correlation of X and Y , in order to determine the line lag. Numerical simulations with synthetic AGN light curves and the treatment of four archival PG quasar light curves yield lags that are (in three out of four cases) consistent with spectroscopic results. However, the reported lag uncertainties of individual AGN are large ($\sim 50\%$), and only for averages of large ensembles of several hundred AGN does the obtained lag appear satisfying. Future optimization, which combine our approach with that of Chelouche & Daniel, would be intriguing.

Finally we outline a modification of the proposals by Elvis and Karovska (2002) and Horne et al. (2003) for determining quasar distances from reverberation data, hence probing dark energy. The luminosity difference between the open Einstein – de Sitter cosmology ($\Omega_M = 0.2, \Omega_{\Lambda} = 0$) and the concordance cosmology ($\Omega_M = 0.3, \Omega_{\Lambda} = 0.7$) is 20%–30% at redshift $0.4 < z < 0.8$ (Riess et al. 1998). From the $R_{\text{BLR}} - L$ relationship we conclude that two quasar samples with the same R_{BLR} distribution, one sample at low redshift and one sample at high redshift, should have the same intrinsic L distribution. Thus one may constrain the luminosity for different cosmologies by measuring the BLR size and the host-subtracted brightness of quasar samples at different redshifts. If for objects matching in R_{BLR} the true scatter in L can be reduced to about a factor 2 (= 200%), the mean luminosity of 1000 quasars may be determined with a statistical accuracy of $200\% / \sqrt{1000} = 6\%$, enabling a $3\sigma - 5\sigma$ detection of a cosmological 20% – 30% luminosity difference.

FINDING MEGAMASER CANDIDATES

In this Chapter, we revisit the connection between maser detection rate and nuclear obscuration by using the strength of the [OIV] $25.9\mu\text{m}$ emission line (for short [OIV]) as tracer for the intrinsic AGN strength. [OIV] has been found to be largely unaffected by obscuration (e.g., Genzel et al. 1998, Haas et al. 2005, Meléndez et al. 2008a, Baum et al. 2010). We combine the strategies of Bassani et al. (1999) and Meléndez et al. (2008a). The observed X-ray (2-10 keV) flux normalized by [OIV] should provide information about X-ray absorption, even in the case of X-ray scattering caused by a complex geometry or for Compton thick cases. We compare the distribution of X-ray / [OIV] for masers and non-masers. In addition, after normalization of the $7\mu\text{m}$ flux by [OIV], we inspect the relation between maser detection rate and the absorption of the $7\mu\text{m}$ dust continuum emitted from the nuclear torus, as well as maser detection and the absorption of the [OIII] 5007\AA emission from the central part of the NLR. The results of this study have already been published in Ramolla et al. (2011).

4.1 SAMPLE SELECTION AND DATA

Now we will present our selection criteria, based on different catalogs. Then we explain the data properties with respect to the maser information and our [OIV] and $7\mu\text{m}$ measurements.

4.1.1 *The parent sample*

At first glance, one could take all known masers and non-masers from the literature and compare their properties, such as $L_X / L_{[\text{OIV}]}$. However, to determine nuclear obscuration, one also needs to know the range of $L_X / L_{[\text{OIV}]}$ for unobscured (preferentially Sy1) sources, which should comprise a complete sample free of any selection bias. However, the selection of Seyferts for which a maser search has been performed has not followed any clear criteria. Even worse, most maser searches have been performed on Sy2s, but only a small number on Sy1s. Because incomplete sample selection may influence the results, we decided to start with complete Seyfert catalogs with well-defined selection criteria. We created a master sample from the following three catalogs, consisting of a total of 163 sources:

- The magnitude-limited complete sample of the CfA Redshift Survey by Huchra and Burg (1992), which was supplied with updated Seyfert-type information from the NED database.
- The $12\mu\text{m}$ active galaxy sample by Spinoglio and Malkan (1989), complemented by that of Rush and Malkan (1993).
- The IRAS F25/F60 flux-ratio selected sample by de Grijp et al. (1992), as refined by Schmitt et al. (2003).

Table 4 documents how the 163 sources are distributed over the three catalogs, and how these catalogs match or complement each other. In general, we present the results

for the combined sample, but – where necessary – also for the catalogs individually (Tab. 5).

In Section 4.2.4, we discuss potential differences between the three samples and our combined sample and all other known masers outside it. The Spitzer data archive contains IRS spectra (at $\sim 26\mu\text{m}$) for 126 of the 163 sources classified as Seyferts according to the NED. This data is listed in Tab. 6. It covers the complete CfA-sample of 54 Seyfert Galaxies. It includes 107 of 118 Seyferts (two blazars included as Sy1) from the $12\mu\text{m}$ selected sample. For the IRAS sample, we found useful IRS spectra for 34 of 60 sources.

4.1.2 Maser information

The parent sample of 126 sources with Spitzer spectra was searched for known maser-detections and non-detections. For this purpose, we used the lists compiled by Benkert et al. (2009) and those on the website of the Hubble constant Maser Experiment (HoME)¹.

This search results in 18 masers (3 Sy1s, 15 Sy2s), 96 non-masers (36 Sy1s, 60 Sy2s), and 12 sources (10 Sy1s, 2 Sy2s) for which no maser search has yet been performed (henceforth called maser-unknown). The results are listed in Tab. 6, Col. 2.

4.1.3 [OIV] line and $7\mu\text{m}$ continuum flux

Our analysis is based on public archival IRS spectra of Seyfert galaxies. We used the post-basic-calibration data (PBCD), reduced by the Spitzer Science Center's (SSC) pipeline. This included droop-, stray-light-, cross-talk- and saturation correction, dark subtraction, flatfielding and coaddition.

Where possible, IRS high resolution spectra with $R \sim 600$ were chosen, to avoid the contamination of $[\text{OIV}]_{25.89\mu\text{m}}$ by the neighboring $[\text{FeII}]_{25.99\mu\text{m}}$ emission line. If high resolution spectra were not available, the low-resolution spectra were used, after a background subtraction had been performed by the SSC pipeline.

For the high resolution data collected with the shorter (4.7×11.3 and 11.1×22.3 arcsec) slits, separate background observations had to be chosen to evaluate the background contribution. This data reduction steps were performed in Ramolla (2009) and will not be detailed here again. In short it was performed by comparing the background with the source fluxes at the presumably weakest part of the source spectrum in the 9 and $10\mu\text{m}$ rest frame; with the result that the background contribution is negligible compared to the conservatively assumed flux calibration errors of 15%. The resulting errors are calculated from an assumed 15% flux calibration error and the error in the line-fitting routine.

The [OIV] flux was extracted by fitting a simple spectral model to a wavelength window of $\sim 0.3\mu\text{m}$ around the [OIV] line. This model consists of a linear base, convolved with Gaussian profiles that also include the neighboring [FeII] line. No [OIV] aperture corrections had to be applied, because for both, high- and low-resolution data, the slit apertures cover an area larger than the expected size of the NLR, as esti-

¹ <http://www.cfa.harvard.edu/~lincoln/demo/HoME/surveys/survey.html> compiled from Becker et al. (1993); Braatz (2008); Braatz and Gugliucci (2008); Braatz et al. (1996, 2003, 2004); Claussen and Lo (1986); Greenhill et al. (1990, 1995, 1997, 2002); Hagiwara et al. (2002, 2003); Haschick and Baan (1985); Henkel (2008); Henkel et al. (1984, 1986, 1998, 2005); Kondratko et al. (2006a,b); Nakai et al. (1995); Sato et al. (2005); Zhang et al. (2006)

mated from the relationship² of [O III] luminosity to NLR size, found by Bennert et al. (2002).

We calculated the $7.6\ \mu\text{m}$ (henceforth for short $7\ \mu\text{m}$) continuum flux from the background-subtracted IRS low-resolution spectra. We used a modified version of the PAHFIT code by Smith et al. (2007), which estimated the continuum in the 5 to $11.8\ \mu\text{m}$ branch. As suggested by Smith and Draine (2008), we did not correct the continuum fit for the silicate feature at $9.7\ \mu\text{m}$. The $7\ \mu\text{m}$ continuum flux was then calculated from the PAH flux and the equivalent width of the features at $7.4\ \mu\text{m}$, $7.6\ \mu\text{m}$, and $7.8\ \mu\text{m}$. The uncertainties in the $7\ \mu\text{m}$ continuum are conservatively estimated to be smaller than 30%, which is sufficient for our purpose. In a few cases, the AGN contribution may be contaminated by nuclear ($<3.7''$) star formation (e.g. Deo et al. 2009). We verified that the effect on our statistical analysis is negligible compared to high resolution ground-based MIR observations.

The [OIV] and $7\ \mu\text{m}$ fluxes are listed in Tab. 6. The values are consistent with those derived by others (Buchanan et al. 2006, Deo et al. 2007, Deo et al. 2009, Tommasin et al. 2010).

4.1.4 X-rays and [O III] flux

The 2-10 keV hard X-ray data were obtained by several observers using ASCA, Beppo SAX, Chandra, and XMM. We collected the data from the NED; in case of multiple entries we chose the latest detection.

We collected [O III] 5007\AA emission line fluxes from various literature sources, as listed in Tab. 6. Because of the large uncertainties, we applied neither an extinction correction nor aperture correction for the [O III] fluxes. Those aperture corrections would affect few very nearby sources, but most sources are sufficiently distant to ensure that any bias in the statistical analysis is small.

4.1.5 Additional maser sources

On the one hand, our combined sample is drawn from the CfA, $12\ \mu\text{m}$, and IRAS F25/F60 catalogs, which contains 15 Sy2 maser sources with Spitzer spectra. On the other hand, a total of 52 masing Sy2 are known so far (Bennert et al. 2009; Zhang et al. 2010), although these are drawn from different AGN catalogs using inhomogeneous criteria.

To compare the 15 Sy2 masers of our combined sample with the remaining 37, we also analyzed available Spitzer spectra and gathered additional [O III] and X-ray fluxes for them from the literature in the same manner, as we did for our combined sample. This results in an “off-sample” list of 37 Sy2 masers that is appended to Tab. 6.

4.2 RESULTS AND DISCUSSION

Our combined sample of 126 sources contains 114 maser and non-maser sources (12 maser-unknown excluded), but not all of them have data for all the observables considered here (X-rays, $F_{7\ \mu\text{m}}$, [O III]). Therefore, we compare the maximum possible subsets

² $\log(R_{\text{NLR}}) = (0.52 \pm 0.06) \times \log(L_{[\text{O III}]}) - (18.5 \pm 2.6)$

of observable pairs, and discuss the implications in the framework of the AGN unified model. Therein we consider as components the accretion disk supposed to host the maser, the dust torus, the bi-conical NLR, and the host galaxy. We denote by Sy1s the subtypes between Seyfert 1.0 and 1.5, and by Sy2s those between Seyfert 1.8 and 2.0. All figures contain a combined error bar in the lower right corner that is averaged from all relative errors in this measurement. Since the literature sources do not have uniformly presented errors, we do not perform this step for the X-ray, [O III], and H₂O luminosities.

4.2.1 Nuclear X-ray obscuration

Figure 44 shows the observed hard X-ray versus [O IV] line luminosities, and Figure 45 the $L_X / L_{[\text{OIV}]}$ histogram. The main characteristics are:

- On average, Sy1s have an X-ray / [O IV] ratio that is about 10 times higher than Sy2s.
- Sy2 non-masers are evenly distributed over the entire range occupied by Sy2 masers and Sy1s (Fig. 44).
- Sy2 masers are almost disjoint from Sy1s. At a given [O IV] luminosity, Sy2 masers have on average about a factor of four lower X-ray luminosity than Sy2 non-masers (Fig. 45). Likewise, the few Sy1 masers have a lower X-ray luminosity than Sy1 non-masers.³
- Six out of 12 sources without masing information, but L_X and $L_{[\text{OIV}]}$ available (see Tab. 6), show the same trends as the Sy1s and Sy2s with masing information (see Tab. 5). They are not plotted, to avoid the overcrowding of Figs. 44 and 45, with too many different symbols.

We assume that the X-ray deficit, i.e. the decrease in $L_X / L_{[\text{OIV}]}$, is caused by obscuration, probably in the molecular dust torus. Figures 44 and 45 then clearly demonstrate that masers are found almost exclusively in Sy2s with heavy nuclear obscuration, while non-maser Sy2s exhibit a broad range of X-ray absorption. A two-sided Kolmogorov-Smirnov (KS) test, applied to the $L_X / L_{[\text{OIV}]}$ distribution, infers a probability of 18% that the Sy2 masers and non-masers are drawn from the same parent population. Our results agree with those of Greenhill et al. (2008) and Zhang et al. (2010), who find that about 60% of the masers are Compton-thick.

Assuming that Sy1s are almost unobscured, the obscured sources populate the $L_X / L_{[\text{OIV}]}$ range below 10 in Fig 44. Thus, masers almost completely populate the range of obscured sources. This range also surprisingly contains numerous non-masers. To more clearly understand why the maser search failed in these absorbed sources, we consider the influence of observed brightness. Fig. 46 shows the X-ray and [O IV] flux distribution (instead of the luminosity distribution). The Sy2 masers and non-masers exhibit a flux-dependence in their [O IV] distribution. Sources with low [O IV] flux are more frequently classified as non-masers (2 Sy2 maser and 12 Sy2 non-maser at $L_{[\text{OIV}]} < 10^{-16} \text{ Wm}^{-2}$), while sources with high [O IV] flux are more frequently classified as masers (6 Sy2 maser and 5 Sy2 non-maser at $L_{[\text{OIV}]} > 10^{-15} \text{ Wm}^{-2}$). Fig. 47 displays the [O IV] fluxes of all Sy2s lying below the dividing line between obscured

³ The Sy1 masers are NGC 4051, NGC 4151, and UCG 5101. Note that both NGC 4051 and NGC 4151 have relatively low maser H₂O luminosity, and UCG 5101 is an ultra-luminous infrared galaxy so that the maser luminosity could arise from starburst regions rather than from the AGN accretion disk.

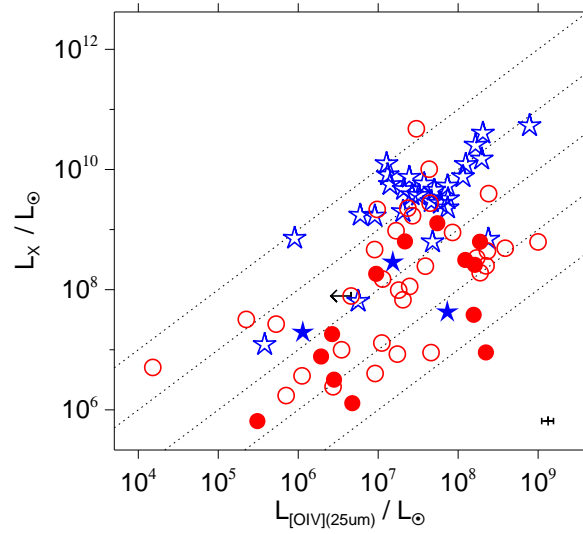


Figure 44: Observed 2-10 keV X-ray versus [OIV] line luminosity. Blue stars represent Sy1s (Sy 1.0-1.5), red circles Sy2s (Sy 1.8-2.0). Filled symbols are masers, open symbols are non-masers. The dotted lines mark fixed $L_X / L_{[\text{OIV}]}$ ratios of 1000; 100; 10; 1; 0.1 (from top to bottom). The error-bar in the lower right corner is the average relative error of all [OIV] measurements.

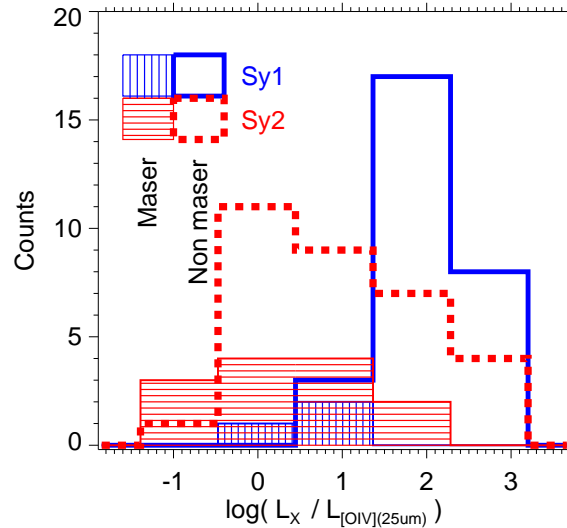


Figure 45: Histogram of the $L_X / L_{[\text{OIV}]}$ ratio of the data points shown in Fig. 44. The red dashed line represents Sy2 non-masers, whereas the blue thick line represents the Sy1 non-masers. The maser-detections are represented by the dashed surfaces - blue and vertically dashed for Sy1, red and horizontally dashed for Sy2. The one upper limit is excluded.

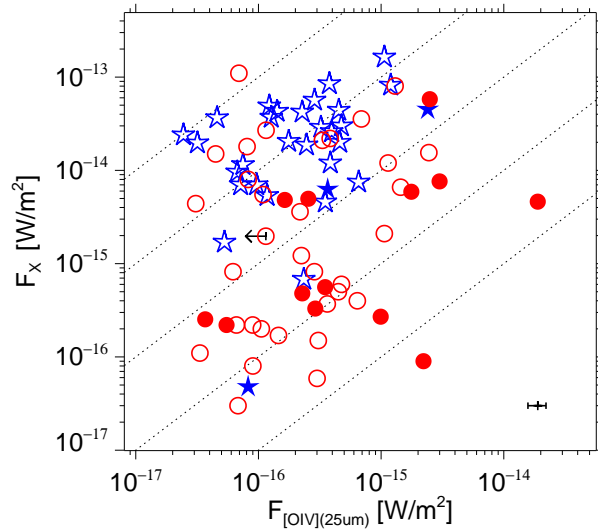


Figure 46: Observed X-ray versus [OIV] line flux. Symbols and colors are as in Fig. 44. The dotted lines mark fixed flux ratios of 1000; 100; 10; 1; 0.1 (from top to bottom). The error bar in the lower right corner is the average relative error in all [OIV] measurements.

and unobscured sources ($L_X : L_{[\text{OIV}]} \approx 10$). Among this subset of obscured Sy2s, the frequency of non-masers rises constantly towards lower [OIV] fluxes, in contrast to the distribution of masers. This incidence is consistent with an observational bias against the maser-detection for faint AGN. This implies that a relation exists between [OIV] flux and H_2O flux, which is indeed observed in Fig. 52 and discussed in Section 4.2.5.

Because the detection of maser emission appears to be biased against sources with low flux, we conclude that among obscured sources the true fraction of masers is higher than indicated by Fig. 45.

4.2.2 Extended obscuration of the dust torus and NLR

Figure 48 shows a histogram of the MIR $7\mu\text{m}$ continuum to [OIV] line ratio. The striking features of this diagram are:

- Sy2s populate about the same total range as Sy1s, but show a prevalence of lower $7\mu\text{m} / [\text{OIV}]$ values, i.e. a $7\mu\text{m}$ continuum deficit. On average, the ratio $7\mu\text{m} / [\text{OIV}]$ of Sy2s is about a factor of three lower than that of Sy1s. This is consistent with the results obtained via radio normalization ($7\mu\text{m} / 8\text{GHz}$) by Buchanan et al. (2006, their Fig. 16).
- Among Sy2s, the $7\mu\text{m} / [\text{OIV}]$ ratio of masers is, on average, about a factor of two lower than that of non-masers. A KS test results in a probability of 3.7% that the Sy2 masers and non-masers are drawn from the same parent distribution. Flux considerations similar to those for $L_X / L_{[\text{OIV}]}$ suggest that the true $7\mu\text{m} / [\text{OIV}]$ separation of masers and non-masers will be even more pronounced once the observational bias against the detection of low flux masers is taken into account.

We assume that the deficit of the $7\mu\text{m}$ continuum in Sy2s is mainly caused by absorption of the torus dust emission. This absorption has to take place somewhere between

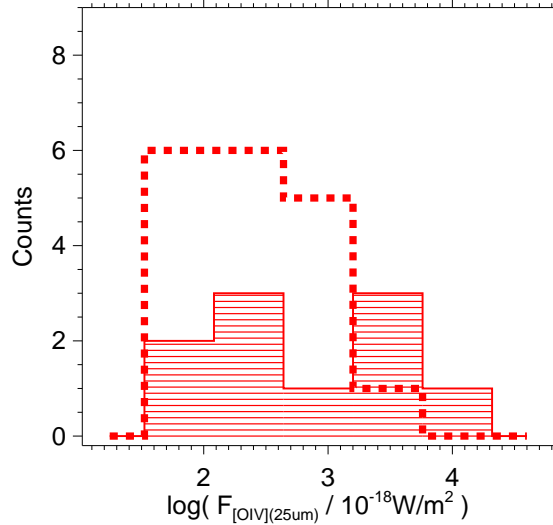


Figure 47: [OIV] flux histogram of Sy2 masers for absorbed sources from Fig. 46 with $L_X / L_{[\text{OIV}]} < 10$. Masers are represented by the shaded area, non-masars by the thick dashed histogram.

the emitting region and the observer, hence probably in the "halo" of the torus, i.e. in the outer part of the torus itself or in the host galaxy. It is possible that the scale height of this MIR-absorbing halo, i.e. the projected distance of absorbing material from the line-of-sight to the nuclear accretion disk, is (much) larger than the scale height of the torus itself. This is consistent with the results of a Spitzer study of CfA Seyferts (Deo et al. 2007), where sources with high $10 \mu\text{m}$ silicate absorption were found to have predominantly large host-galaxy inclinations and irregularities (merger events or interactions), both of which lead to absorption through the host.

To provide additional clues on the extent of the MIR-absorbing material, we consider the [OIII] 5007\AA versus [OIV] line luminosity as shown in Figures 49 and 50. The features of the [OIII] / [OIV] distribution are similar to those of $7 \mu\text{m}$ / [OIV]. Most Sy2s populate the same range as Sy1s, a few Sy2s show a [OIII] deficit, i.e. [OIII] / [OIV] ratios lower on average about a factor 3 compared to Sy1s, consistent with the results of Baum et al. (2010) for the $12 \mu\text{m}$ sample. The distribution pattern of masers and non-masars appears to be statistically indistinguishable. A KS-test results in a probability of 61% that the Sy2 masers and non-masars are drawn from the same parent population. However, the Sy2 subsample in Figures 49 and 50 shows a distinct tail towards lower ratios, potentially caused by absorption.

The [OIV] $25.9 \mu\text{m}$ line is ~ 50 times less affected by extinction than the optical [OIII] 5007\AA line. A low [OIII] / [OIV] ratio argues in favor of large obscuration, as explained in Haas et al. (2005). Another explanation of the very different [OIII] / [OIV] ratios could be the different radiation fields in the NLR. Because the [OIV] $25.9 \mu\text{m}$ line needs a higher ionization potential than the optical [OIII] 5007\AA line, AGN with a hard radiation field are expected to have a low ratio. The Sy2s with low [OIII] / [OIV] would then be those AGN with hard radiation fields. However, this is inconsistent with other spectroscopic MIR tracers such as the [NeII] $12.8 \mu\text{m}$ to [OIV] flux ratio (Meléndez et al. 2008b). Thus, we conclude that in Figures 49 and 50 the NLR of Sy2s with an [OIII] deficit is considerably obscured.

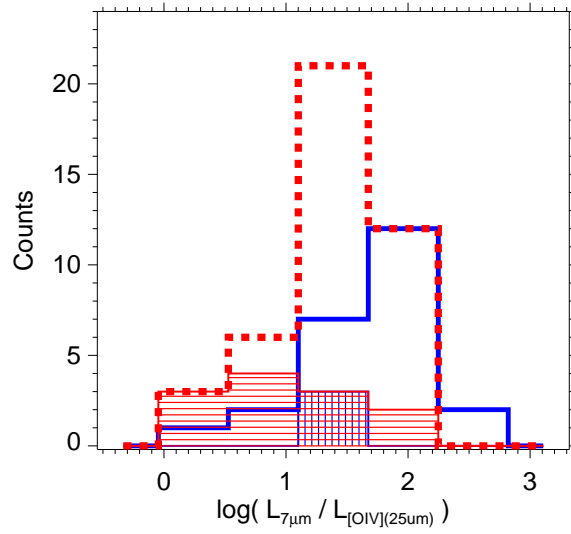


Figure 48: Histogram of the $7\ \mu\text{m}$ continuum to [OIV] line ratio. Legend as in Fig. 45. All 21 upper limits from Tab. 6 are excluded.

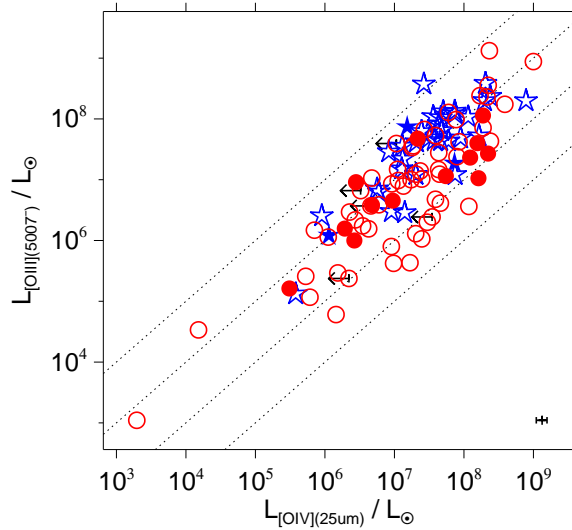


Figure 49: Distribution of [OIII] 5007\AA versus [OIV] $25.9\ \mu\text{m}$ luminosity. Symbols are as in Figure 44. The dotted lines mark fixed ratios 10; 1; 0.1; 0.01 (from top to bottom). The error bar in the lower right corner is the average relative error of all [OIV] measurements.

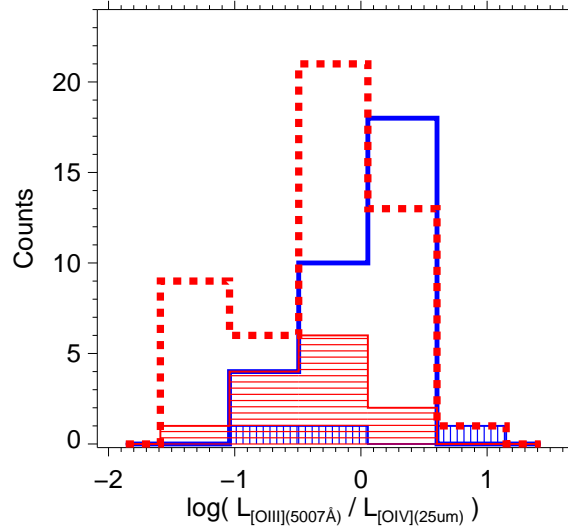


Figure 50: Histogram of the [O III] to [O IV] ratio. Legend as in Fig. 45. Five upper limits are excluded.

While the [O III] obscuration may occur mainly in the innermost part of the NLR, the large extent (>1 kpc) of the NLR suggests that the absorption is not confined to the region encircled by the dust torus. The sky-projected distribution of the absorbing material might reach further out to a considerable distance (several hundred parsec) from the line-of-sight to the nuclear accretion disk. The presence of moderately extended [O III] absorption, as well as the similarity of the $7\mu\text{m} / [\text{O IV}]$ and $[\text{O III}] / [\text{O IV}]$ diagrams supports the picture that the MIR absorption also takes place in a moderately extended layer, i.e. the torus halo mentioned above. Although both observables $7\mu\text{m}$ and [O III] appear to be affected by absorption in a similar fashion, we note that the distribution of $7\mu\text{m} / [\text{O III}]$ spans a wide range (2-700). This is unsurprising in view of the diversity of the orientation-dependent appearance of the involved emitters and absorbers even for a simple AGN model.

4.2.3 Combined picture

Why do masers and non-masers have such different distributions in $X\text{-ray} / [\text{O IV}]$, while their distribution in $7\mu\text{m} / [\text{O IV}]$ looks more similar?

Because masers need a large line-of-sight column density of velocity coherent gas, they are expected to be predominantly detected in edge-on accretion disks. Thus, the maser detection or non-detection can tell us about the disk orientation with respect to the line-of-sight. To constrain the implications in the framework of the AGN unified model, we consider two extreme cases:

1. For a disk seen edge-on, the maser is obviously most easily detected and the molecular torus is also seen more or less edge-on. In this case, the nuclear accretion disk (and its corona) is shielded by the torus, so that the X-rays are heavily obscured. If additional extended material, capable of obscuring the MIR emission, does not lie in the torus plane, the $7\mu\text{m} / [\text{O IV}]$ ratio is lower.
2. For a non-maser, both the disk and torus appear to be sufficiently tilted away from edge-on, so that the nuclear X-ray absorption is relatively low. In addition,

our diagrams indicate the existence of non-masers, where the torus plane is seen edge-on, although in these cases the disk might be tilted out of this plane because of the locally different angular momentum. For a non-maser, the edge-on torus also causes a high obscuration of the X-ray nucleus. On the other hand, irrespective of the disk and torus orientation, the MIR continuum can be absorbed or not depending on the line-of-sight through the extended host.

From these two extreme cases, we see the following. While the requirement for heavy absorption of the nuclear X-rays is that the line-of-sight has to hit a rather compact area of very high column density, the area of the torus emission and even more so the area of the (bright) NLR emission is orders of magnitude larger, so that the absorber must also cover a larger area. If the absorption of X-rays and $7\ \mu\text{m}$ occurs on different spatial scales, the strength of the obscuration in each wavelength range may be sensitive to small differences in the aspect angle. Furthermore, because the MIR-absorbing material is located farther away from the line-of-sight to the nucleus, it is less reliable for predicting whether a maser will be detected.

4.2.4 Comparison of the three samples with other known masers

Our combined sample was compiled from three complete samples with good coverage in the Spitzer archive. Table 4 shows the overlaps between the samples. We note that each sample is incomplete because of the limited availability of data in the Spitzer IRS archive and of X-ray and [O III] measurements in the literature (see Tab. 5). Moreover, maser surveys have not been performed with homogeneous properties (sensitivity, velocity coverage) nor carried out for all sources of our combined sample.

The three samples are based on different selection criteria: Optically selected Seyferts in the CfA sample and IRAS selected sources in the $12\ \mu\text{m}$ and F25/F60 sample. Thus, it is possible that they are affected by different biases with respect to potential maser detection. The fraction of Sy2 masers to non-masers increases from $1/4$ (4/16) in the CfA sample, to $\sim 1/3$ (11/29) in the $12\ \mu\text{m}$ sample and to ~ 1 (6/8) in the IRAS F25/F60 sample. This is consistent with the well-known finding that the mid- and far-infrared wavelengths select more obscured AGN than the optical bands.

However, the range of luminosity ratios ($L_X / L_{[\text{OIV}]}$, $L_{7\ \mu\text{m}} / L_{[\text{OIV}]}$, $L_{[\text{OIII}]} / L_{[\text{OIV}]}$), listed in Table 5, are similar for all three samples. This also indicates that among optical selected masing sources, some can be obscured at a level similar to that of infrared selected sources⁴. To summarize, the result of all three samples (CfA, $12\ \mu\text{m}$, and IRAS F25/F60) are similar in that they point consistently to a prevalence of maser detections in Sy2s with high X-ray obscuration and one may expect that this also holds in general for Seyfert galaxies.

Are our selected Sy2 masers representative of all 52 known Sy2 masers (Zhang et al., 2010)? To address this question, we compare our in-sample Sy2 masers with all remaining 37 off-sample Sy2 masers.

In Figure 51, we compare X-ray and [O IV] luminosities between in- and off-sample masers. The comparison refers to those masers with X-ray and [O IV] fluxes available, i.e. 12 off-sample Sy2s, 13 in-sample Sy2s, and 3 in-sample Sy1s. Both the in-sample and off-sample roughly populate the same $L_X / L_{[\text{OIV}]}$ range. However, the $L_X / L_{[\text{OIV}]}$ ratio is, on average, about a factor of two higher for the off-sample than the in-sample

⁴ Note that even for infrared-selected AGN, optical criteria influence the sample, because the Seyfert identification is done using optical spectroscopy.

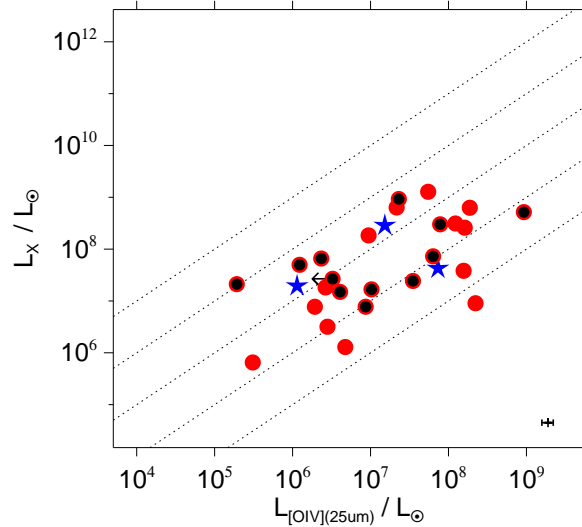


Figure 51: Observed 2-10 keV X-rays plotted against [OIV] line luminosity. Sy1 masers are represented by blue stars and Sy2 masers by red dots. Off-sample Sy2 masers are marked with black dots. The dotted lines mark fixed flux ratios of 1000; 100; 10; 1; 0.1 (from top to bottom). The error bar in the lower right corner is the average error of all [OIV] measurements.

masers. This indicates that the off-sample Sy2 masers may be less absorbed than the in-sample ones. Compared with the in-sample Sy2 non-masers (omitted in Fig 51, see Fig. 44), however, the off-sample masers show, on average, about a factor of two lower $L_X / L_{[\text{OIV}]}$, hence still a considerably high obscuration.

Some off-sample masers exhibit spurious flux ratios indicative of no obscuration (i.e. $L_X / L_{[\text{OIV}]} > 10$ for 4 objects). Among them, we find two nearby extended sources, NGC4258 and NGC4945, in which the X-ray emission was associated with star formation by Risaliti (2002) and Strickland et al. (2004).

To summarize, the large overlap and the lack of significant differences between in- and off-sample Sy2 masers indicates that the results for our combined sample of Sy2 masers can be extended to all known Sy2 masers.

We note that the inhomogeneous selection of all off-sample masers and non-masers precludes any meaningful comparison of maser to non-maser statistics with our in-sample data. A KS test shows a probability of 63% that subsets of both, off- and in-sample masers, are drawn from the same parent distribution and the above-mentioned difference in $L_X / L_{[\text{OIV}]}$ is only by chance. However, a KS test between the in-sample non-masers and the off-sample masers similarly yields a 60% probability that they are drawn from the same parent distribution. Comparing the $L_X / L_{[\text{OIV}]}$ ratio of the in-sample Sy1 non-masers with those of the off-sample Sy2 masers, shows a probability of 0.16% of their being drawn from the same parent distribution. This indicates that the off-sample Sy2 masers differ significantly from the unobscured Sy1 non-maser.

4.2.5 Maser and AGN luminosity

A search for H₂O masers in 274 high-redshift ($0.3 < z < 0.8$) SDSS type-2 AGN, of which half are type-2 *quasars* (Bennert et al. 2009) found only one maser (SDSSJ0804+3607,

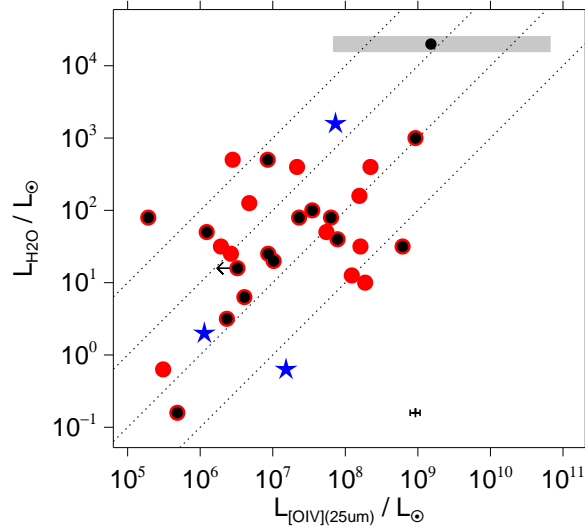


Figure 52: Maser H_2O versus [OIV] luminosity. Symbols and colors are as in Fig. 51. The dotted lines mark fixed ratios 10^{-4} ; 10^{-5} ; 10^{-6} ; 10^{-7} (from top to bottom). For comparison, the expected position of the $z = 0.66$ maser SDSSJ0804+3607 is marked with a black dot and a gray bar covering the range $0.1 \times L_{[\text{OIII}]} < L_{[\text{OIV}]} < 100 \times L_{[\text{OIII}]}$ assumed from Fig. 49.

Barvainis and Antonucci 2005). The high rate of non-detections in these luminous AGN might be due to limited observational sensitivity or intrinsic differences between low- and high-luminosity AGN. These differences could for instance be that in a high-luminosity AGN the accretion disk becomes hotter so that the density required for maser emission falls below a critical limit. If this were frequently the case, one would expect a relative decline in H_2O maser luminosity with increasing AGN luminosity. On the other hand, the SDSS H_2O maser survey was relatively shallow, because one was interested in finding masers that are sufficiently bright for spatially resolved follow-up VLBI observations.

We consider how far the Seyfert sample can help us to distinguish between these two possibilities (i.e. by investigating whether or not $L_{\text{H}_2\text{O}} / L_{[\text{OIV}]}$ declines with increasing $L_{[\text{OIV}]}$). A remarkable feature of Fig. 44 is that maser-detections and non-detections are quite evenly distributed across the whole [OIV] luminosity range covering about four orders of magnitude. Thus, our data do not indicate a trend where the frequency of non-masers increases with luminosity. Also we have already seen that the available maser observations of the Seyferts are biased against maser detection in faint (and distant) AGN (Fig. 47).

Figure 52 shows the (isotropically assumed) maser luminosity versus the AGN luminosity traced by [OIV]. In addition to the Seyfert sample, we have plotted the expected position of SDSSJ0804+3607 at $z = 0.66$, the only QSO-2 maser detection. Because this source had not been observed with Spitzer IRS, we derived $L_{[\text{OIV}]}$ from $L_{[\text{OIII}]}$ using the range $0.1 \times L_{[\text{OIII}]} < L_{[\text{OIV}]} < 100 \times L_{[\text{OIII}]}$ as indicated in Fig. 49, which is also valid for higher luminosity AGN (Haas et al. 2005). At a given [OIV] luminosity, the maser luminosity spreads over three orders of magnitude (Fig. 52). One explanation for the large spread is that the maser emission is not isotropic, and hence the derived maser luminosity depends sensitively on the maser direction with respect to the line-of-sight. The Seyfert sample alone indicates only a marginal corre-

lation in Fig. 52, with a Pearson correlation coefficient of 0.32 for all Sy2 masers of our combined sample that is not significant at the 5% level. Adding the off-sample Sy2 masers changes the coefficient to 0.46 which would then be significant, but this correlation might also be an artifact of distance in the luminosities. However, in addition, the position of SDSSJ0804+3607 and that its assumed $\text{H}_2\text{O} / [\text{OIV}]$ ratio lies in the same range as for the lower luminosity AGN, argues in favor of a physical connection between maser luminosity and AGN luminosity.

The numerous non-masers among the SDSS QSO-2s (Bennert et al., 2009) have a $[\text{OIII}]$ luminosity similar to that of SDSSJ0804+3607, hence are expected to populate a similar $L_{[\text{OIV}]}$ range in Fig. 52. The H_2O maser upper limits⁵, found for these QSO-2s by Bennert et al. (2009), lie even above J0804+3607. Thus, the upper limits are not stringent enough to support a relative decline of maser luminosity with increasing AGN luminosity. This, together with the sufficiently high $L_{\text{H}_2\text{O}} / L_{[\text{OIV}]}$ ratio of J0804+3607, leads us to conclude that the main reason for the high rate of maser non-detections is insufficient observational sensitivity, rather than basic differences between low-and high-luminosity AGN for hosting a maser.

4.3 CONCLUSION

To understand the connection between H_2O maser detection rate and nuclear extinction, we have used the $[\text{OIV}]_{25.9 \mu\text{m}}$ line and the $7 \mu\text{m}$ continuum flux from Spitzer spectra of a well-selected sample of 114 Seyfert galaxies from the CfA, $12 \mu\text{m}$, and IRAS F25/F60 catalogs, for which a maser search has been performed. These data have been compared to hard X-ray and $[\text{OIII}] 5007\text{\AA}$ fluxes from the literature. We have analyzed the data in the framework of the orientation-dependent AGN unified scheme, yielding the following results:

1. Comparing hard X-rays to $[\text{OIV}]$ flux, Sy2s exhibit, on average, an about ten times lower X-ray to $[\text{OIV}]$ ratio than Sy1s. Masers reside primarily in X-ray absorbed sources (i. e. those with low $L_X / L_{[\text{OIV}]}$ ratios). Sy2 masers have on average about four times less X-ray flux normalized by $[\text{OIV}]$ than non-maser Sy2s. This is consistent with the geometric alignment of both the X-ray absorber and the maser emitting region in the accretion disk. Non-masers do not tend to reside predominantly in strongly absorbed sources. However, our data uncover an observational bias against faint sources, in the sense that more sensitive maser observations might reveal more absorbed sources to house a maser.
2. For the $7 \mu\text{m}$ to $[\text{OIV}]$ flux ratio, we have found that most Sy2s are spread across the same range as Sy1s. However, some sources have a significantly lower ratio, pushing the Sy2s on average to about three times lower ratios than Sy1s. These cases can be explained by an extended dusty absorber covering the $7 \mu\text{m}$ emitting torus region. Maser detections also appear to correspond to $7 \mu\text{m}$ absorbed sources, but with less significance than in the X-ray to $[\text{OIV}]$ comparison. This suggests that the geometric alignment of the MIR absorber with the maser emitting disk is not as perfect as the supposed alignment of the disk with the X-ray absorber.
3. The $[\text{OIII}]$ to $[\text{OIV}]$ flux ratio also indicates the presence of extended obscuration in some Sy2s that blocks the optical emission from the NLR. Masers and non-

⁵ $\frac{L_{\text{H}_2\text{O}}}{L_\odot} = 0.0039 \times \frac{1}{1+z} \times \left(\frac{D_L}{\text{Mpc}} \right)^2$

masers are distributed very similarly in the [O III] to [O IV] plot. The fraction of maser-detections is not significantly higher for sources with this extended absorption. This leads us to conclude that the matter distribution for the [O III] absorber has no influence on the prediction of a maser detection. Moreover, it is possible that a substantial fraction of the absorption of AGN emission could occur in extended regions outside the torus that are not necessarily aligned with the torus or AGN sub-structure.

4. The separate three samples, CfA, $12\mu\text{m}$, and IRAS F25/F60 provide very similar results. The Sy2 maser to non-maser ratio increases from optical to infrared selection. The Sy2 masers of our combined sample have a similar range of $L_{[\text{O IV}]}$ and $L_{\text{H}_2\text{O}}$ as the known off-sample Sy2 masers. While, on average, the off-sample masers are a factor of two less obscured, as inferred by the $L_X / L_{[\text{O IV}]}$ ratio, they are still considerably obscured compared to Sy1s from our combined sample. Thus, the results obtained for our combined sample of Sy2 masers may also hold for all remaining Sy2 maser sources that have no Spitzer or X-ray data available.
5. After supplementing our combined sample with the remaining known Sy2 masers that were not included in it, the H_2O maser luminosity appears to be correlated with the AGN luminosity traced by [O IV], although it has a large spread. We do not find any evidence of physical differences between low- and high-luminosity AGN hosting a maser.

With the novel concept of using the MIR [O IV] as tracer of the AGN luminosity, the results demonstrate that heavy X-ray absorption is an indicator of a high probability of detecting a maser. The $7\mu\text{m}$ absorption can also be used to find maser candidates, but with a lower probability.

SUMMARY AND OUTLOOK

This thesis has studied different components of the central regions of AGN. The principal elements can be summarized as follows.

- H₂O water megamasers at 22 GHz may offer superior precision in the distance measurements for type 2 AGN, since they allow a direct geometric method. However, usable candidates are very rare and surveys at radio telescopes require enormous amounts of integration time. Therefore, I developed a new principle to find good candidates. By comparing Mid-IR observations with X-ray fluxes, it can be shown that X-ray absorbed sources are more likely to present a maser emission in the line-of-sight to the observer. This allows further investigators to focus their integration time on these sources.
- The reverberation mapping technique measures nuclear continuum brightness variations and their emission line echo in the BLR. If the accuracy of the relation between BLR size and nuclear luminosity can be improved drastically, it becomes possible to estimate the AGN distance. With our new method of photometric reverberation mapping, four AGN (ESO 374-G25, PG0003+199, Ark120 and 3C120) could be placed anew in the $R_{\text{BLR}} - L$ diagram. The dense time sampling of our lightcurves allows us to obtain precise BLR sizes. Using the flux variation gradient method we are able to calculate the host-free AGN luminosity L_{AGN} . This method is a powerful alternative to taking high-resolution HST images and applying host model fits. Only one single-epoch spectrum was obtained to successfully estimate further properties, like the Balmer line's velocity dispersion and the enclosed virial black hole masses. Future comparisons will show how reliable such M_{BH} determinations are.
- To expand the ability of the Universitätssternwarte der Ruhr-Universität Bochum, to obtain long-term variability lightcurves with high sampling rates, I have worked out and implemented a new control system for the *VYSOS 16* telescope. It is now capable to perform robotic observations and has already provided the first lightcurves. Finally, this will contribute to the future investigations as detailed above.

With respect to maser detection campaigns, first investigations are already in progress, considering the candidate selection criterion we proposed here. The current quality of the imaging data of *VYSOS 16* is amazing. In combination with the methodical success of the photometric reverberation mapping, the next three years allow us to monitor at least 50 AGN and to determine their R_{BLR} and L_{AGN} .

APPENDIX

At first, this appendix contains a brief description of the *VYSOS 16* telescope's hardware and script design, as well as commands of the control script. This is followed by an introduction to the mathematical background of the analysis methods as used in this thesis. Then, a set of Tables is presented, showing the sample properties together with our results. Finally, a supplemental list of figures is attached, on which part of my discussion refers to.

A.1 HARDWARE

MOUNT: The telescope has an equatorial fork mount manufactured by *Equinox Inter-science*. Both, right ascension (α) and declination (δ) drives have contact to them through friction wheels. The polar axle unit is a weldment assembly that uses an 20.32 cm diameter stainless steel tube of 1.27 cm wall thickness that is mated to a 60.96 cm diameter drive wheel on the north end. The south end has a plug plate that carries a stub axle of 7.46 cm diameter. The polar axis is defined in space by 2 pinions of 1.905 cm diameter on the north end and by a spherical journal cartridge bearing on the south end. The support pinions on the north end absorb the radial load imposed by the fork and tube units, along with about 80 percent of the moment load created by the cantilevered fork/tube assembly. The remainder of the moment load is absorbed by the south bearing, which is a spherical journal, self aligning unit. This bearing also accommodates the entire thrust load imposed by the polar axis, fork and tube assemblies.

POSITIONING: Movement is driven by bifilar stepper motors (1 per axis). Positional feedback is received from two shaft encoders on both α and δ axes. The cabin shutter position is also readable. Per equatorial axis, one low-resolution absolute encoder is available for absolute alignment of the axis in case of a power outage. Then, each axis has a relative encoder with high rotation ratios on the axis (α : 32/1 and δ : 24/1). They have significantly higher accuracy than the absolute encoders, but trade this advantage for reoccurring periodic errors (see Fig. 5). The absolute encoders are attached to the NI-6509 DAQ card in *vysos-s*. They feature an fourteen bit digital input giving out Gray-code¹. The converted binary numbers (0-16384) projected to the angles on the axis.

OPTICS: The *VYSOS 16* features a Coudé system with a focal length of 2337 mm and an aperture of 413 mm. It also uses two elliptical diagonal mirrors and a refractive *Paracorr* coma corrector by *Televue Optics*. The system obscuration is 37%. All mirrors in the system are supported by mounting plates with axial and radial support pads. The mirror cells use a center ball pivot system with four pull

¹ Gray-code reduces the Hamming distance in the counting number system to 1. This means that always only one bit will change when increasing, or decreasing the counter. This allows precise encoders on slowly varying inputs, having no false intermediate states when multiple bits are switching in an unknown order.

screws acting through reaction plates. An adjustment in either the horizontal or vertical axis is made by tightening a screw and loosening the opposite screw.

FILTERS: The internal filter wheel holds 5 slots and is currently equipped with Johnson B and V broad band filters from *Astrodon* and three *Ashahi* filters with 12 nm band-pass. These are YBPA670, YBPA680, YBPA690, centered at 670 nm, 680 nm and 690 nm.

CCD: SBIG STL-6303 with 3072×2048 pixel that have an approximate edge length of 9 microns. The pixel scale is thus $0''.79$ per pixel and the resulting field of view $41.2' \times 27.5'$.

A.2 SOFTWARE

The software was developed and tested in a *Scientific Linux 5.0* x64 environment. The telescope server can be accessed via *UDP* and is compatible to the *Alma Common Software (ACS)* system. The communication between the telescope server and *ACS* is based on the *ACE* network interface library. Figure 53 (Appendix) illustrates the structure.

We have developed hardware drivers (*ni73xx* 0.6.3.1, based on the work by Kogee Leung²) using the programming language *C*. In these low level drivers the communication to the *National Instruments 7344* PCI controller card is abstracted. I.e. a command to set up a parameter for an axis will be formed into a packet as depicted in Fig. 54 in the Appendix.

The commands used in the hardware drivers have then been combined to more complex sequences of commands in our newly developed *libfreemotion* 1.0.1 library (also based on the work by Kogee Leung). It offers a variety of command functions (i.e. to block axes, set up target positions or initiate movements).

The *libfreemotion* is then used by the telescope server class, which we have developed. Here the abstraction layer is even higher, and the telescope server software class offers functions like initiate tracking on given equatorial coordinates. For this to be possible, corrections of aberration, precession, nutation, atmospheric refraction, misalignment of the mount, bending of mount and tube, and the periodic errors in the positioning have to be corrected in-place to sub-arcsecond precision.

A.3 VYSOS16 SCRIPT COMMANDS

waituntil:dusk

At this point, the telescope will wait for the evening astronomical twilight to pass, before any new jobs are processed.

waituntil:dawn

At this point, the telescope will wait for the morning astronomical twilight to pass, before any new jobs are processed.

² <http://ni73xx.sourceforge.net/>

name:<objectname>

Through this command, the following images will be designated with the characters in place of <objectname> in their header keyword OBJECT.

ra:<HH/MM/SS.S>

By this command, the following images will be dithered around this right ascension. Capital letters represent time angles. Header keyword OBJCTRA will be written.

dec:<ddd/mm/ss>

With this command, the following images will be dithered around this declination. Small letters represent arc angles. Header keyword OBJCTDEC will be written.

filter/exptime/amount:<filtername/exptime/amount>

This is basically an exposure-command. The script will generate <amount> number of observations dithered around the coordinates defined before. Header keywords FILTER and EXPTIME will be written. However, some modes, explained below require different compositions of this command, which is explained in each section respectively. Available filters are:

v_j: Johnson V-band.

B_j: Johnson B-band.

670: Narrow band filter with 12nm FWHM at 670nm.

680: Narrow band filter with 12nm FWHM at 680nm.

690: Narrow band filter with 12nm FWHM at 690nm.

MOUNT:OFF

This command will close the tube and drive the mount into the parking position. Afterwards the observer may shutdown the motors and close the roof.

END

If this job is started, the connection to the *mount* and *ccd* containers of ACS will be suspended. Afterwards the script will close.

POINT

This will enable the pointing measurement mode. All following observations only need a format like

"filter/exptime/amount:V_j/60/1"

without a name declaration beforehand. The script will automatically generate a number of random positions across the visible sky above 45° altitude starting roughly in

zenit. If only one measurement is taken, it will be used to calculate an offset of the pointing model from the true sky, adding this to the relative encoder counts. This is to mitigate long-term drifting of the pointing model.

BIAS

This will enable the bias imaging mode. All following observations only need a format like "amount:10".

DARK

This will enable the dark imaging mode. All following observations only need a format like "amount/exptime:10/120".

FLAT

This will enable the flatfield imaging mode. All following observations only need a format like "filter/amount:670/10". The script will automatically generate flatfield positions on the sky at -24.5° declination and 20° from the meridian, away from the sun, in hour angle coordinates. Hence, at dusk it will look east and at dawn it will look west automatically.

LIGHT

This will enable the science imaging mode. Now, a good focus will be checked before the first observation and later if one hour has passed since last focussing, or the object has changed. After switching to this mode, in order to observe an object, you need to define the name, α and δ before the exposure commands appear. This exposure command should then be like "filter/exptime/amount:V_j/60/1".

A.4 EXAMPLE OF A COMPLETE OBSERVATION PLAN

Here we present a short plan, designed in the fashion of our regular observations. The Script will begin with automatic adjustments to take the requested flatfields during dusk.

```

FLAT
filter/amount:690/5
filter/amount:670/5
filter/amount:680/5
filter/amount:V_j/5
filter/amount:B_j/5
BIAS
amount:5
DARK
exptime/amount:120/5
waituntil:dusk
POINT
filter/exptime/amount:V_j/60/1
LIGHT
name:MARK705
ra:09/26/03.3
dec:+12/44/03
filter/exptime/amount:V_j/60/9
filter/exptime/amount:B_j/60/9
filter/exptime/amount:680/120/14
filter/exptime/amount:690/120/14
waituntil:dawn
FLAT
filter/amount:B_j/5
filter/amount:V_j/5
filter/amount:680/5
filter/amount:670/5
filter/amount:690/5
MOUNT:OFF
BIAS
amount:5
DARK
exptime/amount:120/5
END

```

If the script was started too late (e.g. because of strong wind), the script will notice this condition and quickly skip those flatfields, for which there is not enough brightness. Then we take a set of bias and dark exposures, before taking a pointing verification exposure (that is matched in-place with an astrometric catalog). Then the telescope is used to observe Markarian 705 for four filters with different repetitions and exposure-times. If this object is done, the telescope will wait till dawn, before it starts to read out the CCD for flats. When everything is done, the telescope will park and seal the optics, so the roof can be closed safely.

A.5 MATHEMATICAL METHODS

A.5.1 *The Discrete Cross Correlation Function*

We assume that the broad emission line $B(t)$ flux is a reprocessed signal of the variable continuum $C(t)$. This processing can be described by:

$$B(t) = \int C(t - \tau)\psi(\tau)d\tau \quad (6)$$

$\psi(\tau)$ is the so-called transfer function. It is determined by the radiation field of the nucleus and the morphology and distance of the emitting clouds. Our task is now to extract the average distance (from the reverberation time lag) of the cloud structure.

One could try to transform $B(t)$ into Fourier space and apply the convolution theorem, as proposed by Blandford and McKee (1982), but this would require a very fine resolved and equidistant time sampling, which is observationally impossible to achieve, even in an environment like Chile's Atacama desert. But there exists just another method that measures the correlation of the obtained lightcurves for different lagtimes. This is the Discrete Correlation Function (DCF), introduced by Edelson and Krolik (1988). Here, we calculate this function using a particular binsize for a discrete range of time lags defined by $n \cdot \Delta\tau \leq \tau_{ij} < (n + 1) \cdot \Delta\tau$. With two data arrays of fluxes (associated to their individual observation times) b_i and c_j this function is described by:

$$\text{DCF}(\tau_{ij}) = \frac{1}{M} \sum_{ij} \frac{(b_i - \bar{b})(c_j - \bar{c})}{\sigma_b \sigma_c} \quad (7)$$

The sum is over all pairs of datapoints b_i and c_j with their associated time lags $\tau_{ij} = t_i - t_j$ inside the lagtime bin $2 \cdot \Delta\tau$ defined above. The data is normalized by the product of the standard deviations σ_b , σ_c and M , which is the total of pairs in the bin. In our analysis in Section 3.5.1, we will plot this function for a set of lagtime bins which are adapted to the median time sampling of the supplied lightcurves. As Blandford and McKee (1982) already noted, varying the binsize has only little impact to the result if chosen with a size in this order.

A.5.2 The Flux Variation Gradient

Choloniewski (1981) noticed a linear relationship between the fluxes obtained in two different filters taken at different epochs. Using this relationship he demonstrated the existence of two component structure to the spectra of Seyfert galaxies. Following the geometrical representation of three-dimensional vectors by Choloniewski (1981), it is possible to write the two component structure in two different filters (i, j) as:

$$\vec{\phi}_{i,j}(v, t) = \vec{F}_{i,j}(v) + \vec{f}_{i,j}(v, t) \quad (8)$$

where the observed flux $\vec{F}_{i,j}(v)$ and $\vec{f}_{i,j}(v, t)$ are the constant and variable components in two arbitrary filters respectively. The shape of spectrum of the variable component does not change, allowing us to express their ratio by a constant a_{ij} :

$$\frac{\vec{f}_j(v, t)}{\vec{f}_i(v, t)} = a_{ji} \quad (9)$$

where a_{ji} is a constant. Using equations (8) and (9) we obtain the equation of a straight line in the plane ($\vec{\phi}_i, \vec{\phi}_j$):

$$\vec{\phi}_j(v, t) = a_{ji} \vec{\phi}_i(v, t) + b_{ji}, \quad b_{ji} = \vec{F}_j(v) - a_{ji} \vec{F}_i(v) \quad (10)$$

The coefficient a_{ji} represents the color index of the variable component and can be obtained by fitting a linear gradient in the flux-flux diagram.

This component is tracing the variability of the nucleus. This was proposed by Winkler et al. (1992) in the first place, in order to obtain the nucleus's colors for a set of

35 AGN monitored in *UBVRI*. Although this has been firmly established and verified by numerous authors like Yoshii et al. (2003), Suganuma et al. (2006), Doroshenko et al. (2008) and Sakata et al. (2010), there remain some doubts, as mentioned in Sakata et al. (2010), where the measurements were scattering more than the linear relationship should allow if the color stays perfectly constant.

A recent study on the determination of the nuclear flux contribution was realized by Sakata et al. (2010). In this study the flux of the host galaxy was estimated for 11 nearby Seyfert galaxies and QSOs. These fluxes were measured in *B*, *V* and *I* bands, using surface brightness fitting to the high resolution HST and MAGNUM telescope images. The authors find a well defined range for the host galaxy slope of $0.4 < \Gamma_{BV}^{host} < 0.53$, which corresponds to host galaxy colors of $0.8 < B - V < 1.1$. The results obtained by Sakata et al. (2010) are consistent (within measurement errors) with those obtained by Winkler (1997), Bentz et al. (2006) and Bentz et al. (2009a).

A.6 TABLES

In this section we list the most important Tables. The vast amounts of photometric and spectroscopic measurements are omitted. They are intended to be accessible online via the web page of the AIRUB. Currently, you are invited to request any data from the author³ of this work.

Table 2: Filters on the *VYSOS 6* and *VYSOS 16* telescopes. The index ‘J’ represents filters of the Johnson photometric system and ‘S’ represents filters from the Sloan system. ‘NB’ is a narrow band continuum filter. The numbers of the three narrow *VYSOS 16* filters correspond to the central wavelength in nanometers. The FWHM of each narrow filter is 12 nm. The “white” filter in *BEST II* is simply an empty slot, leaving the CCD’s quantum efficiency profile.

| Telescope | Filternames | | | | | | |
|------------------|----------------------|----------------------|----------------------|----------------------|----------------------|-----------------------------|-------------|
| <i>VYSOS 6 a</i> | <i>U_J</i> | <i>V_J</i> | <i>R_J</i> | <i>g_S</i> | <i>i_S</i> | <i>Hα</i> | <i>SII</i> |
| <i>VYSOS 6 b</i> | <i>B_J</i> | <i>I_J</i> | <i>u_S</i> | <i>r_S</i> | <i>z_S</i> | <i>NB</i> | <i>OIII</i> |
| <i>VYSOS 16</i> | <i>B_J</i> | <i>V_J</i> | 670 | 680 | 690 | | |
| <i>BEST II</i> | <i>B_J</i> | <i>V_J</i> | <i>R_J</i> | <i>I_J</i> | white | | |

³ Michael Ramolla: ramolla@astro.rub.de

Table 3: Results of the DCF analysis of the obtained lightcurves, as noted in Table 1, combined with the cleaned AGN luminosity, obtained by applying the FVG method. The values for ESO 374-G25 are associated to the second epoch in 2012, because the first one in 2011 lacked V band observations and spectroscopy.

| Name | Γ_{BV} | $L_{\text{AGN}} \lambda 5100 \text{ \AA}$ ($10^{42} \text{ erg s}^{-1}$) | $\tau_{\text{H}\alpha}$ | $\tau_{\text{H}\beta}$ | $M_{\text{virial}}^{(3)}$ ($10^6 M_{\odot}$) |
|-------------|-----------------|---|-------------------------|------------------------|---|
| | | | (days) | | |
| 3C120 | 1.12 ± 0.04 | 69.4 ± 7.1 | – | 23.6 ± 1.7 | 10.4 ± 5.3 |
| Ark120 | 1.20 ± 0.10 | 132.7 ± 12.1 | – | 46.5 ± 3.3 | 35 ± 17 |
| ESO 374-G25 | 1.33 ± 0.22 | 1.85 ± 0.93 | 11.1 ± 2.6 | – | 10.4 ± 5.7 |
| PG0003+199 | 1.16 ± 0.05 | 31.3 ± 3.6 | $20.0^{+2.0}_{-2.7}$ | – | 3.0 ± 1.5 |

Table 4: Documentation of how far the three samples (of 163 sources in total) match and complement each other. For each row, the table entries list the number of sources contained in the intersection of the sample denoted by the Cols. 2-7 with the CfA, $12\mu\text{m}$, and IRAS F25/F60 sample (Col. 1). For instance the union of the $12\mu\text{m}$ and IRAS F25/F60 samples (Col. 5) has 45 sources in common with the CfA sample (Row 1).

| | (1) | (2) | (3) | (4) | (5) | (6) | (7) |
|---------------------|-----|-----------------|------|----------------------------------|-----------------|--------------------------|-----|
| Intersecting sample | CfA | $12\mu\text{m}$ | IRAS | $12\mu\text{m} \cup \text{IRAS}$ | CfA \cup IRAS | CfA $\cup 12\mu\text{m}$ | |
| CfA | 54 | 42 | 12 | 45 | – | – | |
| $12\mu\text{m}$ | – | 118 | 24 | – | 57 | – | |
| IRAS F25/F60 | – | – | 60 | – | – | 27 | |

Table 5: The average values and standard deviations of the logarithmic luminosity ratios for each subset of Seyfert galaxies. Column 1: In descending order, the optically selected CfA sources (Huchra and Burg, 1992), the MIR-selected $12\mu\text{m}$ sources (Rush and Malkan, 1993), the IRAS F25/F60 flux-ratio selected sources (Schmitt et al., 2003) and the combined sample that is used in this work. Columns 2-4: Number of sources with luminosities available in [OIV] and one of the following: 2-10 keV X-rays (Col. 2) or $7\mu\text{m}$ (Col. 3) or [OIII] (Col. 4). Each sample's row is subdivided into Sy1 maser, non-maser, maser-unknown and Sy2 maser, non-maser, and maser-unknown. Column 5: Total number of objects in the parent sample from Col. 1, e.g. 3 Sy1 maser in the CfA, 18 Sy1 non-maser in the CfA, and so forth.

| (1) | | (2) | | (3) | | (4) | | (5) |
|---|---------------|--------------------------|-----------------|---------------------------------------|---------------|--|----------------|---------------|
| Parent Sample | Subset | $L_X / L_{[\text{OIV}]}$ | | $L_{7\mu\text{m}} / L_{[\text{OIV}]}$ | | $L_{[\text{OIII}]} / L_{[\text{OIV}]}$ | | Parent Sample |
| | | Number | log(Ratio) | Number | log(Ratio) | Number | log(Ratio) | Number |
| CfA | Sy1 maser | 3 | 0.8 ± 0.9 | 3 | 1.6 ± 0.1 | 3 | 0.0 ± 0.6 | 3 |
| | Sy1 non-maser | 16 | 2.0 ± 0.5 | 14 | 1.9 ± 0.5 | 16 | 0.1 ± 0.4 | 18 |
| | Sy1 unknown | 2 | 1.73 ± 0.02 | 3 | 2.1 ± 0.6 | 2 | -0.1 ± 0.1 | 4 |
| | Sy2 maser | 4 | 0.1 ± 0.5 | 4 | 1.2 ± 0.7 | 4 | -0.2 ± 0.6 | 4 |
| | Sy2 non-maser | 16 | 1.1 ± 0.9 | 18 | 1.3 ± 0.5 | 20 | -0.2 ± 0.5 | 24 |
| | Sy2 unknown | 0 | – | 1 | 1.4 | 1 | –1.3 | 1 |
| $12\mu\text{m}$ | Sy1 maser | 2 | 1.25 ± 0.93 | 2 | 1.6 ± 0.1 | 2 | 0.4 ± 0.5 | 2 |
| | Sy1 non-maser | 22 | 2.0 ± 0.6 | 22 | 1.8 ± 0.5 | 27 | 0.1 ± 0.4 | 30 |
| | Sy1 unknown | 4 | 2.3 ± 0.6 | 5 | 1.9 ± 0.6 | 6 | 0.0 ± 0.3 | 9 |
| | Sy2 maser | 11 | 0.5 ± 0.7 | 10 | 1.2 ± 0.6 | 11 | -0.3 ± 0.5 | 13 |
| | Sy2 non-maser | 29 | 0.9 ± 1.0 | 34 | 1.4 ± 0.5 | 42 | -0.4 ± 0.6 | 51 |
| | Sy2 unknown | 1 | 1.1 | 1 | 1.4 | 2 | -0.7 ± 0.9 | 2 |
| IRAS | Sy1 maser | 0 | – | 0 | – | 0 | – | 0 |
| | Sy1 non-maser | 13 | 2.2 ± 0.4 | 10 | 1.7 ± 0.3 | 15 | 0.0 ± 0.4 | 15 |
| | Sy1 unknown | 0 | – | 0 | – | 0 | – | 0 |
| | Sy2 maser | 8 | 0.2 ± 1.0 | 8 | 1.2 ± 0.7 | 8 | -0.3 ± 0.4 | 8 |
| | Sy2 non-maser | 6 | 0.7 ± 0.8 | 9 | 1.3 ± 0.5 | 10 | -0.2 ± 0.5 | 11 |
| | Sy2 unknown | 0 | – | 0 | – | 0 | – | 0 |
| Combined: CfA \cup $12\mu\text{m}$ \cup IRAS | Sy1 maser | 3 | $.8 \pm 0.9$ | 3 | 1.6 ± 0.1 | 3 | 0.0 ± 0.6 | 3 |
| | Sy1 non-maser | 28 | 2.0 ± 0.6 | 25 | 1.8 ± 0.5 | 33 | 0.1 ± 0.4 | 36 |
| | Sy1 unknown | 5 | 2.1 ± 0.6 | 6 | 1.9 ± 0.5 | 7 | 0.0 ± 0.3 | 10 |
| | Sy2 maser | 13 | 0.4 ± 0.8 | 12 | 1.1 ± 0.6 | 13 | -0.4 ± 0.5 | 15 |
| | Sy2 non-maser | 32 | 0.9 ± 1.0 | 42 | 1.4 ± 0.5 | 50 | -0.3 ± 0.6 | 60 |
| | Sy2 unknown | 1 | 1.1 | 1 | 1.4 | 2 | -0.7 ± 0.9 | 2 |

Table 6: Measured fluxes and literature values. Column 1: Source names with catalog marks: *a*: CfA sample; *b*: 12 μ m sample; *c*: IRAS F25/F60 sample

Column 2: Isotropic maser luminosities obtained from Bennert et al. 2009. A question mark designates sources unobserved for masers and a dash represents a maser undetected source.

Note that MRK938 and NGC1320 are listed as Maser in Zhang et al. (2010) but have no luminosity information available. Therefore, they are marked with asterisks. Column 3: Seyfert type obtained from the NED or the literature with references given in square brackets. Column 4: [OIV] flux determined by Ramolla (2009). Column 5: [OIII] flux from the literature. Column 6: 2-10 keV X-ray flux obtained from the literature. Column 7: 7 μ m continuum flux determined by Ramolla (2009). An analysis of the off-sample masers has also been performed. This data is appended in the table.

References: 1: Dahari and De Robertis 1988; 2: Polletta et al. 1996; 3: Whittle 1992; 4: Gondoin et al. 2002; 5: Moustakas and Kennicutt 2006; 6: Shu et al. 2007; 7: Tran 2003a; 8: de Grijp et al. 1992; 9: Awaki et al. 2000; 10: Reeves and Turner 2000; 11: Ueda et al. 2005; 12: Tran 2003b; 13: Guainazzi et al. 2005; 14: Malizia et al. 2007; 15: Turner and Pounds 1989; 16: Cappi et al. 2006; 17: Iyomoto et al. 1996; 18: Gu et al. 2006; 19: Schmitt et al. 2003; 20: Vaceli et al. 1997; 21: Greenhill et al. 2008; 22: Véron-Cetty and Véron 2006; 23: Risaliti et al. 2000; 24: Bennert et al. 2006; 25: Boroson and Meyers 1992; 26: Verrecchia et al. 2007; 27: Rao et al. 1992; 28: Storchi-Bergmann et al. 1995; 29: Bassani et al. 1999; 30: Kim et al. 1995; 31: Severgnini et al. 2001; 32: Bianchi et al. 2005; 33: Immler et al. 2003; 34: Ho et al. 1995; 35: Terashima et al. 2002; 36: González-Martín et al. 2006; 37: Nandra et al. 2007; 38: Gondoin et al. 2003b; 39: Blustin et al. 2002; 40: Matt et al. 2000; 41: Shang et al. 2007; 42: Perola et al. 2002; 43: Miniutti et al. 2007; 44: Phillips et al. 1983; 45: Holczer et al. 2007; 46: Gondoin et al. 2001; 47: Levenson et al. 2006; 48: Bianchi et al. 2003; 49: Reynolds 1997; 50: Gondoin et al. 2003a; 51: Buchanan et al. 2006; 52: Braitto et al. 2003; 53: Perola et al. 2000; 54: Kewley et al. 2001; 55: Lawson and Turner 1997; 56: Sharples et al. 1984; 57: Ueno et al. 2000; 58: Shinozaki et al. 2006; 59: Ho et al. 1997; 60: Whittle and Wilson 2004; 61: Zhang and Fan 2009; 62: Tilak et al. 2008; 63: Heckman et al. 1980; 64: Done et al. 2003; 65: Oliva et al. 1994; 66: Smith and Wilson 2001; 67: Lumsden and Alexander 2001; 68: Lumsden et al. 2004; 69: Matsumoto et al. 2004; 70: Turner et al. 1997; 71: Panessa et al. 2006.

| (1) | (2) | (3) | (4) | (5) | (6) | (7) |
|--------------------------------|--|-----|---|--|--|-------------|
| Source | H ₂ O $\log\left(\frac{L}{L_{\odot}}\right)$ | Sy | [OIV] $\left(10^{-15} \frac{\text{erg}}{\text{s cm}^2}\right)$ | [OIII] $\left(10^{-15} \frac{\text{erg}}{\text{s cm}^2}\right)$ | 2-10 keV $\left(10^{-14} \frac{\text{erg}}{\text{s cm}^2}\right)$ | 7.6 μ m |
| MRK334 ^[a] | – | 1.8 | 82 ± 14 | 49 ^[1] | 800 ^[2] | 504 ± 101 |
| MRK335 ^[a,b] | – | 1.0 | 67 ± 10 | 950 ^[3] | 960 ^[4] | 983 ± 241 |
| MRK938 ^[b] | * | 2.0 | – | 44 ^[5] | 23 ^[6] | 332 ± 66 |
| E12-G21 ^[b] | ? | 1.0 | 187 ± 56 | 97 ^[7] | – | 366 ± 82 |
| MRK348 ^[b,c] | 2.6 | 2.0 | 163 ± 25 | 359 ^[8] | 482 ^[9] | 1151 ± 235 |
| IZw1 ^[b] | ? | 1.0 | 97 ± 13 | 44 ^[1] | 680 ^[10] | – |
| IRAS00521-7054 ^[b] | – | 2.0 | 71 ± 11 | 77 ^[8] | – | – |
| NGC424 ^[b] | – | 2.0 | 223 ± 34 | 420 ^[3] | 122 ^[11] | 3655 ± 738 |
| NGC526A ^[b] | – | 1.5 | 176 ± 26 | 270 ^[3] | 2046 ^[11] | 669 ± 162 |
| NGC513 ^[b] | – | 2.0 | 59 ± 9 | 35 ^[12] | – | 232 ± 59 |
| F01475-0740 ^[b,c] | – | 2.0 | 62 ± 10 | 53 ^[8] | 82 ^[13] | 393 ± 111 |
| UM146 ^[a] | – | 1.9 | 26 ± 3 | 60 ^[3] | – | < 199 |
| MRK590 ^[c] | – | 1.2 | 31 ± 8 | 53 ^[1] | 1970 ^[14] | < 589 |
| MCG+05-06-036 ^[a,b] | ? | 1.0 | 42 ± 5 | – | – | 166 ± 33 |

Table 6: continued.

| Source | H ₂ O | Sy | [OIV] | [OIII] | 2-10 keV | 7.6 μ m |
|---------------------------------|------------------|-----|------------------|---------------------|----------------------|-------------------|
| NGC931 ^[b,c] | — | 1.5 | 459 \pm 67 | 75 ^[8] | 2000 ^[15] | 1697 \pm 392 |
| NGC1068 ^[a,b,c] | 2.2 | 2.0 | 18908 \pm 2697 | 4834 ^[8] | 462 ^[16] | 52585 \pm 10567 |
| NGC1056 ^[b] | — | 2.0 | < 212 | 23 ^[7] | — | 235 \pm 47 |
| NGC1097 ^[a,b] | — | 1.0 | 52 \pm 12 | 18 ^[7] | 170 ^[17] | 283 \pm 58 |
| NGC1125 ^[b] | — | 2.0 | 356 \pm 52 | 23 ^[18] | — | 118 \pm 27 |
| NGC1144 ^[b] | — | 2.0 | 69 \pm 10 | — | 11000 ^[2] | 164 \pm 37 |
| M-2-8-39 ^[b,c] | — | 2.0 | 144 \pm 21 | 183 ^[8] | — | 270 \pm 69 |
| NGC1194 ^[b,c] | — | 1.0 | 144 \pm 21 | 396 ^[19] | — | 521 \pm 105 |
| NGC1241 ^[b] | — | 2.0 | < 100 | 370 ^[20] | — | — |
| NGC1320 ^[b,c] | * | 2.0 | 254 \pm 37 | 122 ^[8] | 496 ^[21] | 933 \pm 231 |
| NGC1365 ^[b] | — | 1.8 | 1441 \pm 207 | 62 ^[22] | 660 ^[23] | 2759 \pm 553 |
| NGC1386 ^[b,c] | 2.1 | 2.0 | 991 \pm 145 | 800 ^[24] | 27 ^[18] | 1017 \pm 206 |
| IRAS03362-1641 ^[b] | — | 2.0 | 52 \pm 8 | 18 ^[8] | — | — |
| F03450+0055 ^[b] | ? | 1.5 | 31 \pm 5 | 100 ^[25] | — | < 10504 |
| 3C120 ^[a,b] | — | 1.0 | 1195 \pm 174 | 304 ^[8] | 8200 ^[26] | 987 \pm 235 |
| MRK618 ^[b] | — | 1.0 | 96 \pm 16 | 160 ^[8] | 700 ^[27] | — |
| F04385-0828 ^[b] | — | 2.0 | 80 \pm 14 | 3 ^[7] | 1800 ^[2] | 1119 \pm 228 |
| NGC1667 ^[b] | — | 2.0 | 68 \pm 11 | 64 ^[28] | 3 ^[29] | 76 \pm 18 |
| E33-G2 ^[b,c] | — | 2.0 | 137 \pm 20 | 57 ^[19] | — | — |
| M-5-13-17 ^[b,c] | — | 1.5 | 98 \pm 15 | 340 ^[19] | — | 376 \pm 96 |
| IRAS05189-2524 ^[b] | — | 2.0 | 218 \pm 16 | 39 ^[30] | 360 ^[31] | 2247 \pm 451 |
| Markarian3 ^[c] | 1.0 | 2.0 | 1763 \pm 358 | 1070 ^[8] | 590 ^[32] | 1593 \pm 349 |
| MRK6 ^[b,c] | — | 1.5 | 385 \pm 56 | 700 ^[8] | 1200 ^[33] | — |
| MRK9 ^[b] | — | 1.5 | 48 \pm 8 | 109 ^[3] | — | < 1944 |
| MRK79 ^[b,c] | — | 1.2 | 395 \pm 57 | 370 ^[3] | 2600 ^[15] | < 3567 |
| IRAS07598+6508 ^[a,b] | ? | 1.0 | < 168 | — | — | — |
| MRK622 ^[c] | — | 2.0 | 66 \pm 8 | 40 ^[19] | 22 ^[13] | — |
| NGC2639 ^[b] | 1.4 | 1.9 | 36 \pm 4 | 14 ^[34] | 25 ^[35] | < 155 |
| IRAS08572+3915 ^[a,b] | ? | 2.0 | 167 \pm 50 | 8 ^[5] | — | 427 \pm 85 |
| MRK704 ^[b] | — | 1.5 | 117 \pm 18 | 85 ^[1] | 537 ^[11] | < 10595 |
| NGC2841 ^[a] | — | 1.0 | 12 \pm 3 | — | — | 161 \pm 51 |
| pg0923+129 ^[c] | — | 1.2 | 74 \pm 12 | 90 ^[19] | 1151 ^[11] | 458 \pm 96 |
| UGC5101 ^[a] | 3.2 | 1.5 | 82 \pm 11 | 21 ^[5] | 5 ^[36] | 276 \pm 55 |
| NGC2992 ^[a,b] | — | 1.9 | 1300 \pm 134 | 360 ^[1] | 8030 ^[37] | 639 \pm 130 |
| MRK1239 ^[b] | — | 1.5 | 154 \pm 24 | 467 ^[8] | — | 3323 \pm 672 |
| NGC3031 ^[a,b] | — | 1.8 | 44 \pm 13 | 100 ^[34] | 1500 ^[29] | — |
| 3C234 ^[b] | ? | 1.0 | 79 \pm 12 | — | — | 407 \pm 92 |
| NGC3079 ^[a,b] | 2.7 | 2.0 | 290 \pm 53 | 945 ^[5] | 33 ^[16] | 160 \pm 32 |
| NGC3227 ^[a,b] | — | 1.5 | 655 \pm 95 | 820 ^[1] | 750 ^[38] | — |
| NGC3281 ^[c] | — | 2.0 | 1779 \pm 534 | 55 ^[1] | — | 162 \pm 32 |
| NGC3393 ^[c] | 2.6 | 2.0 | 2214 \pm 184 | 268 ^[18] | 9 ^[18] | 199 \pm 52 |
| NGC3511 ^[b] | — | 1.0 | 23 \pm 6 | — | — | 27 \pm 5 |
| NGC3516 ^[a,c] | — | 1.5 | 451 \pm 66 | 270 ^[1] | 4410 ^[18] | < 2900 |
| M+0-29-23 ^[b] | — | 2.0 | 78 \pm 23 | 5 ^[7] | — | 348 \pm 69 |
| NGC3660 ^[b] | — | 2.0 | 25 \pm 5 | 33 ^[28] | — | < 234 |
| NGC3783 ^[a,c] | — | 1.0 | 378 \pm 57 | 763 ^[8] | 8500 ^[39] | 2261 \pm 470 |
| NGC3786 ^[a] | — | 1.8 | 129 \pm 19 | 84 ^[3] | — | 281 \pm 56 |
| NGC3982 ^[a,b] | — | 2.0 | 89 \pm 15 | 188 ^[34] | 22 ^[11] | 49 \pm 10 |

Table 6: continued.

| Source | H ₂ O | Sy | [OIV] | [OIII] | 2-10 keV | 7.6 μ m |
|---------------------------------|------------------|-----|----------------|-----------------------|-----------------------|-----------------|
| NGC4051 ^[a,b] | 0.3 | 1.5 | 366 \pm 53 | 390 ^[34] | 627 ^[16] | 1704 \pm 344 |
| UGC7064 ^[a,b] | – | 1.9 | 118 \pm 17 | – | – | 269 \pm 55 |
| NGC4151 ^[a,b] | –0.2 | 1.5 | 2396 \pm 342 | 11600 ^[34] | 4510 ^[16] | 7211 \pm 1459 |
| MRK766 ^[a,b,c] | – | 1.0 | 474 \pm 69 | 453 ^[8] | 3000 ^[40] | 1061 \pm 213 |
| NGC4388 ^[a,b,c] | 1.1 | 2.0 | 2996 \pm 644 | 564 ^[8] | 762 ^[16] | 971 \pm 199 |
| 3C273 ^[b] | ? | 1.0 | 79 \pm 9 | 116 ^[41] | 8300 ^[15] | 2043 \pm 424 |
| NGC4501 ^[a,b] | – | 2.0 | 33 \pm 6 | 34 ^[34] | 11 ^[16] | < 271 |
| NGC4507 ^[a,c] | – | 2.0 | 332 \pm 51 | 828 ^[8] | 2100 ^[29] | 1579 \pm 320 |
| NGC4569 ^[a] | – | 2.0 | 42 \pm 10 | 24 ^[5] | – | 463 \pm 95 |
| NGC4579 ^[a,b] | – | 1.9 | 30 \pm 5 | – | 440 ^[29] | 325 \pm 74 |
| NGC4593 ^[b,c] | – | 1.0 | 127 \pm 40 | 134 ^[8] | 3710 ^[42] | 1428 \pm 304 |
| NGC4602 ^[b] | – | 1.9 | < 66 | 134 ^[8] | – | 70 \pm 18 |
| TOL1238-364 ^[b] | – | 2.0 | 145 \pm 23 | 194 ^[18] | 17 ^[11] | 779 \pm 161 |
| M-2-33-34 ^[b] | – | 1.0 | 670 \pm 145 | 364 ^[8] | – | 175 \pm 57 |
| MRK231 ^[b] | – | 1.0 | 233 \pm 70 | 230 ^[1] | 68 ^[11] | 5960 \pm 1192 |
| NGC4826 ^[a] | – | 2.0 | 139 \pm 41 | – | – | 540 \pm 108 |
| NGC4922 ^[b] | 2.3 | 2.0 | – | 64 ^[5] | – | 476 \pm 96 |
| NGC4941 ^[b] | – | 2.0 | 285 \pm 43 | 143 ^[18] | 82 ^[11] | < 513 |
| NGC4968 ^[b,c] | – | 2.0 | 307 \pm 45 | 177 ^[8] | 15 ^[13] | 742 \pm 156 |
| NGC5005 ^[a,b] | – | 2.0 | 179 \pm 21 | 7 ^[1] | – | 344 \pm 69 |
| NGC5033 ^[a,b] | – | 1.8 | 109 \pm 23 | 53 ^[1] | 550 ^[29] | 211 \pm 43 |
| MCG-03-34-064 ^[a,b] | – | 1.8 | 1062 \pm 153 | 1507 ^[8] | 210 ^[43] | 2206 \pm 442 |
| NGC5135 ^[b] | – | 2.0 | 726 \pm 147 | 219 ^[44] | – | 808 \pm 161 |
| NGC5194 ^[b] | –0.2 | 2.0 | 227 \pm 47 | 120 ^[34] | 48 ^[16] | 199 \pm 46 |
| M-6-30-15 ^[b,c] | – | 1.2 | 227 \pm 34 | 75 ^[19] | 4220 ^[37] | 1425 \pm 313 |
| IRAS13349+2438 ^[a,b] | ? | 1.0 | 64 \pm 9 | 47 ^[7] | 360 ^[45] | 3194 \pm 673 |
| MRK266 ^[b] | 1.5 | 2.0 | 349 \pm 77 | 23 ^[34] | 56 ^[23] | 72 \pm 14 |
| MRK273 ^[a,b] | – | 2.0 | 474 \pm 142 | 213 ^[5] | 60 ^[29] | – |
| IC4329a ^[a,b] | – | 1.2 | 1061 \pm 156 | 340 ^[12] | 16400 ^[46] | 4140 \pm 968 |
| NGC5347 ^[a,b,c] | 1.5 | 2.0 | 54 \pm 9 | 45 ^[8] | 22 ^[47] | 628 \pm 129 |
| MRK463E ^[a,b] | – | 2.0 | 639 \pm 96 | 563 ^[1] | 40 ^[29] | 2295 \pm 461 |
| NGC5506 ^[b] | 1.7 | 1.9 | 2492 \pm 360 | 521 ^[28] | 5800 ^[48] | 4222 \pm 844 |
| NGC5548 ^[a,b,c] | – | 1.5 | 141 \pm 24 | 360 ^[8] | 4300 ^[49] | 726 \pm 174 |
| MRK817 ^[a,b] | – | 1.5 | 73 \pm 12 | 140 ^[1] | – | 950 \pm 244 |
| PG1501+106 ^[a] | – | 1.5 | 246 \pm 36 | 250 ^[1] | 1869 ^[11] | – |
| NGC5929 ^[a,b] | – | 2.0 | < 114 | 93 ^[1] | 197 ^[11] | 32 \pm 8 |
| NGC5953 ^[b] | – | 2.0 | 172 \pm 25 | 63 ^[3] | – | 259 \pm 52 |
| M-2-40-4 ^[b] | – | 2.0 | 115 \pm 19 | 74 ^[12] | 2693 ^[11] | 1586 \pm 382 |
| F15480-0344 ^[b] | – | 2.0 | 364 \pm 53 | 138 ^[8] | 37 ^[13] | < 838 |
| ESO141-G055 ^[b] | ? | 1.0 | 107 \pm 16 | 164 ^[8] | 2650 ^[50] | – |
| IRAS19254-7245 ^[a,b] | – | 2.0 | 105 \pm 31 | 602 ^[51] | 20 ^[52] | < 323 |
| NGC6810 ^[b] | – | 2.0 | 68 \pm 13 | 13 ^[7] | – | 838 \pm 168 |
| NGC6860 ^[b,c] | – | 1.0 | 122 \pm 18 | 25 ^[19] | 4900 ^[26] | < 2201 |
| NGC6890 ^[b] | – | 2.0 | 90 \pm 13 | 72 ^[18] | 8 ^[11] | 410 \pm 97 |
| MRK509 ^[a,b] | – | 1.2 | 286 \pm 44 | 540 ^[8] | 5660 ^[53] | 1221 \pm 254 |
| UGC11630 ^[c] | – | 2.0 | 175 \pm 28 | – | – | 280 \pm 77 |
| IC5063 ^[a,b,c] | – | 2.0 | 1139 \pm 167 | 564 ^[8] | 1200 ^[29] | 2949 \pm 598 |
| UGC11680 ^[b] | – | 2.0 | 45 \pm 13 | 88 ^[54] | – | < 686 |

Table 6: continued.

| Source | H ₂ O | Sy | [OIV] | [OIII] | 2-10 keV | 7.6 μ m |
|-------------------------------|------------------|-----|----------------|--------------------|----------------------|----------------|
| PG2130+099 ^[a] | ? | 1.0 | 103 \pm 16 | 104 ^[8] | 530 ^[55] | 861 \pm 277 |
| IC5135 ^[b] | – | 2.0 | 300 \pm 40 | 27 ^[30] | 6 ^[36] | 451 \pm 90 |
| NGC7172 ^[b] | – | 2.0 | 384 \pm 39 | 10 ^[56] | 2200 ^[6] | 522 \pm 104 |
| IRAS22017+0319 ^[b] | ? | 2.0 | 287 \pm 42 | 218 ^[8] | 360 ^[57] | – |
| NGC7213 ^[a,b,c] | – | 1.5 | 45 \pm 8 | 130 ^[8] | 3660 ^[14] | 798 \pm 202 |
| 3C445 ^[a,b] | – | 1.0 | 71 \pm 14 | – | 700 ^[58] | 765 \pm 242 |
| NGC7314 ^[a,b] | – | 1.9 | 690 \pm 101 | 61 ^[3] | 3560 ^[29] | 249 \pm 65 |
| UGC12138 ^[a,c] | – | 1.8 | 105 \pm 15 | 144 ^[8] | – | 273 \pm 57 |
| M-3-58-7 ^[b] | – | 2.0 | 117 \pm 19 | 251 ^[7] | – | 1186 \pm 272 |
| NGC7469 ^[a,b] | – | 1.2 | 322 \pm 48 | 840 ^[1] | 2900 ^[49] | 2298 \pm 460 |
| NGC7582 ^[a,b] | – | 2.0 | 2449 \pm 587 | 300 ^[1] | 1550 ^[29] | 309 \pm 61 |
| NGC7590 ^[b] | – | 2.0 | 58 \pm 18 | 11 ^[18] | – | 70 \pm 17 |
| NGC7603 ^[a,b] | – | 1.5 | 24 \pm 4 | 29 ^[1] | 2400 ^[14] | 1619 \pm 339 |
| NGC7674 ^[a,b,c] | – | 2.0 | 448 \pm 110 | 718 ^[8] | 50 ^[29] | 1095 \pm 248 |
| NGC7679 ^[a] | – | 1.0 | 350 \pm 36 | 472 ^[5] | 458 ^[11] | – |
| CGCG381-051 ^[b] | – | 2.0 | < 72 | 5 ^[8] | – | 317 \pm 102 |

Additional off-sample data

| | | | | | | |
|----------------|------|-----|-----------------|---------------------|----------------------|------------------|
| NGC253 | –0.8 | 2.0 | 1519 \pm 239 | – | – | – |
| NGC449 | 1.7 | 2.0 | – | 330 ^[1] | 13 ^[13] | – |
| NGC591 | 1.4 | 2.0 | – | 1780 ^[3] | 18 ^[11] | – |
| NGC613 | 1.3 | 2.0 | – | – | – | – |
| IC184 | 1.4 | 2.0 | – | – | – | – |
| NGC1052 | 2.1 | 2.0 | – | – | 112 ^[36] | – |
| NGC1106 | 0.9 | 2.0 | – | – | – | – |
| MRK1066 | 1.5 | 2.0 | – | 5140 ^[3] | 36 ^[13] | – |
| IRAS03355+0104 | 2.7 | 2.0 | – | 76 ^[8] | – | – |
| IC342 | –2.0 | 2.0 | – | 34 ^[59] | – | – |
| UGC3255 | 1.2 | 2.0 | – | – | – | – |
| VIIZw73 | 2.2 | 2.0 | – | 74 ^[8] | – | – |
| NGC2273 | 0.8 | 2.0 | 187 \pm 56 | 330 ^[3] | 69 ^[18] | 1014 \pm 204 |
| MRK78 | 1.5 | 2.0 | 792 \pm 82 | 653 ^[60] | – | 422 \pm 91 |
| MRK1210 | 1.9 | 2.0 | 209 \pm 26 | 285 ^[18] | 840 ^[61] | 1244 \pm 260 |
| 2MASXJ08362280 | 3.4 | 2.0 | – | – | – | – |
| NGC2979 | 2.1 | 2.0 | – | 11 ^[18] | – | – |
| IC2560 | 2.0 | 2.0 | 558 \pm 85 | 125 ^[18] | 39 ^[62] | 469 \pm 115 |
| MRK34 | 3.0 | 2.0 | 626 \pm 76 | 520 ^[1] | 35 ^[11] | 244 \pm 67 |
| NGC3735 | 1.3 | 2.0 | – | 330 ^[59] | – | – |
| NGC4258 | 1.9 | 1.9 | 76 \pm 13 | 100 ^[63] | 837 ^[16] | 576 \pm 132 |
| ESO269-12 | 3.0 | 2.0 | – | 6 ^[18] | – | – |
| NGC4945 | 1.7 | 2.0 | 320 \pm 49 | – | 1300 ^[64] | – |
| NGC5495 | 2.3 | 2.0 | – | – | – | – |
| Circinus | 1.3 | 2.0 | 8599 \pm 1231 | 83 ^[65] | 1400 ^[66] | 39011 \pm 7803 |
| NGC5643 | 1.4 | 2.0 | 940 \pm 142 | 800 ^[1] | 84 ^[18] | – |
| NGC5728 | 1.9 | 1.9 | 1162 \pm 117 | 115 ^[18] | 133 ^[6] | 220 \pm 44 |

Table 6: continued.

| Source | H ₂ O | Sy | [OIV] | [OIII] | 2-10 keV | 7.6 μ m |
|----------------|------------------|-----|--------------|----------------------|---------------------|---------------|
| NGC5793 | 2.0 | 2.0 | – | – | 13 ^[11] | – |
| NGC6240 | 1.6 | 2.0 | 236 \pm 35 | 202 ^[5] | 91 ^[36] | 483 \pm 96 |
| NGC6264 | 3.1 | 2.0 | – | 3200 ^[67] | – | – |
| NGC6323 | 2.7 | 2.0 | – | – | – | – |
| NGC6300 | 0.5 | 2.0 | 304 \pm 33 | 140 ^[68] | 860 ^[69] | 887 \pm 177 |
| Eso103-G035 | 2.6 | 2.0 | – | 43 ^[18] | 907 ^[70] | – |
| IRAS19370-0131 | 2.2 | 2.0 | – | – | – | – |
| NGC6926 | 2.7 | 2.0 | 45 \pm 7 | 241 ^[5] | – | 64 \pm 13 |
| AM2158-380 | 2.7 | 2.0 | – | – | – | – |
| NGC7479 | 1.2 | 2.0 | < 136 | – | 112 ^[71] | – |

A.7 FIGURES

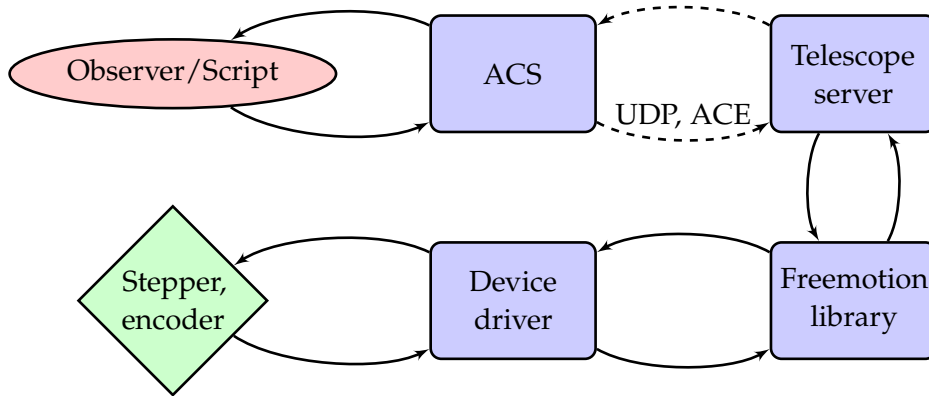


Figure 53: Chain of software interactions between observer’s script and telescope device. Red is the human-controlled component, blue represents the software and the hardware is green.

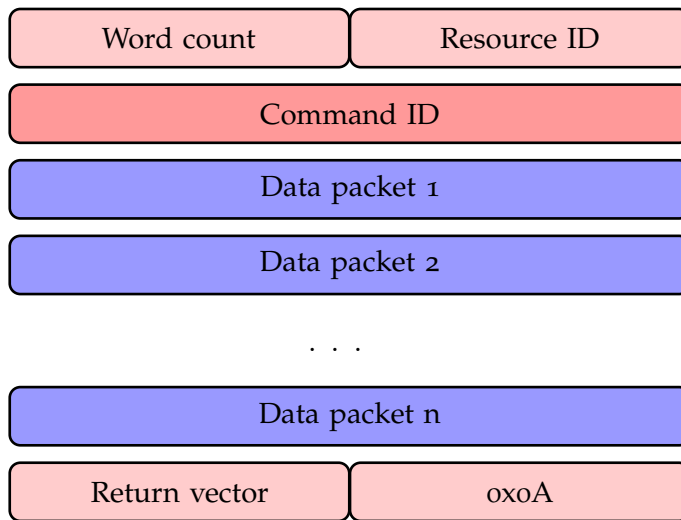


Figure 54: Format of the packets that are handled by the *National Instruments 7344* PCI card in order to process a command that contains n data blocks. The bigger blocks are 16 bit unsigned integers, while the smaller ones represent 8 bit blocks accordingly. The blocks colored in red denote essential header and footer packets of the communication. The blue packets are generally optional and depend on the Command ID. “Word count” is the complete number of data words plus header and footer (thus plus 3). “Resource ID” is the axis, encoder, vector space, ADC or DAC channel on the motion controller card. “Command ID” is an integer representation of one of the API motion commands. “Data packets” are limited to unsigned 16 bit integers. If a 64 bit double has to be send by the packet generator, it must be sliced bit-wise in four 16 bit blocks, in advance. “Return vector” is the source or destination address of data to send or receive.

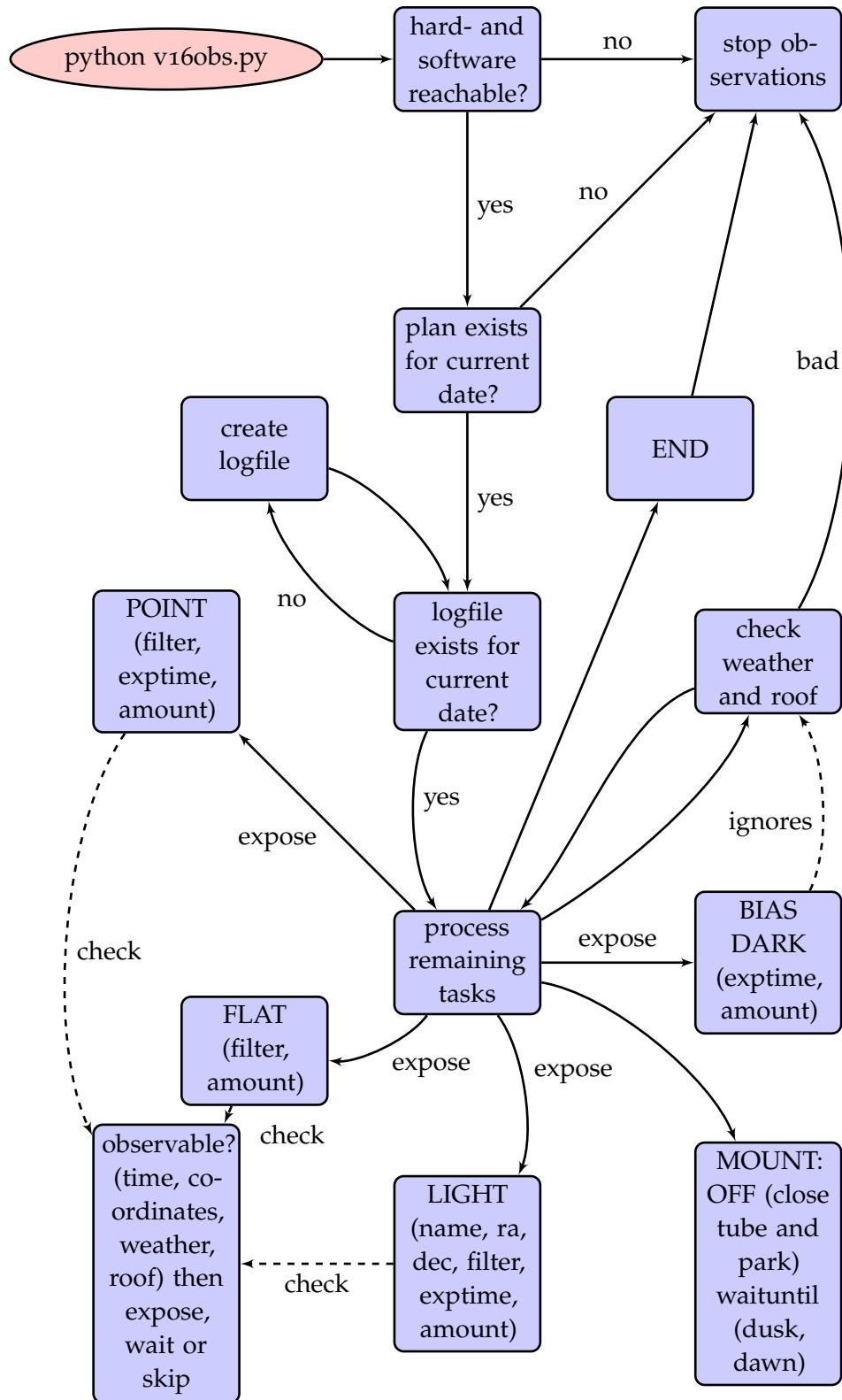


Figure 55: Workflow of the observations script.

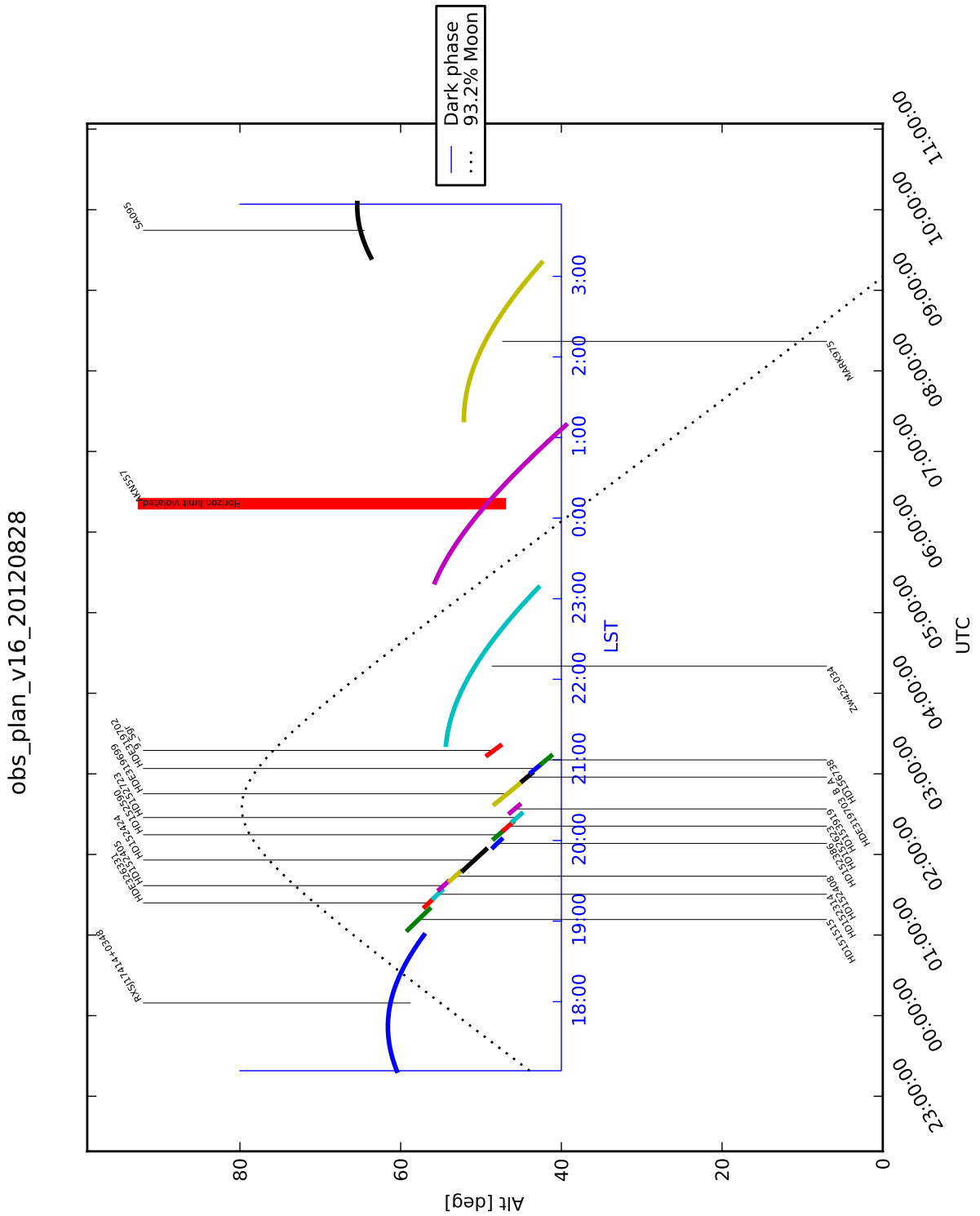


Figure 56: Example diagnostic plot of a successfully applied observation plan on August 28th 2012. Elevation versus time. The blue inner axis is stretching for the time of darkness in the night (sun is 12° below horizon) and is calibrated to local sidereal time (LST). The colored curves represent the altitude of the objects while they are being observed, with name-tags connected to them. If an object is critically low ($< 40^\circ$), the connection line is marked thick red, containing an error message. Here, the last images of AKN557 will eventually not be taken. The dotted curve is the altitude of the moon. This helps to determine optimally dark time for precision photometry targets.

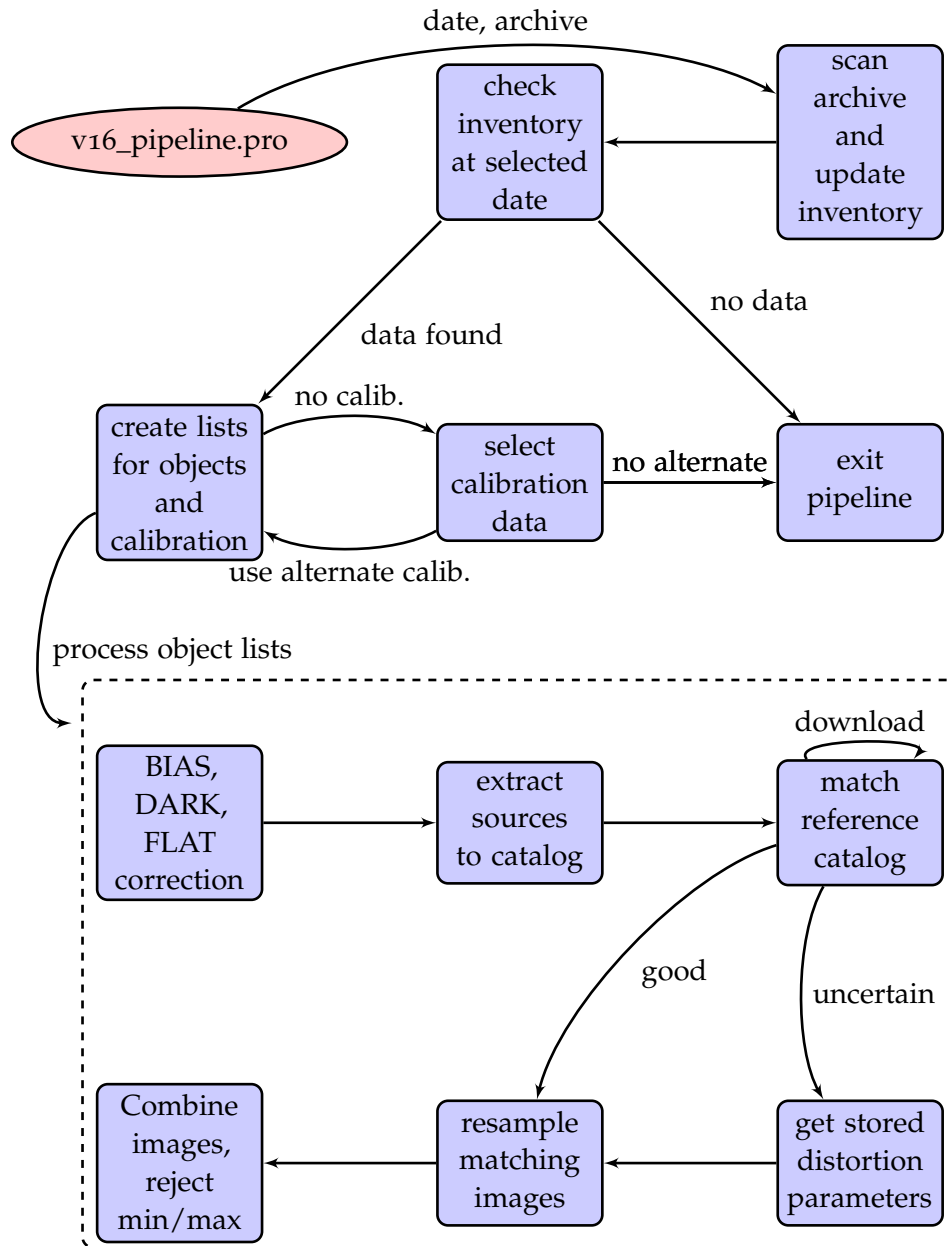


Figure 57: Workflow of the data reduction routine `v16_pipeline.pro`. Calibration data are flat-fields, dark-, and biasframes. The pipeline has a fixed amount of required calibration images (e.g. 20 darkframes, 10 flatfields in Johnson V-Band). If there are not enough calibration images at the selected observation date, the pipeline will search for alternative calibration data in the nearest neighboring observation dates until the required number of images is found. Uncertain matchings to reference catalogs can mean a reliable shift, but uncertain image distortion parameters. In this case, median distortion parameters will be used instead. Images that can't be matched or show defects of tracking are rejected and not used, when combining the final image.

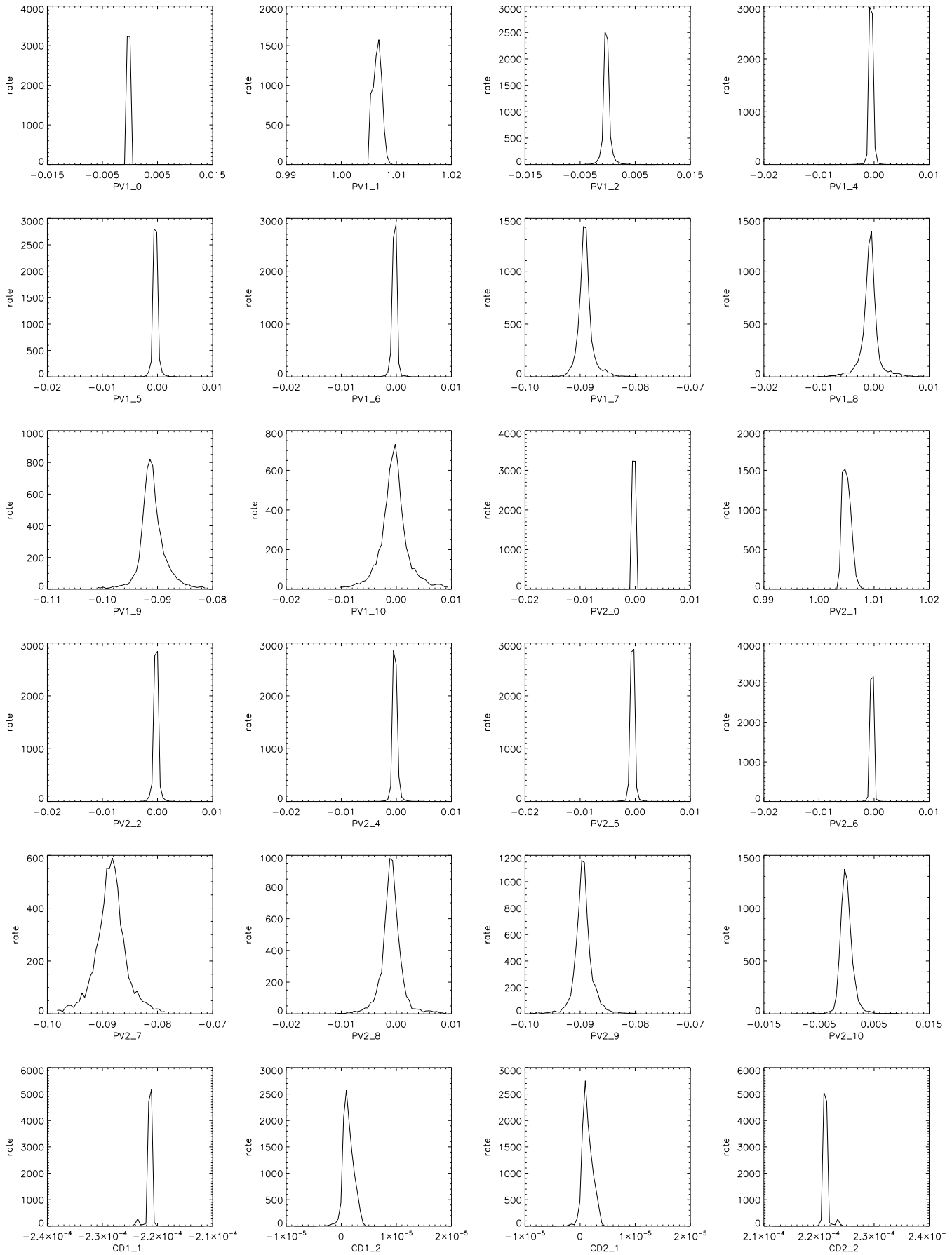


Figure 58: Histogram statistic for the PV distortion and CD projection coefficients for 10699 analyzed single images in the 670nm narrow band filter.

BIBLIOGRAPHY

- Danielle Alloin and Rachel Johnson. *Physics of Active Galactic Nuclei at all Scales*. Springer-Verlag Berlin Heidelberg, 2006. (Cited on pages 1 and 3.)
- A. Alonso-Herrero, M. J. Ward, and J. K. Kotilainen. [OIII] λ 5007, near-IR and X-ray properties of Seyfert 2 galaxies. *MNRAS*, 288:977–987, July 1997. (Cited on page 6.)
- R. Antonucci. Unified models for active galactic nuclei and quasars. *ARAA*, 31:473–521, 1993. doi: 10.1146/annurev.aa.31.090193.002353. (Cited on page 5.)
- R. R. J. Antonucci. Optical polarization position angle versus radio structure axis in Seyfert galaxies. *Nat.*, 303:158–+, May 1983. doi: 10.1038/303158a0. (Cited on page 2.)
- R. R. J. Antonucci and J. S. Miller. The Seyfert 1 Inside NGC 1068. In *Bulletin of the American Astronomical Society*, volume 16 of *Bulletin of the American Astronomical Society*, pages 957–+, September 1984. (Cited on page 2.)
- R. R. J. Antonucci and J. S. Miller. Spectropolarimetry and the nature of NGC 1068. *apj*, 297:621–632, October 1985. doi: 10.1086/163559. (Cited on page 2.)
- H. Awaki, S. Ueno, Y. Taniguchi, and K. A. Weaver. X-Ray Emission from Seyfert 2 Galaxies with Optical Polarized Broad Lines. *ApJ*, 542:175–185, October 2000. doi: 10.1086/309516. (Cited on page 82.)
- J. C. Baker. Origin of the viewing-angle dependence of the optical continuum emission in quasars. *MNRAS*, 286: 23–37, March 1997. (Cited on page 6.)
- J. Baldwin, G. Ferland, K. Korista, and D. Verner. Locally Optimally Emitting Clouds and the Origin of Quasar Emission Lines. *ApJL*, 455:L119, December 1995. doi: 10.1086/309827. (Cited on page 54.)
- R. Barvainis and R. Antonucci. Extremely Luminous Water Vapor Emission from a Type 2 Quasar at Redshift $z = 0.66$. *ApJL*, 628:L89–L91, August 2005. doi: 10.1086/432666. (Cited on page 68.)
- S. Barway, Y. D. Mayya, A. K. Kembhavi, and S. K. Pandey. Multicolor Surface Photometry of Lenticular Galaxies. I. The Data. *AJ*, 129:630–646, February 2005. doi: 10.1086/426906. (Cited on pages 28 and 52.)
- L. Bassani, M. Dadina, R. Maiolino, M. Salvati, G. Risaliti, R. della Ceca, G. Matt, and G. Zamorani. A Three-dimensional Diagnostic Diagram for Seyfert 2 Galaxies: Probing X-Ray Absorption and Compton Thickness. *ApJS*, 121:473–482, April 1999. doi: 10.1086/313202. (Cited on pages 6, 57, and 82.)
- S. A. Baum, J. F. Gallimore, C. P. O’Dea, C. L. Buchanan, J. Noel-Storr, D. J. Axon, A. Robinson, M. Elitzur, M. Dorn, and S. Staudaer. Infrared Diagnostics for the Extended 12 μ m Sample of Seyferts. *ApJ*, 710:289–308, February 2010. doi: 10.1088/0004-637X/710/1/289. (Cited on pages 6, 57, and 63.)
- R. Becker, C. Henkel, T. L. Wilson, and J. G. A. Wouterloot. H₂O masers in nearby irregular galaxies. *A&A*, 268: 483–490, February 1993. (Cited on page 58.)
- N. Bennert, H. Falcke, H. Schulz, A. S. Wilson, and B. J. Wills. Size and Structure of the Narrow-Line Region of Quasars. *ApJL*, 574:L105–L109, August 2002. doi: 10.1086/342420. (Cited on page 59.)
- N. Bennert, B. Jungwiert, S. Komossa, M. Haas, and R. Chini. Size and properties of the NLR in the Seyfert-2 galaxy <ASTROBJ>NGC 1386</ASTROBJ>. *A&A*, 446:919–932, February 2006. doi: 10.1051/0004-6361:20053571. (Cited on pages 24 and 82.)
- N. Bennert, R. Barvainis, C. Henkel, and R. Antonucci. A Search for H₂O Megamasers in High- z Type-2 Active Galactic Nuclei. *ApJ*, 695:276–286, April 2009. doi: 10.1088/0004-637X/695/1/276. (Cited on pages 58, 59, 67, 69, and 82.)
- M. C. Bentz, B. M. Peterson, R. W. Pogge, M. Vestergaard, and C. A. Onken. The Radius-Luminosity Relationship for Active Galactic Nuclei: The Effect of Host-Galaxy Starlight on Luminosity Measurements. *ApJ*, 644:133–142, June 2006. doi: 10.1086/503537. (Cited on pages 4, 44, 50, 51, and 79.)
- M. C. Bentz, K. D. Denney, E. M. Cackett, M. Dietrich, J. K. J. Fogel, H. Ghosh, K. D. Horne, C. Kuehn, T. Minezaki, C. A. Onken, B. M. Peterson, R. W. Pogge, V. I. Pronik, D. O. Richstone, S. G. Sergeev, M. Vestergaard, M. G. Walker, and Y. Yoshii. NGC 5548 in a Low-Luminosity State: Implications for the Broad-Line Region. *ApJ*, 662:205–212, June 2007. doi: 10.1086/516724. (Cited on page 44.)
- M. C. Bentz, B. M. Peterson, H. Netzer, R. W. Pogge, and M. Vestergaard. The Radius-Luminosity Relationship for Active Galactic Nuclei: The Effect of Host-Galaxy Starlight on Luminosity Measurements. II. The Full Sample of Reverberation-Mapped AGNs. *ApJ*, 697:160–181, May 2009a. doi: 10.1088/0004-637X/697/1/160. (Cited on pages 4, 47, 48, 49, 50, 51, 53, 54, 55, and 79.)
- M. C. Bentz, J. L. Walsh, A. J. Barth, N. Baliber, V. N. Bennert, G. Canalizo, A. V. Filippenko, M. Ganeshalingam, E. L. Gates, J. E. Greene, M. G. Hidas, K. D. Hiner, N. Lee, W. Li, M. A. Malkan, T. Minezaki, Y. Sakata, F. J. D. Serduke, J. M. Silverman, T. N. Steele, D. Stern, R. A. Street, C. E. Thornton, T. Treu, X. Wang, J.-H. Woo, and Y. Yoshii. The Lick AGN Monitoring Project: Broad-line Region Radii and Black Hole Masses from Reverberation Mapping of H β . *ApJ*, 705:199–217, November 2009b. doi: 10.1088/0004-637X/705/1/199. (Cited on pages 4, 32, 44, and 51.)

- M. C. Bentz, J. L. Walsh, A. J. Barth, Y. Yoshii, J.-H. Woo, X. Wang, T. Treu, C. E. Thornton, R. A. Street, T. N. Steele, J. M. Silverman, F. J. D. Serduke, Y. Sakata, T. Minezaki, M. A. Malkan, W. Li, N. Lee, K. D. Hiner, M. G. Hidas, J. E. Greene, E. L. Gates, M. Ganeshalingam, A. V. Filippenko, G. Canalizo, V. N. Bennert, and N. Baliber. The Lick AGN Monitoring Project: Reverberation Mapping of Optical Hydrogen and Helium Recombination Lines. *ApJ*, 716: 993–1011, June 2010. doi: 10.1088/0004-637X/716/2/993. (Cited on page 32.)
- S. Bianchi, I. Balestra, G. Matt, M. Guainazzi, and G. C. Perola. The recent X-ray history of NGC 5506. *A&A*, 402: 141–149, April 2003. doi: 10.1051/0004-6361:20030210. (Cited on page 82.)
- S. Bianchi, G. Miniutti, A. C. Fabian, and K. Iwasawa. The XMM-Newton view of Mrk 3 and IXO 30. *MNRAS*, 360: 380–389, June 2005. doi: 10.1111/j.1365-2966.2005.09048.x. (Cited on page 82.)
- R. D. Blandford and C. F. McKee. Reverberation mapping of the emission line regions of Seyfert galaxies and quasars. *ApJ*, 255:419–439, April 1982. doi: 10.1086/159843. (Cited on pages 3 and 78.)
- A. J. Blustin, G. Branduardi-Raymont, E. Behar, J. S. Kaastra, S. M. Kahn, M. J. Page, M. Sako, and K. C. Steenbrugge. Multi-wavelength study of the Seyfert 1 galaxy NGC 3783 with XMM-Newton. *A&A*, 392:453–467, September 2002. doi: 10.1051/0004-6361:20020914. (Cited on page 82.)
- T. A. Boroson and K. A. Meyers. The optical properties of IR-selected and MG II broad absorption line quasars. *ApJ*, 397:442–451, October 1992. doi: 10.1086/171800. (Cited on page 82.)
- J. Braatz. The Megamaser Cosmology Project. In *A Decade of Dark Energy*, May 2008. (Cited on page 58.)
- J. A. Braatz and N. E. Gugliucci. The Discovery of Water Maser Emission from Eight Nearby Galaxies. *ApJ*, 678:96–101, May 2008. doi: 10.1086/529538. (Cited on page 58.)
- J. A. Braatz, A. S. Wilson, and C. Henkel. A Survey for H₂O Megamasers in Active Galactic Nuclei. I. Observations. *ApJS*, 106:51–+, September 1996. doi: 10.1086/192328. (Cited on page 58.)
- J. A. Braatz, A. S. Wilson, and C. Henkel. A Survey for H₂O Megamasers in Active Galactic Nuclei. II. A Comparison of Detected and Undetected Galaxies. *ApJS*, 110:321–+, June 1997. doi: 10.1086/312999. (Cited on page 5.)
- J. A. Braatz, A. S. Wilson, C. Henkel, R. Gough, and M. Sinclair. A Survey for H₂O Megamasers. III. Monitoring Water Vapor Masers in Active Galaxies. *ApJS*, 146:249–265, June 2003. doi: 10.1086/374417. (Cited on page 58.)
- J. A. Braatz, C. Henkel, L. J. Greenhill, J. M. Moran, and A. S. Wilson. A Green Bank Telescope Search for Water Masers in Nearby Active Galactic Nuclei. *ApJL*, 617:L29–L32, December 2004. doi: 10.1086/427185. (Cited on pages 5 and 58.)
- V. Braito, A. Franceschini, R. Della Ceca, P. Severgnini, L. Bassani, M. Cappi, G. Malaguti, G. G. C. Palumbo, M. Persic, G. Risaliti, and M. Salvati. XMM-Newton observations of ULIRGs: A Compton-thick AGN in IRAS 19254-7245. *A&A*, 398:107–111, January 2003. doi: 10.1051/0004-6361:20021633. (Cited on page 82.)
- Christoph Bruckmann. Modelling of Photometric AGN Reverberation Mapping, December 2012. (Cited on page 30.)
- C. L. Buchanan, J. F. Gallimore, C. P. O’Dea, S. A. Baum, D. J. Axon, A. Robinson, M. Elitzur, and M. Elvis. Spitzer IRS Spectra of a Large Sample of Seyfert Galaxies: A Variety of Infrared Spectral Energy Distributions in the Local Active Galactic Nucleus Population. *AJ*, 132:401–419, July 2006. doi: 10.1086/505022. (Cited on pages 6, 59, and 82.)
- M. Cappi, F. Panessa, L. Bassani, M. Dadina, G. Di Cocco, A. Comastri, R. della Ceca, A. V. Filippenko, F. Gianotti, L. C. Ho, G. Malaguti, J. S. Mulchaey, G. G. C. Palumbo, E. Piconcelli, W. L. W. Sargent, J. Stephen, M. Trifoglio, and K. A. Weaver. X-ray spectral survey with XMM-Newton of a complete sample of nearby Seyfert galaxies. *A&A*, 446:459–470, February 2006. doi: 10.1051/0004-6361:20053893. (Cited on page 82.)
- D. Chelouche and E. Daniel. Photometric Reverberation Mapping of the Broad Emission Line Region in Quasars. *ApJ*, 747:62, March 2012. doi: 10.1088/0004-637X/747/1/62. (Cited on page 56.)
- J. Choloniewski. The Shape and Variability of the Nonthermal Component of the Optical Spectra of Active Galaxies. *Acta Astronomica*, 31:293, 1981. (Cited on pages 4, 31, 45, 46, 48, 55, and 78.)
- M. J. Claussen and K.-Y. Lo. Circumnuclear water vapor masers in active galaxies. *ApJ*, 308:592–599, September 1986. doi: 10.1086/164529. (Cited on page 58.)
- O. Dahari and M. M. De Robertis. A statistical study of properties of Seyfert and starburst galaxies. *ApJS*, 67:249–277, July 1988. doi: 10.1086/191273. (Cited on page 82.)
- M. H. K. de Grijp, W. C. Keel, G. K. Miley, P. Goudfrooij, and J. Lub. Warm IRAS sources. II - Optical spectroscopy of objects from the point source catalog. *A&AS*, 96:389–428, December 1992. (Cited on pages 2, 57, and 82.)
- K. D. Denney, M. C. Bentz, B. M. Peterson, R. W. Pogge, E. M. Cackett, M. Dietrich, J. K. J. Fogel, H. Ghosh, K. D. Horne, C. Kuehn, T. Minezaki, C. A. Onken, V. I. Pronik, D. O. Richstone, S. G. Sergeev, M. Vestergaard, M. G. Walker, and Y. Yoshii. The Mass of the Black Hole in the Seyfert 1 Galaxy NGC 4593 from Reverberation Mapping. *ApJ*, 653:152–158, December 2006. doi: 10.1086/508533. (Cited on page 44.)
- K. D. Denney, B. M. Peterson, M. Dietrich, M. Vestergaard, and M. C. Bentz. Systematic Uncertainties in Black Hole Masses Determined from Single-Epoch Spectra. *ApJ*, 692:246–264, February 2009. doi: 10.1088/0004-637X/692/1/246. (Cited on pages 25, 27, 28, and 44.)
- R. P. Deo, D. M. Crenshaw, S. B. Kraemer, M. Dietrich, M. Elitzur, H. Teplitz, and T. J. Turner. Spitzer IRS Observations of Seyfert 1.8 and 1.9 Galaxies: A Comparison with Seyfert 1 and Seyfert 2. *ApJ*, 671:124–135, December 2007. doi: 10.1086/522823. (Cited on pages 59 and 63.)

- R. P. Deo, G. T. Richards, D. M. Crenshaw, and S. B. Kraemer. The Mid-Infrared Continua of Seyfert Galaxies. *ApJ*, 705:14–31, November 2009. doi: 10.1088/0004-637X/705/1/14. (Cited on page 59.)
- S. di Serego Alighieri, A. Cimatti, R. A. E. Fosbury, and R. Hes. Anisotropic [OIII] emission in radio loud AGN. *A&A*, 328:510–516, December 1997. (Cited on page 6.)
- M. S. Dimitrijević, L. Č. Popović, J. Kovačević, M. Dačić, and D. Ilić. The flux ratio of the [OIII] $\lambda\lambda 5007, 4959$ lines in AGN: comparison with theoretical calculations. *MNRAS*, 374:1181–1184, January 2007. doi: 10.1111/j.1365-2966.2006.11238.x. (Cited on page 25.)
- C. Done, G. M. Madejski, P. T. Życki, and L. J. Greenhill. Simultaneous Chandra and Rossi X-Ray Timing Explorer Observations of the Nearby Bright Seyfert 2 Galaxy NGC 4945. *ApJ*, 588:763–770, May 2003. doi: 10.1086/374332. (Cited on page 82.)
- V. T. Doroshenko, S. G. Sergeev, V. I. Pronik, and K. K. Chuvaev. H β and continuum variability in the Seyfert galaxy Akn 120 from Crimean observations during 1974–1990. *Astronomy Letters*, 25:569–581, September 1999. (Cited on pages 25, 37, and 45.)
- V. T. Doroshenko, S. G. Sergeev, and V. I. Pronik. The Seyfert 1 galaxy Ark 120 in 1996 2005: U BV RI photometry. *Astronomy Reports*, 52:167–183, March 2008. doi: 10.1134/S1063772908030013. (Cited on pages 48, 49, and 79.)
- R. A. Edelson and J. H. Krolik. The discrete correlation function - A new method for analyzing unevenly sampled variability data. *ApJ*, 333:646–659, October 1988. doi: 10.1086/166773. (Cited on pages 4, 31, 55, and 78.)
- M. Elitzur. Topics in basic maser theory. In V. Migenes & M. J. Reid, editor, *Cosmic Masers: From Proto-Stars to Black Holes*, volume 206 of *IAU Symposium*, pages 452–+, 2002. (Cited on page 5.)
- M. Elvis and M. Karovska. Quasar Parallax: A Method for Determining Direct Geometrical Distances to Quasars. *ApJL*, 581:L67–L70, December 2002. doi: 10.1086/346015. (Cited on page 56.)
- M. Elvis, B. J. Wilkes, J. C. McDowell, R. F. Green, J. Bechtold, S. P. Willner, M. S. Oey, E. Polomski, and R. Cutri. Atlas of quasar energy distributions. *ApJS*, 95:1–68, November 1994. doi: 10.1086/192093. (Cited on pages 46 and 47.)
- R. Genzel, D. Lutz, E. Sturm, E. Egami, D. Kunze, A. F. M. Moorwood, D. Rigopoulou, H. W. W. Spoon, A. Sternberg, L. E. Tacconi-Garman, L. Tacconi, and N. Thatte. What Powers Ultraluminous IRAS Galaxies? *ApJ*, 498:579–+, May 1998. doi: 10.1086/305576. (Cited on page 57.)
- P. Gondoin, P. Barr, D. Lumb, T. Oosterbroek, A. Orr, and A. N. Parmar. Simultaneous XMM-Newton and BeppoSAX observation of the Seyfert I galaxy IC 4329A. *A&A*, 378:806–816, November 2001. doi: 10.1051/0004-6361:20011258. (Cited on page 82.)
- P. Gondoin, A. Orr, D. Lumb, and M. Santos-Lleo. XMM-Newton observations of the Seyfert 1 galaxy Mrk 335. *A&A*, 388:74–87, June 2002. doi: 10.1051/0004-6361:20020435. (Cited on page 82.)
- P. Gondoin, A. Orr, and D. Lumb. XMM-Newton observations of the Seyfert 1 galaxy ESO 141-G55. *A&A*, 398:967–973, February 2003a. doi: 10.1051/0004-6361:20021694. (Cited on page 82.)
- P. Gondoin, A. Orr, D. Lumb, and H. Siddiqui. XMM-Newton observations of the Seyfert 1 galaxy NGC 3227. *A&A*, 397:883–890, January 2003b. doi: 10.1051/0004-6361:20021574. (Cited on page 82.)
- O. González-Martín, J. Masegosa, I. Márquez, M. A. Guerrero, and D. Dultzin-Hacyan. X-ray nature of the LINER nuclear sources. *A&A*, 460:45–57, December 2006. doi: 10.1051/0004-6361:20054756. (Cited on page 82.)
- A. W. Graham, C. A. Onken, E. Athanassoula, and F. Combes. An expanded $M_{bh}-\sigma$ diagram, and a new calibration of active galactic nuclei masses. *MNRAS*, 412:2211–2228, April 2011. doi: 10.1111/j.1365-2966.2010.18045.x. (Cited on page 44.)
- L. J. Greenhill, J. M. Moran, M. J. Reid, C. R. Gwinn, K. M. Menten, A. Eckart, and H. Hirabayashi. First images of water vapor masers in the galaxy M33. *ApJ*, 364:513–526, December 1990. doi: 10.1086/169433. (Cited on page 58.)
- L. J. Greenhill, J. M. Moran, M. J. Reid, K. M. Menten, and H. Hirabayashi. Microarcsecond proper motions of extragalactic water vapor masers in M33. *ApJ*, 406:482–488, April 1993. doi: 10.1086/172460. (Cited on page 5.)
- L. J. Greenhill, C. Henkel, R. Becker, T. L. Wilson, and J. G. A. Wouterloot. Centripetal acceleration within the subparsec nuclear maser disk of NGC4258. *A&A*, 304:21–+, December 1995. (Cited on page 58.)
- L. J. Greenhill, J. R. Herrnstein, J. M. Moran, K. M. Menten, and T. Velusamy. A Search for H $_2$ O Maser Emission toward Active Galactic Nuclei: Discovery of a Nuclear Maser Source in NGC 3735. *ApJL*, 486:L15+, September 1997. doi: 10.1086/310824. (Cited on page 58.)
- L. J. Greenhill, S. P. Ellingsen, R. P. Norris, P. J. McGregor, R. G. Gough, M. W. Sinclair, D. P. Rayner, C. J. Phillips, J. R. Herrnstein, and J. M. Moran. A Search for H $_2$ O Maser Emission in Southern Active Galactic Nuclei and Star-forming Galaxies: Discovery of a Maser in the Edge-on Galaxy IRAS F01063-8034. *ApJ*, 565:836–848, February 2002. doi: 10.1086/324383. (Cited on page 58.)
- L. J. Greenhill, A. Tilak, and G. Madejski. Prevalence of High X-Ray Obscuring Columns among AGNs that Host H $_2$ O Masers. *ApJL*, 686:L13–L16, October 2008. doi: 10.1086/592782. (Cited on pages 5, 60, and 82.)
- C. J. Grier, B. M. Peterson, M. C. Bentz, K. D. Denney, J. D. Eastman, M. Dietrich, R. W. Pogge, J. L. Prieto, D. L. DePoy, R. J. Assef, D. W. Atlee, J. Bird, M. E. Eyley, M. S. Peeples, R. Siverd, L. C. Watson, and J. C. Yee. The Mass of the Black Hole in the Quasar PG 2130+099. *ApJ*, 688:837–843, December 2008. doi: 10.1086/592269. (Cited on page 44.)

- C. J. Grier, B. M. Peterson, R. W. Pogge, K. D. Denney, M. C. Bentz, P. Martini, S. G. Sergeev, S. Kaspi, T. Minezaki, Y. Zu, C. S. Kochanek, R. Siverd, B. Shappee, K. Z. Stanek, C. Araya Salvo, T. G. Beatty, J. C. Bird, D. J. Bord, G. A. Borman, X. Che, C. Chen, S. A. Cohen, M. Dietrich, V. T. Doroshenko, T. Drake, Y. S. Efimov, N. Free, I. Ginsburg, C. B. Henderson, A. L. King, S. Koshida, K. Mogren, M. Molina, A. M. Mosquera, S. V. Nazarov, D. N. Okhmat, O. Pejcha, S. Rafter, J. C. Shields, J. Skowron, D. M. Szczygiel, M. Valluri, and J. L. van Sadlers. Reverberation Mapping Results for Five Seyfert 1 Galaxies. *ApJ*, 755:60, August 2012a. doi: 10.1088/0004-637X/755/1/60. (Cited on pages 4, 27, 41, 45, 52, 54, 55, and 56.)
- C. J. Grier, B. M. Peterson, R. W. Pogge, K. D. Denney, M. C. Bentz, P. Martini, S. G. Sergeev, S. Kaspi, Y. Zu, C. S. Kochanek, B. J. Shappee, K. Z. Stanek, C. Araya Salvo, T. G. Beatty, J. C. Bird, D. J. Bord, G. A. Borman, X. Che, C. Chen, S. A. Cohen, M. Dietrich, V. T. Doroshenko, Y. S. Efimov, N. Free, I. Ginsburg, C. B. Henderson, K. Horne, A. L. King, K. Mogren, M. Molina, A. M. Mosquera, S. V. Nazarov, D. N. Okhmat, O. Pejcha, S. Rafter, J. C. Shields, J. Skowron, D. M. Szczygiel, M. Valluri, and J. L. van Sadlers. A Reverberation Lag for the High-ionization Component of the Broad-line Region in the Narrow-line Seyfert 1 Mrk 335. *ApJL*, 744:L4, January 2012b. doi: 10.1088/2041-8205/744/1/L4. (Cited on page 32.)
- Q. Gu, J. Melnick, R. C. Fernandes, D. Kunth, E. Terlevich, and R. Terlevich. Emission-line properties of Seyfert 2 nuclei (Gu+, 2006). *VizieR Online Data Catalog*, 736:60480+, June 2006. (Cited on page 82.)
- M. Guainazzi, G. Matt, and G. C. Perola. X-ray obscuration and obscured AGN in the local universe. *A&A*, 444: 119–132, December 2005. doi: 10.1051/0004-6361:20053643. (Cited on page 82.)
- M. Haas, R. Siebenmorgen, B. Schulz, E. Krügel, and R. Chini. Spitzer IRS spectroscopy of 3CR radio galaxies and quasars: testing the unified schemes. *A&A*, 442:L39–L43, November 2005. doi: 10.1051/0004-6361:200500185. (Cited on pages 6, 57, 63, and 68.)
- M. Haas, R. Chini, M. Ramolla, F. Pozo Nuñez, C. Westhues, R. Watermann, V. Hoffmeister, and M. Murphy. Photometric AGN reverberation mapping - an efficient tool for BLR sizes, black hole masses, and host-subtracted AGN luminosities. *A&A*, 535:A73, November 2011. doi: 10.1051/0004-6361/201117325. (Cited on page 4.)
- Y. Hagiwara, P. J. Diamond, and M. Miyoshi. A search for extragalactic H₂O maser emission towards IRAS galaxies. Detection of a maser from an infrared-luminous merger, NGC 6240. *A&A*, 383:65–70, January 2002. doi: 10.1051/0004-6361:20011687. (Cited on page 58.)
- Y. Hagiwara, P. J. Diamond, M. Miyoshi, E. Rovilos, and W. Baan. A search for extragalactic H₂O maser emission towards IRAS galaxies - II. Discovery of an H₂O maser in the type 1 Seyfert galaxy NGC 4051. *MNRAS*, 344: L53–L57, October 2003. doi: 10.1046/j.1365-8711.2003.07005.x. (Cited on page 58.)
- A. D. Haschick and W. A. Baan. A very bright water vapour maser source in the galaxy NGC3079. *Nat.*, 314:144–146, March 1985. doi: 10.1038/314144a0. (Cited on page 58.)
- T. M. Heckman, P. C. Crane, and B. Balick. An optical and radio survey of the nuclei of bright galaxies - Sample selection and observations. *A&AS*, 40:295–305, June 1980. (Cited on page 82.)
- T. M. Heckman, A. Ptak, A. Hornschemeier, and G. Kauffmann. The Relationship of Hard X-Ray and Optical Line Emission in Low-Redshift Active Galactic Nuclei. *ApJ*, 634:161–168, November 2005. doi: 10.1086/491665. (Cited on page 6.)
- C. Henkel. The Megamaser Cosmology Project. In *A Decade of Dark Energy*, 2008. (Cited on page 58.)
- C. Henkel, R. Guesten, D. Downes, C. Thum, T. L. Wilson, and P. Biermann. Strong H₂O maser emission from the peculiar galaxy NGC 3079. *A&A*, 141:L1–L3, December 1984. (Cited on page 58.)
- C. Henkel, J. G. A. Wouterloot, and J. Bally. H₂O and OH maser emission from bright IRAS galaxies. *A&A*, 155: 193–199, January 1986. (Cited on page 58.)
- C. Henkel, Y. P. Wang, H. Falcke, A. S. Wilson, and J. A. Braatz. H₂O megamaser emission from FR I radio galaxies. *A&A*, 335:463–466, July 1998. (Cited on page 58.)
- C. Henkel, A. B. Peck, A. Tarchi, N. M. Nagar, J. A. Braatz, P. Castangia, and L. Moscadelli. New H₂O masers in Seyfert and FIR bright galaxies. *A&A*, 436:75–90, June 2005. doi: 10.1051/0004-6361:20042175. (Cited on pages 5 and 58.)
- J. R. Herrnstein, J. M. Moran, L. J. Greenhill, P. J. Diamond, M. Inoue, N. Nakai, M. Miyoshi, C. Henkel, and A. Riess. A geometric distance to the galaxy NGC4258 from orbital motions in a nuclear gas disk. *Nat.*, 400:539–541, August 1999. doi: 10.1038/22972. (Cited on page 5.)
- R. Hes, P. D. Barthel, and R. A. E. Fosbury. Emission line imaging of 3CR quasars and radio galaxies. *A&A*, 313: 423–438, September 1996. (Cited on page 6.)
- L. C. Ho. [O II] Emission in Quasar Host Galaxies: Evidence for a Suppressed Star Formation Efficiency. *ApJ*, 629: 680–685, August 2005. doi: 10.1086/431643. (Cited on page 6.)
- L. C. Ho, A. V. Filippenko, and W. L. Sargent. A search for ‘dwarf’ Seyfert nuclei. 2: an optical spectral atlas of the nuclei of nearby galaxies. *ApJS*, 98:477–593, June 1995. doi: 10.1086/192170. (Cited on page 82.)
- L. C. Ho, A. V. Filippenko, and W. L. W. Sargent. A Search for “Dwarf” Seyfert Nuclei. III. Spectroscopic Parameters and Properties of the Host Galaxies. *ApJS*, 112:315+, October 1997. doi: 10.1086/313041. (Cited on page 82.)
- T. Holczer, E. Behar, and S. Kaspi. Absorption Measure Distribution of the Outflow in IRAS 13349+2438: Direct Observation of Thermal Instability? *ApJ*, 663:799–807, July 2007. doi: 10.1086/518416. (Cited on page 82.)

- K. Horne, K. T. Korista, and M. R. Goad. Quasar tomography: unification of echo mapping and photoionization models. *MNRAS*, 339:367–386, February 2003. doi: 10.1046/j.1365-8711.2003.06036.x. (Cited on page 56.)
- K. Horne, B. M. Peterson, S. J. Collier, and H. Netzer. Observational Requirements for High-Fidelity Reverberation Mapping. *PASP*, 116:465–476, May 2004. doi: 10.1086/420755. (Cited on page 24.)
- J. Huchra and R. Burg. The spatial distribution of active galactic nuclei. I - The density of Seyfert galaxies and liners. *apj*, 393:90–97, July 1992. doi: 10.1086/171488. (Cited on pages 57 and 81.)
- S. Immler, W. N. Brandt, C. Vignali, F. E. Bauer, D. M. Crenshaw, J. J. Feldmeier, and S. B. Kraemer. Probing the Complex and Variable X-Ray Absorption of Markarian 6 with XMM-Newton. *AJ*, 126:153–157, July 2003. doi: 10.1086/375652. (Cited on page 82.)
- T. Isobe, E. D. Feigelson, M. G. Akritas, and G. J. Babu. Linear regression in astronomy. *ApJ*, 364:104–113, November 1990. doi: 10.1086/169390. (Cited on page 52.)
- N. Iyomoto, K. Makishima, Y. Fukazawa, M. Tashiro, Y. Ishisaki, N. Nakai, and Y. Taniguchi. Detection of Excess Hard X-Ray Emission from the Optical Jet Galaxy NGC 1097. *PASJ*, 48:231–236, April 1996. (Cited on page 82.)
- S. Kaspi, P. S. Smith, H. Netzer, D. Maoz, B. T. Jannuzi, and U. Giveon. Reverberation Measurements for 17 Quasars and the Size-Mass-Luminosity Relations in Active Galactic Nuclei. *ApJ*, 533:631–649, April 2000. doi: 10.1086/308704. (Cited on pages 4, 32, and 53.)
- S. Kaspi, D. Maoz, H. Netzer, B. M. Peterson, M. Vestergaard, and B. T. Jannuzi. The Relationship between Luminosity and Broad-Line Region Size in Active Galactic Nuclei. *ApJ*, 629:61–71, August 2005. doi: 10.1086/431275. (Cited on pages 4 and 53.)
- W. C. Keel. Spectroscopic evidence for activity in the nuclei of normal spiral galaxies. *ApJ*, 269:466–486, June 1983. doi: 10.1086/161057. (Cited on page 2.)
- L. J. Kewley, C. A. Heisler, M. A. Dopita, and S. Lumsden. Optical Classification of Southern Warm Infrared Galaxies. *ApJS*, 132:37–71, January 2001. doi: 10.1086/318944. (Cited on page 82.)
- D.-C. Kim, D. B. Sanders, S. Veilleux, J. M. Mazzarella, and B. T. Soifer. Optical Spectroscopy of Luminous Infrared Galaxies. I. Nuclear Data. *ApJS*, 98:129–+, May 1995. doi: 10.1086/192157. (Cited on page 82.)
- W. Kollatschny. Accretion disk wind in the AGN broad-line region: Spectroscopically resolved line profile variations in Mrk 110. *A&A*, 407:461–472, August 2003a. doi: 10.1051/0004-6361:20030928. (Cited on pages 32 and 55.)
- W. Kollatschny. Spin orientation of supermassive black holes in active galaxies. *A&A*, 412:L61–L64, December 2003b. doi: 10.1051/0004-6361:20034611. (Cited on page 55.)
- W. Kollatschny and M. Zetzl. Broad-line active galactic nuclei rotate faster than narrow-line ones. *Nat.*, 470:366–368, February 2011. doi: 10.1038/nature09761. (Cited on page 55.)
- P. T. Kondratko, L. J. Greenhill, and J. M. Moran. Discovery of Water Maser Emission in Five AGNs and a Possible Correlation Between Water Maser and Nuclear 2–10 keV Luminosities. *ApJ*, 652:136–145, November 2006a. doi: 10.1086/507885. (Cited on page 58.)
- P. T. Kondratko, L. J. Greenhill, J. M. Moran, J. E. J. Lovell, T. B. H. Kuiper, D. L. Jauncey, L. B. Cameron, J. F. Gómez, C. García-Miró, E. Moll, I. de Gregorio-Monsalvo, J. McCallum, and E. Jiménez-Bailón. Erratum: “Discovery of Water Maser Emission in Eight AGNs with 70 m Antennas of NASA’s Deep Space Network” (ApJ, 638, 100 [2006]). *ApJ*, 649:561–561, September 2006b. doi: 10.1086/504978. (Cited on page 58.)
- A. P. Koratkar and C. M. Gaskell. Radius-luminosity and mass-luminosity relationships for active galactic nuclei. *ApJL*, 370:L61–L64, April 1991. doi: 10.1086/185977. (Cited on page 4.)
- K. T. Korista. The broad emission-line profiles and profile variability of the Seyfert 1 galaxy Arakelian 120. *ApJS*, 79:285–301, April 1992. doi: 10.1086/191654. (Cited on page 25.)
- A. Lamastra, S. Bianchi, G. Matt, G. C. Perola, X. Barcons, and F. J. Carrera. The bolometric luminosity of type 2 AGN from extinction-corrected [OIII]. No evidence of Eddington-limited sources. *A&A*, 504:73–79, September 2009. doi: 10.1051/0004-6361/200912023. (Cited on page 6.)
- A. U. Landolt. UBVRI Photometric Standard Stars Around the Celestial Equator: Updates and Additions. *AJ*, 137:4186–4269, May 2009. doi: 10.1088/0004-6256/137/5/4186. (Cited on pages 21 and 22.)
- A. J. Lawson and M. J. L. Turner. GINGA observations of the X-ray spectra of quasars. *MNRAS*, 288:920–944, July 1997. (Cited on page 82.)
- N. A. Levenson, T. M. Heckman, J. H. Krolik, K. A. Weaver, and P. T. Życki. Penetrating the Deep Cover of Compton-thick Active Galactic Nuclei. *ApJ*, 648:111–127, September 2006. doi: 10.1086/505735. (Cited on page 82.)
- K. Y. Lo. Mega-Masers and Galaxies. *ARAA*, 43:625–676, September 2005. doi: 10.1146/annurev.astro.41.011802.094927. (Cited on page 5.)
- S. L. Lumsden and D. M. Alexander. The infrared luminosity of the torus and the visibility of scattered broad line emission in Seyfert 2 galaxies. *MNRAS*, 328:L32–L36, December 2001. doi: 10.1046/j.1365-8711.2001.05074.x. (Cited on page 82.)
- S. L. Lumsden, D. M. Alexander, and J. H. Hough. Spectropolarimetry of Compton-thin Seyfert 2 galaxies. *MNRAS*, 348:1451–1458, March 2004. doi: 10.1111/j.1365-2966.2004.07469.x. (Cited on page 82.)

- R. Maiolino and G. H. Rieke. Low-Luminosity and Obscured Seyfert Nuclei in Nearby Galaxies. *ApJ*, 454:95–+, November 1995. doi: 10.1086/176468. (Cited on page 6.)
- A. Malizia, R. Landi, L. Bassani, A. J. Bird, M. Molina, A. De Rosa, M. Fiacchi, N. Gehrels, J. Kennea, and M. Perri. Swift XRT Observation of 34 New INTEGRAL IBIS AGNs: Discovery of Compton-Thick and Other Peculiar Sources. *ApJ*, 668:81–86, October 2007. doi: 10.1086/520874. (Cited on page 82.)
- C. Matsumoto, A. Nava, L. A. Maddox, K. M. Leighly, D. Grupe, H. Awaki, and S. Ueno. An XMM-Newton Observation of the Seyfert 2 Galaxy NGC 6300. I. The Nucleus. *ApJ*, 617:930–938, December 2004. doi: 10.1086/425566. (Cited on page 82.)
- G. Matt, G. C. Perola, F. Fiore, M. Guainazzi, F. Nicastro, and L. Piro. The BeppoSAX observation of Mrk 766. *A&A*, 363:863–868, November 2000. (Cited on page 82.)
- C. W. McAlary, R. A. McLaren, R. J. McGonegal, and J. Maza. A near-infrared and optical study of X-ray selected Seyfert Galaxies. I - Observations. *ApJS*, 52:341–362, August 1983. doi: 10.1086/190871. (Cited on pages 46 and 47.)
- R. J. McLure and J. S. Dunlop. The cosmological evolution of quasar black hole masses. *MNRAS*, 352:1390–1404, August 2004. doi: 10.1111/j.1365-2966.2004.08034.x. (Cited on page 53.)
- M. Meléndez, S. B. Kraemer, B. K. Armentrout, R. P. Deo, D. M. Crenshaw, H. R. Schmitt, R. F. Mushotzky, J. Tueller, C. B. Markwardt, and L. Winter. New Indicators for AGN Power: The Correlation between [O IV] 25.89 μm and Hard X-Ray Luminosity for Nearby Seyfert Galaxies. *ApJ*, 682:94–103, July 2008a. doi: 10.1086/588807. (Cited on pages 6 and 57.)
- M. Meléndez, S. B. Kraemer, H. R. Schmitt, D. M. Crenshaw, R. P. Deo, R. F. Mushotzky, and F. C. Bruhweiler. Constraining the Active Galactic Nucleus Contribution in a Multiwavelength Study of Seyfert Galaxies. *ApJ*, 689:95–107, December 2008b. doi: 10.1086/592724. (Cited on page 63.)
- K. G. Metzroth, C. A. Onken, and B. M. Peterson. The Mass of the Central Black Hole in the Seyfert Galaxy NGC 4151. *ApJ*, 647:901–909, August 2006. doi: 10.1086/505525. (Cited on page 44.)
- G. Miniutti, G. Ponti, M. Dadina, M. Cappi, and G. Malaguti. IRAS 13197-1627 has them all: Compton-thin absorption, photoionized gas, thermal plasmas and a broad Fe line. *MNRAS*, 375:227–239, February 2007. doi: 10.1111/j.1365-2966.2006.11291.x. (Cited on page 82.)
- J. Moustakas and R. C. Kennicutt, Jr. An Integrated Spectrophotometric Survey of Nearby Star-forming Galaxies. *ApJS*, 164:81–98, May 2006. doi: 10.1086/500971. (Cited on page 82.)
- J. S. Mulchaey, A. Koratkar, M. J. Ward, A. S. Wilson, M. Whittle, R. R. J. Antonucci, A. L. Kinney, and T. Hurt. Multiwavelength tests of the dusty torus model for Seyfert galaxies. *ApJ*, 436:586–598, December 1994. doi: 10.1086/174933. (Cited on page 6.)
- N. Nakai, M. Inoue, K. Miyazawa, M. Miyoshi, and P. Hall. Search for Extremely-High-Velocity H₂O Maser Emission Seyfert Galaxies. *PASJ*, 47:771–799, December 1995. (Cited on page 58.)
- K. Nandra, P. M. O’Neill, I. M. George, and J. N. Reeves. An XMM-Newton survey of broad iron lines in Seyfert galaxies. *MNRAS*, 382:194–228, November 2007. doi: 10.1111/j.1365-2966.2007.12331.x. (Cited on page 82.)
- M. Nenkova, M. M. Sirocky, Ž. Ivezić, and M. Elitzur. AGN Dusty Tori. I. Handling of Clumpy Media. *ApJ*, 685:147–159, September 2008. doi: 10.1086/590482. (Cited on page 5.)
- H. Netzer. AGN emission lines. In R. D. Blandford, H. Netzer, L. Woltjer, T. J.-L. Courvoisier, and M. Mayor, editors, *Active Galactic Nuclei*, pages 57–160, 1990. (Cited on pages 3, 4, 28, and 53.)
- H. Netzer. The Largest Black Holes and the Most Luminous Galaxies. *ApJL*, 583:L5–L8, January 2003. doi: 10.1086/368012. (Cited on page 53.)
- H. Netzer and P. Marziani. The Effect of Radiation Pressure on Emission-line Profiles and Black Hole Mass Determination in Active Galactic Nuclei. *ApJ*, 724:318–328, November 2010. doi: 10.1088/0004-637X/724/1/318. (Cited on page 53.)
- H. Netzer, V. Mainieri, P. Rosati, and B. Trakhtenbrot. The correlation of narrow line emission and X-ray luminosity in active galactic nuclei. *A&A*, 453:525–533, July 2006. doi: 10.1051/0004-6361:20054203. (Cited on page 6.)
- E. Oliva, M. Salvati, A. F. M. Moorwood, and A. Marconi. Size and physical conditions of the coronal line region in a nearby Seyfert 2: the Circinus galaxy. *A&A*, 288:457–465, August 1994. (Cited on page 82.)
- C. A. Onken, L. Ferrarese, D. Merritt, B. M. Peterson, R. W. Pogge, M. Vestergaard, and A. Wandel. Supermassive Black Holes in Active Galactic Nuclei. II. Calibration of the Black Hole Mass-Velocity Dispersion Relationship for Active Galactic Nuclei. *ApJ*, 615:645–651, November 2004. doi: 10.1086/424655. (Cited on page 44.)
- F. Panessa, L. Bassani, M. Cappi, M. Dadina, X. Barcons, F. J. Carrera, L. C. Ho, and K. Iwasawa. On the X-ray, optical emission line and black hole mass properties of local Seyfert galaxies. *A&A*, 455:173–185, August 2006. doi: 10.1051/0004-6361:20064894. (Cited on pages 6 and 82.)
- F. Patat, S. Moehler, K. O’Brien, E. Pompei, T. Bensby, G. Carraro, A. de Ugarte Postigo, A. Fox, I. Gavignaud, G. James, H. Korhonen, C. Ledoux, S. Randall, H. Sana, J. Smoker, S. Stefl, and T. Szeifert. Optical atmospheric extinction over Cerro Paranal. *A&A*, 527:A91, March 2011. doi: 10.1051/0004-6361/201015537. (Cited on page 22.)
- C. Y. Peng, L. C. Ho, C. D. Impey, and H.-W. Rix. Detailed Structural Decomposition of Galaxy Images. *AJ*, 124:266–293, July 2002. doi: 10.1086/340952. (Cited on page 51.)

- G. C. Perola, G. Matt, F. Fiore, P. Grandi, M. Guainazzi, F. Haardt, L. Maraschi, T. Mineo, F. Nicastro, and L. Piro. BeppoSAX observations of Mrk 509 and MCG +8-11-11. *A&A*, 358:117–124, June 2000. (Cited on page 82.)
- G. C. Perola, G. Matt, M. Cappi, F. Fiore, M. Guainazzi, L. Maraschi, P. O. Petrucci, and L. Piro. Compton reflection and iron fluorescence in BeppoSAX observations of Seyfert type 1 galaxies. *A&A*, 389:802–811, July 2002. doi: 10.1051/0004-6361:20020658. (Cited on page 82.)
- B. M. Peterson, I. Wanders, R. Bertram, J. F. Hunley, R. W. Pogge, and R. M. Wagner. Optical Continuum and Emission-Line Variability of Seyfert 1 Galaxies. *ApJ*, 501:82, July 1998a. doi: 10.1086/305813. (Cited on pages 4, 37, 48, and 49.)
- B. M. Peterson, I. Wanders, K. Horne, S. Collier, T. Alexander, S. Kaspi, and D. Maoz. On Uncertainties in Cross-Correlation Lags and the Reality of Wavelength-dependent Continuum Lags in Active Galactic Nuclei. *PASP*, 110: 660–670, June 1998b. doi: 10.1086/316177. (Cited on pages 31 and 41.)
- B. M. Peterson, L. Ferrarese, K. M. Gilbert, S. Kaspi, M. A. Malkan, D. Maoz, D. Merritt, H. Netzer, C. A. Onken, R. W. Pogge, M. Vestergaard, and A. Wandel. Central Masses and Broad-Line Region Sizes of Active Galactic Nuclei. II. A Homogeneous Analysis of a Large Reverberation-Mapping Database. *ApJ*, 613:682–699, October 2004. doi: 10.1086/423269. (Cited on pages 4, 27, 31, 32, 37, 41, 44, and 45.)
- B. M. Peterson, M. C. Bentz, L.-B. Desroches, A. V. Filippenko, L. C. Ho, S. Kaspi, A. Laor, D. Maoz, E. C. Moran, R. W. Pogge, and A. C. Quillen. Multiwavelength Monitoring of the Dwarf Seyfert 1 Galaxy NGC 4395. I. A Reverberation-based Measurement of the Black Hole Mass. *ApJ*, 632:799–808, October 2005. doi: 10.1086/444494. (Cited on page 44.)
- M. M. Phillips, P. A. Charles, and J. A. Baldwin. Nearby galaxies with Seyfert-like nuclei. *ApJ*, 266:485–501, March 1983. doi: 10.1086/160797. (Cited on page 82.)
- E. A. Pier and J. H. Krolik. Infrared spectra of obscuring dust tori around active galactic nuclei. I - Computational method and basic trends. *ApJ*, 401:99–109, December 1992. doi: 10.1086/172042. (Cited on page 2.)
- M. Polletta, L. Bassani, G. Malaguti, G. G. C. Palumbo, and E. Caroli. A Multiwavelength Catalog of Seyfert 2 Galaxies Observed in the 2–10 keV Energy Band. *ApJS*, 106:399–+, October 1996. doi: 10.1086/192342. (Cited on page 82.)
- F. Pozo Nuñez, M. Ramolla, C. Westhues, C. Bruckmann, M. Haas, R. Chini, K. Steenbrugge, and M. Murphy. Photometric reverberation mapping of 3C 120. *A&A*, 545:A84, September 2012. doi: 10.1051/0004-6361/201219107. (Cited on page 4.)
- M. Ramolla, M. Haas, V. N. Bennert, and R. Chini. Megamaser detection and nuclear obscuration in Seyfert galaxies. *A&A*, 530:A147, June 2011. doi: 10.1051/0004-6361/201015247. (Cited on pages 6 and 57.)
- M. Ramolla, F. Pozo Nuñez, C. Westhues, M. Haas, and R. Chini. In preparation: Photometric reverberation mapping of RXJ1741.4+0348, 2013. (Cited on page 17.)
- Michael Ramolla. Middle-Infrared Spectroscopy of Seyfert Galaxies, Diploma Thesis, Ruhr-Universität Bochum, June 2009. (Cited on pages 58 and 82.)
- Michael Ramolla. Documentation of the VYSOS16 Telescope, 2011. URL <http://dl.dropbox.com/u/1798034/v16doc.pdf>. (Cited on page 9.)
- A. R. Rao, K. P. Singh, and M. N. Vahia. X-ray variability in the Seyfert galaxy Markarian 618. *MNRAS*, 255:197–202, March 1992. (Cited on page 82.)
- J. N. Reeves and M. J. L. Turner. X-ray spectra of a large sample of quasars with ASCA. *MNRAS*, 316:234–248, August 2000. doi: 10.1046/j.1365-8711.2000.03510.x. (Cited on page 82.)
- C. S. Reynolds. An X-ray spectral study of 24 type 1 active galactic nuclei. *MNRAS*, 286:513–537, April 1997. (Cited on page 82.)
- A. G. Riess, A. V. Filippenko, P. Challis, A. Clocchiatti, A. Diercks, P. M. Garnavich, R. L. Gilliland, C. J. Hogan, S. Jha, R. P. Kirshner, B. Leibundgut, M. M. Phillips, D. Reiss, B. P. Schmidt, R. A. Schommer, R. C. Smith, J. Spyromilio, C. Stubbs, N. B. Suntzeff, and J. Tonry. Observational Evidence from Supernovae for an Accelerating Universe and a Cosmological Constant. *AJ*, 116:1009–1038, September 1998. doi: 10.1086/300499. (Cited on page 56.)
- G. Risaliti. The BeppoSAX view of bright Compton-thin Seyfert 2 galaxies. *A&A*, 386:379–398, May 2002. doi: 10.1051/0004-6361:20020170. (Cited on page 67.)
- G. Risaliti, R. Gilli, R. Maiolino, and M. Salvati. The hard X-ray emission of luminous infrared galaxies. *A&A*, 357: 13–23, May 2000. (Cited on page 82.)
- P. M. Rodríguez-Pascual, M. Santos-Lleo, and J. Clavel. A comparative study of the discrete and cross correlation techniques - an application to the NGC 5548 IUE light-curve. *A&A*, 219:101–104, July 1989. (Cited on pages 39 and 41.)
- B. Rush and M. A. Malkan. Multiwavelength Observations of 12-Micron-Selected Active Galaxies from the X-Rays to the Far-IR. In *Bulletin of the American Astronomical Society*, volume 25 of *Bulletin of the American Astronomical Society*, pages 1362–+, December 1993. (Cited on pages 57 and 81.)
- Y. Sakata, T. Minezaki, Y. Yoshii, Y. Kobayashi, S. Koshida, T. Aoki, K. Enya, H. Tomita, M. Suganuma, Y. Katsuno Uchimoto, and S. Sugawara. Long-Term Optical Continuum Color Variability of Nearby Active Galactic Nuclei. *ApJ*, 711:461–483, March 2010. doi: 10.1088/0004-637X/711/1/461. (Cited on pages 46, 47, 48, 49, 50, 51, 52, 53, 55, and 79.)

- H. Sana, E. Gosset, G. Rauw, E. Antokhina, P. Royer, J. Manfroid, and J.-M. Vreux. CPD-41° 7742: an unusual wind interaction. In G. Rauw, Y. Nazé, R. Blomme, and E. Gosset, editors, *Massive Stars and High-Energy Emission in OB Associations*, pages 89–92, November 2005. (Cited on page 17.)
- N. Sato, A. Yamauchi, Y. Ishihara, K. Sorai, N. Kuno, N. Nakai, R. Balasubramanyam, and P. Hall. Water-Vapor Maser Survey for Active Galactic Nuclei: A Megamaser in NGC 6926. *PASJ*, 57:587–594, August 2005. (Cited on page 58.)
- D. J. Schlegel, D. P. Finkbeiner, and M. Davis. Maps of Dust Infrared Emission for Use in Estimation of Reddening and Cosmic Microwave Background Radiation Foregrounds. *ApJ*, 500:525, June 1998. doi: 10.1086/305772. (Cited on pages 20, 22, 48, 50, 52, and 53.)
- H. R. Schmitt, J. L. Donley, R. R. J. Antonucci, J. B. Hutchings, and A. L. Kinney. A Hubble Space Telescope Survey of Extended [O III] λ 5007 Emission in a Far-Infrared Selected Sample of Seyfert Galaxies: Observations. *ApJS*, 148: 327–352, October 2003. doi: 10.1086/377440. (Cited on pages 57, 81, and 82.)
- M. Schweitzer, D. Lutz, E. Sturm, A. Contursi, L. J. Tacconi, M. D. Lehnert, K. M. Dasyra, R. Genzel, S. Veilleux, D. Rupke, D.-C. Kim, A. J. Baker, H. Netzer, A. Sternberg, J. Mazzarella, and S. Lord. Spitzer Quasar and ULIRG Evolution Study (QUEST). I. The Origin of the Far-Infrared Continuum of QSOs. *ApJ*, 649:79–90, September 2006. doi: 10.1086/506510. (Cited on page 6.)
- S. G. Sergeev, S. A. Klimanov, N. G. Chesnok, and V. I. Pronik. Optical variability of the active galactic nucleus 1E 0754.6+3928 and reverberation-based mass estimate for the central black hole. *Astronomy Letters*, 33:429–436, July 2007. doi: 10.1134/S1063773707070018. (Cited on page 44.)
- P. Severgnini, G. Risaliti, A. Marconi, R. Maiolino, and M. Salvati. An X-ray and near-IR spectroscopic analysis of the ULIRG IRAS 05189-2524. *A&A*, 368:44–51, March 2001. doi: 10.1051/0004-6361:20000522. (Cited on page 82.)
- Z. Shang, B. J. Wills, D. Wills, and M. S. Brotherton. Spectral Properties from Ly α to H α for an Essentially Complete Sample of Quasars. I. Data. *AJ*, 134:294–393, July 2007. doi: 10.1086/518505. (Cited on page 82.)
- R. M. Sharples, A. J. Longmore, T. G. Hawarden, and D. Carter. NGC 7172 - an obscured active nucleus. *MNRAS*, 208:15–24, May 1984. (Cited on page 82.)
- K. Shinozaki, T. Miyaji, Y. Ishisaki, Y. Ueda, and Y. Ogasaka. Spectral Statistics and Local Luminosity Function of a Complete Hard X-Ray Sample of the Brightest Active Galactic Nuclei. *AJ*, 131:2843–2858, June 2006. doi: 10.1086/504155. (Cited on page 82.)
- X. W. Shu, J. X. Wang, P. Jiang, L. L. Fan, and T. G. Wang. Investigating the Nuclear Obscuration in Two Types of Seyfert 2 Galaxies. *ApJ*, 657:167–176, March 2007. doi: 10.1086/510579. (Cited on page 82.)
- D. A. Smith and A. S. Wilson. A Chandra Observation of the Circinus Galaxy. *ApJ*, 557:180–192, August 2001. doi: 10.1086/321667. (Cited on page 82.)
- J. D. T. Smith and B. T. Draine. Pahfit web description, 2008. <http://tir.astro.utoledo.edu/jdsmith/research/pahfit.php>. (Cited on page 59.)
- J. D. T. Smith, B. T. Draine, D. A. Dale, J. Moustakas, R. C. Kennicutt, Jr., G. Helou, L. Armus, H. Roussel, K. Sheth, G. J. Bendo, B. A. Buckalew, D. Calzetti, C. W. Engelbracht, K. D. Gordon, D. J. Hollenbach, A. Li, S. Malhotra, E. J. Murphy, and F. Walter. The Mid-Infrared Spectrum of Star-forming Galaxies: Global Properties of Polycyclic Aromatic Hydrocarbon Emission. *ApJ*, 656:770–791, February 2007. doi: 10.1086/510549. (Cited on page 59.)
- L. Spinoglio and M. A. Malkan. The 12 micron galaxy sample. I - Luminosity functions and a new complete active galaxy sample. *ApJ*, 342:83–99, July 1989. doi: 10.1086/167577. (Cited on page 57.)
- T. Storchi-Bergmann, A. L. Kinney, and P. Challis. Ultraviolet to Near-Infrared Spectral Distributions of Star-forming and Seyfert 2 Galaxies. *ApJS*, 98:103–+, May 1995. doi: 10.1086/192156. (Cited on page 82.)
- P. J. Storey and C. J. Zeippen. Theoretical values for the [OIII] 5007/4959 line-intensity ratio and homologous cases. *MNRAS*, 312:813–816, March 2000. doi: 10.1046/j.1365-8711.2000.03184.x. (Cited on pages 25 and 28.)
- D. K. Strickland, T. M. Heckman, E. J. M. Colbert, C. G. Hoopes, and K. A. Weaver. A High Spatial Resolution X-Ray and H α Study of Hot Gas in the Halos of Star-forming Disk Galaxies. I. Spatial and Spectral Properties of the Diffuse X-Ray Emission. *ApJS*, 151:193–236, April 2004. doi: 10.1086/382214. (Cited on page 67.)
- M. Suganuma, Y. Yoshii, Y. Kobayashi, T. Minezaki, K. Enya, H. Tomita, T. Aoki, S. Koshida, and B. A. Peterson. Reverberation Measurements of the Inner Radius of the Dust Torus in Nearby Seyfert 1 Galaxies. *ApJ*, 639:46–63, March 2006. doi: 10.1086/499326. (Cited on page 79.)
- Y. Terashima, N. Iyomoto, L. C. Ho, and A. F. Ptak. X-Ray Properties of LINERs and Low-Luminosity Seyfert Galaxies Observed with ASCA. I. Observations and Results. *ApJS*, 139:1–36, March 2002. doi: 10.1086/324373. (Cited on page 82.)
- G. Theureau, L. Bottinelli, N. Coudreau-Durand, L. Gouguenheim, N. Hallet, M. Loulergue, G. Paturel, and P. Teerikorpi. Kinematics of the local universe. VII. New 21-cm line measurements of 2112 galaxies. *A&AS*, 130:333–339, June 1998. doi: 10.1051/aas:1998416. (Cited on page 28.)
- A. Tilak, L. J. Greenhill, C. Done, and G. Madejski. A Deep 0.3–10 keV Spectrum of the H₂O Maser Galaxy IC 2560. *ApJ*, 678:701–711, May 2008. doi: 10.1086/529537. (Cited on page 82.)
- S. Tommasin, L. Spinoglio, M. A. Malkan, and G. Fazio. Spitzer-IRS High-Resolution Spectroscopy of the 12 μ m Seyfert Galaxies. II. Results for the Complete Data Set. *ApJ*, 709:1257–1283, February 2010. doi: 10.1088/0004-637X/709/2/1257. (Cited on page 59.)

- H. D. Tran. The Unified Model and Evolution of Active Galaxies: Implications from a Spectropolarimetric Study. *ApJ*, 583:632–648, February 2003a. doi: 10.1086/345473. (Cited on page 82.)
- H. T. Tran. Polarization comparison between on-axis and off-axis dual reflector telescopes: Zemax and Grasp8 simulations. *New Astronomy Review*, 47:1091–1096, December 2003b. doi: 10.1016/S1387-6473(03)00234-3. (Cited on page 82.)
- T. J. Turner and K. A. Pounds. The EXOSAT spectral survey of AGN. *MNRAS*, 240:833–880, October 1989. (Cited on page 82.)
- T. J. Turner, I. M. George, K. Nandra, and R. F. Mushotzky. ASCA Observations of Type 2 Seyfert Galaxies. I. Data Analysis Results. *ApJS*, 113:23–+, November 1997. doi: 10.1086/313053. (Cited on page 82.)
- Y. Ueda, Y. Ishisaki, T. Takahashi, K. Makishima, and T. Ohashi. The ASCA Medium Sensitivity Survey (The GIS Catalog Project): Source Catalog II. *ApJS*, 161:185–223, December 2005. doi: 10.1086/468187. (Cited on page 82.)
- S. Ueno, M. J. Ward, P. T. O'Brien, G. M. Stirpe, and G. Matt. BeppoSAX Observations of Luminous Iras Galaxies. *Advances in Space Research*, 25:823–826, 2000. doi: 10.1016/S0273-1177(99)00848-0. (Cited on page 82.)
- C. M. Urry and P. Padovani. Unified Schemes for Radio-Loud Active Galactic Nuclei. *PASP*, 107:803–+, September 1995. doi: 10.1086/133630. (Cited on page 1.)
- M. S. Vaceli, S. M. Viegas, R. Gruenwald, and R. E. de Souza. Spectroscopy of Seyfert 2 Galaxies, Liners, and H(II) Galaxies. *AJ*, 114:1345–+, October 1997. doi: 10.1086/118568. (Cited on page 82.)
- M.-P. Véron-Cetty and P. Véron. A catalogue of quasars and active nuclei: 12th edition. *A&A*, 455:773–777, August 2006. doi: 10.1051/0004-6361:20065177. (Cited on page 82.)
- F. Verrecchia, J. J. M. in't Zand, P. Giommi, P. Santolamazza, S. Granata, J. J. Schuurmans, and L. A. Antonelli. The BeppoSAX WFC X-ray source catalogue. *A&A*, 472:705–713, September 2007. doi: 10.1051/0004-6361:20067040. (Cited on page 82.)
- M. Vestergaard. Determining Central Black Hole Masses in Distant Active Galaxies. *ApJ*, 571:733–752, June 2002. doi: 10.1086/340045. (Cited on pages 28 and 53.)
- W. F. Welsh and K. Horne. Echo images of broad-line regions in active Galactic nuclei. *ApJ*, 379:586–591, October 1991. doi: 10.1086/170530. (Cited on page 24.)
- M. Whittle. Virial and jet-induced velocities in Seyfert galaxies. I - A compilation of narrow line region and host galaxy properties. *ApJS*, 79:49–75, March 1992. doi: 10.1086/191644. (Cited on page 82.)
- M. Whittle and A. S. Wilson. Jet-Gas Interactions in Markarian 78. I. Morphology and Kinematics. *AJ*, 127:606–624, February 2004. doi: 10.1086/380940. (Cited on page 82.)
- H. Winkler. The extinction, flux distribution and luminosity of Seyfert 1 nuclei derived from UBV(RI)_C aperture photometry. *MNRAS*, 292:273, December 1997. (Cited on pages 31, 46, 50, and 79.)
- H. Winkler, I. S. Glass, F. van Wyk, F. Marang, J. H. S. Jones, D. A. H. Buckley, and K. Sekiguchi. Variability studies of Seyfert galaxies. I - Broad-band optical photometry. *MNRAS*, 257:659–676, August 1992. (Cited on pages 4, 31, 46, 48, 52, 55, and 78.)
- J.-H. Woo, T. Treu, M. A. Malkan, M. A. Ferry, and T. Misch. Variability of Moderate-Luminosity Active Galactic Nuclei at $z = 0.36$. *ApJ*, 661:60–69, May 2007. doi: 10.1086/516564. (Cited on pages 25 and 28.)
- Y. Yoshii, Y. Kobayashi, and T. Minezaki. The MAGNUM (Multicolor Active Galactic Nuclei Monitoring) Project. In *American Astronomical Society Meeting Abstracts #202*, volume 35 of *Bulletin of the American Astronomical Society*, page 752, May 2003. (Cited on page 79.)
- J. S. Zhang and J. H. Fan. Chandra observations of the h2o megamaser galaxy mrk1210. *Sci Chin.*, 52:G6, 960–968, January 2009. (Cited on page 82.)
- J. S. Zhang, C. Henkel, M. Kadler, L. J. Greenhill, N. Nagar, A. S. Wilson, and J. A. Braatz. Extragalactic H₂O masers and X-ray absorbing column densities. *A&A*, 450:933–944, May 2006. doi: 10.1051/0004-6361:20054138. (Cited on pages 5 and 58.)
- J. S. Zhang, C. Henkel, Q. Guo, H. G. Wang, and J. H. Fan. On The Nuclear Obscuration of H₂O Maser Galaxies. *ApJ*, 708:1528–1536, January 2010. doi: 10.1088/0004-637X/708/2/1528. (Cited on pages 5, 59, 60, 66, and 82.)

*I dedicate this thesis to my dear family,
who supported me unconditionally during my whole life.*

ACKNOWLEDGMENTS

This work is based on observations made with the *Spitzer Space Telescope*, which is operated by the Jet Propulsion Laboratory, California Institute of Technology under a contract with NASA. This research has made use of the NASA/IPAC Extragalactic Database (NED) which is operated by the Jet Propulsion Laboratory, California Institute of Technology, under contract with the U.S. National Aeronautics and Space Administration. The research has been supported as a project of the Nordrhein-Westfälische Akademie der Wissenschaften und der Künste in the framework of the academy program by the Federal Republic of Germany and the state Nordrhein-Westfalen.

I would like to deeply thank all the people that helped me complete this work in one way or another. Either by critical discussions, help in the analysis of enormous amounts of data, or simply by relentlessly cheering me up while I was going through a variety of smaller and bigger problems during the past years. Here I want to express my gratitude in some specific cases. It would be selfish to say that this thesis is a pure product of my own mind. It was only possible due to the wonderful teamwork in our institute and especially our AGN research group.

In the first place, I hold my supervisor Martin Haas, who has spent an unbelievable amount of time and effort to teach me how to perform research and present the results in a quality that is competitive with the leading scientists in this field. Moreover, he was always in reach to talk to about anything, always having incredibly constructive ideas. I am very thankful to Rolf Chini, who has not only awakened my deeper interest in astronomy, but also supported me unconditionally, being a go-to person for really every problem and anytime, no matter how difficult it was. I also thank Wolfram Kollatschny for the fruitful collaboration and his willingness to be my second referee. If it wasn't for Roland Lemke, his patience and overview of the software and hardware at the Universitätssternwarte der Ruhr-Universität Bochum, it would never have been possible for me to enable the *VYSOS 16* telescope to perform robotic observations. A special thank I want to pass on to Francisco Pozo Nuñez, always asking critical questions and investigating every little bit of photometric data with all measures imaginable. But I will also never forget the great hospitality that I enjoyed when I was visiting Chile. Thanks go to Angie Barr Dominguez, Matthias Zetzl and Christian Westhues, for contributing either reduced data or routines that have been used in this thesis. To all other members of the AIRUB that have not been named, I am really thankful for all the good time we had together.

I am also deeply grateful for the numerous proof readers, helping me to relax complicated formulations and to eliminate typos. Among them are Martin Haas, Markus Rokicki, Dominic Wehner, Zhiwei Chen and Stephanie Böcken.

Finally, I would like to thank my family and all my friends for propping up my failing strength, always keeping me laughing and happy. To anyone who does not feel appreciated – I deeply apologize.

Bochum, September 28, 2012

Michael Ramolla

CURRICULUM VITAE

PERSONAL DATA

Date of birth: March 12th 1985
Place of birth: Aurich, Lower Saxony, Germany
Nationality: German

EDUCATION

June 2004
„Abitur“ at the Windthorst-Gymnasium Meppen, Germany

October 2004 – September 2006
Undergraduate studies of physics and astronomy at the Ruhr-Universität Bochum

September 2006
„Physik Diplom-Vorprüfung“, grade: very good

October 2006 – September 2008
Graduate student of physics and mathematics at the Ruhr-Universität Bochum

October 2008 – July 2009
Diploma student at the Astronomisches Institut der Ruhr-Universität Bochum
Supervised by Dr. habil. Martin Haas
Title of the thesis: Middle-Infrared Spectroscopy of Seyfert Galaxies

July 2009
„Physik Diplomprüfung“, grade: very good

August 2009 – present
PhD student at the Astronomisches Institut der Ruhr-Universität Bochum
Supervised by Dr. habil. Martin Haas
Title of the thesis: The Central Region of Active Galactic Nuclei

DECLARATION

Versicherung gemäß §7 Abs. 2 Nr. 5 PromO 1987

Hiermit versichere ich, dass ich meine Dissertation selbstständig angefertigt und verfasst und keine anderen als die angegebenen Hilfsmittel und Hilfen benutzt habe. Meine Dissertation habe ich in dieser oder ähnlicher Form noch bei keiner anderen Fakultät der Ruhr-Universität Bochum oder bei einer anderen Hochschule eingereicht.

I hereby certify that this dissertation has been composed by myself and is based on my own work, unless stated otherwise. My dissertation has not been submitted for any other degree in any faculty of the Ruhr-Universität Bochum or any other tertiary institution.

Bochum, September 28, 2012

Michael Ramolla